Superconducting Quantum Metamaterials as Active Lasing Medium: Effects of Disorder and Longitudinal Couplings

(Supraleitende Quantenmetamaterialien als aktives Lasermedium: Einfluss von Unordnung und longitudinalen Kopplungen)

Masterarbeit
von

Martin Koppenhöfer

am Institut für Theoretische Festkörperphysik

Referent: Prof. Dr. G. Schön
Korreferent: Prof. Dr. E. Il'ichev
Betreuender Mitarbeiter: Dr. M. Marthaler

Bearbeitungszeit: 02.04.2015 – 31.03.2016

Erklärung zur Selbstständigkeit

Ich versichere, dass ich diese Arbeit selbstständig verfasst habe und keine anderen als die angegebenen Quellen und Hilfsmittel benutzt habe, die wörtlich oder inhaltlich übernommenen Stellen als solche kenntlich gemacht und die Satzung des KIT zur Sicherung guter wissenschaftlicher Praxis in der gültigen Fassung vom 27.11.2014 beachtet habe.

Karlsruhe, den 31.03.2016, _____

Martin Koppenhöfer

Contents

List of Figures

1. Introduction

Although the first laser had been considered as "a solution looking for a problem" [1], lasers nowadays serve as the standard source of coherent light with a wide range of applications [2]. The term "laser" was originally coined as an abbreviation for its operation principle, "Light Amplification by Stimulated Emission of Radiation". The basic components of a laser are a resonator that stores photons and selects particular modes, an optically active medium that emits photons coherently into the resonator by stimulated emission, and a pumping process that establishes population inversion in the medium [3]. A large variety of systems can serve as optically active medium. This includes natural atoms [4] or semiconductor devices [5], but also superconducting circuits [6] or quantum dot systems [7]. The latter ones are often called "artificial atoms" because they provide a simple energy level structure similar to that of natural atoms, but they are artificially created structures.

In 2007, Astafiev *et al.* demonstrated the creation of coherent laser radiation with a superconducting single-electron transistor coupled to a coplanar waveguide microwave resonator [6]. This setup should in principle be called a "maser" because it emitted microwave radiation instead of optical light. Since that time, several experiments followed which demonstrated lasing with other types of superconducting circuits and quantum dot systems [7, 8, 9].

So far all single or few-artificial-atom lasing experiments produce radiation at a rather low intensity. A way to reach a higher output power is to couple more artificial atoms to a common resonator. Such multi-atom setups are named "quantum metamaterials" for the following reasons [10]: First, the size of an artificial atom is of the order of micrometers or below, i.e., it is much smaller than the wavelength of the emitted radiation, which is of the order of centimeters. Second, the properties and couplings of the artificial atoms can be tailored in order to obtain new functionality by the interaction of these atoms with a radiation field.

A possible application of quantum metamaterials is the construction of a microwave laser. Coherent microwave radiation is necessary to control superconducting quantum bits (qubits). Currently, microwave generators are used as a source of coherent microwave radiation, but they have to be connected from outside to the superconducting qubits in the cryostat. This limits the number of independently controllable qubits and introduces undesirable heat bridges. Approaches to build on-chip microwave sources have been studied, including voltage-biased Josephson junctions or nonlinear resonators close to the quantum regime [11, 12, 13]. However, these devices emit incoherent radiation unless driven by a coherent microwave source. The usage of quantum metamaterials as active lasing medium offers another way to build on-chip microwave radiation sources for low-temperature experiments. As a proof of principle the coupling of 20 superconducting flux qubits to a microwave resonator has already been demonstrated experimentally by Macha *et al.* in 2014 [14].

Disorder

A challenge in the usage of artificial instead of natural atoms for lasing is the presence of fluctuations in the parameters of the individual atoms, e.g., in the level-splitting energy, the coupling strength to a resonator, or the local driving. There are several reasons for this behavior. First, superconducting circuits are typically created using thin-film deposition techniques, e.g., shadow evaporation, or optical or electron-beam lithography [15]. In this fabrication process the actually obtained device geometry deviates from the intended dimensions, which causes fluctuations of the setup parameters, for instance, the capacitances and critical currents [16]. A second source of fluctuations is noise due to the environment of the artificial atoms, e.g., fluctuations of the control voltages or the control magnetic fields, inhomogeneities of applied fields, flux trapping, or charge noise [15, 16]. In the following we denote these fluctuations of atomic parameters in a multi-atom lasing setup as disorder.

Disorder may obstruct multi-atom lasing because artificial atoms with a weak coupling strength to the resonator or a far-detuned level-splitting energy are expected not to participate in the lasing process. For example, in the flux-qubit metamaterial only 8 out of 20 artificial atoms interacted resonantly with the microwave cavity at a time [14].

In this thesis the influence of disorder on multi-atom lasing setups is investigated, with a focus on static sample-to-sample fluctuations and quasistatic fluctuations on long timescales of up to hours. We show that multi-atom lasing setups are surprisingly robust against disorder as the range of parameters that allow for lasing is widened because of collective effects arising for a large number of atoms in the metamaterial. Choosing a large number of artificial atoms in the metamaterial is actually a way to compensate for disorder.

Longitudinal couplings

An interesting property of the usage of artificial atoms as active lasing medium is the presence of longitudinal couplings to the radiation field. In the radiation gauge, the interaction between an atom and an electric field $\boldsymbol{E}$ is well described by a dipole interaction $H_{\text{int}} = -e\boldsymbol{r} \cdot \boldsymbol{E}$, where $-e\boldsymbol{r}$ is the dipole moment of the atom [17]. Natural atoms have an inversion-symmetric Coulomb potential, i.e., the wave function of each state is either symmetric or antisymmetric with respect to inversion, which corresponds to a parity of ± 1, respectively. The dipole-moment operator has parity -1, hence, all of its matrix elements which are taken between atomic states with the same parity vanish. Therefore, the coupling of a two-level atom with an inversion-symmetric atomic potential has only a transversal contribution,

$$H_{\text{int}} = \hbar g \sigma_x \left(a + a^\dagger \right) , \qquad (1.1)$$

where σ_x is the first Pauli matrix. The annihilation and creation operators of the electromagnetic field are denoted by a and $a^\dagger$, respectively, and g is the coupling strength of the atom to the electric field.

However, for superconducting circuits and quantum dot systems an additional longitudinal contribution arises: For superconducting qubits there are two basic circuit designs, a so-called Cooper pair box and a rf SQUID [18]. The Cooper pair box allows for the construction of charge and transmon qubits, depending on the chosen parameters. The rf SQUID is used to construct flux and phase qubits. In practice, more sophisticated circuit designs are used in order to achieve tunable qubit parameters or the reduction of noise and undesired interactions with the environment. For charge and flux qubits there is a bias point where the level structure shows a large anharmonicity, i.e., the two lowest energy levels are nearly degenerate and all other levels have a much higher energy. Then, the

system can be restricted to these two lowest energy eigenstates and is effectively described by a two-level system [18],

$$H_{\text{TLS}} = \frac{\delta}{2}\tau_z - \frac{t}{2}\tau_x \,. \tag{1.2}$$

For a charge qubit the level-splitting energy δ is proportional to the control charge on the superconducting island and t is given by the Josephson energy of the junction. For a flux qubit the asymmetry δ of the effective double-well potential depends on the flux bias through the SQUID loop and t is the tunneling rate through the central barrier. Both circuit designs couple to the electromagnetic field of a resonator by a τ_z interaction [19],

$$H_{\text{int}} = \hbar g \tau_z \left(a + a^\dagger\right) \,. \tag{1.3}$$

Quantum computation and lasing processes are performed in the eigenbasis of the Hamiltonian (1.2), which is obtained by a rotation of the state space by an angle $\theta = \tan^{-1}(-t/\delta)$. This yields the diagonalized Hamiltonian $H_{\text{TLS}}^{\text{diag}} = \frac{1}{2}\sqrt{\delta^2 + t^2}\sigma_z$. The diagonalization modifies the interaction term (1.3) as well, which takes the following form in the eigenbasis of the qubit Hamiltonian (1.2):

$$H_{\text{int}}^{\text{diag}} = \hbar g \left(\cos(\theta)\sigma_z + \sin(\theta)\sigma_x \right) \left(a + a^\dagger\right) \,. \tag{1.4}$$

In contrast to the pure σ_x interaction (1.1) of conventional atoms an additional σ_z interaction arises for superconducting circuits. The relative strength of the σ_x and σ_z interactions is adjusted via the angle θ originating from the diagonalization of the qubit Hamiltonian.

The interaction term (1.4) applies also to quantum-dot systems [20].

For conventional atoms a longitudinal σ_z-type interaction is forbidden by the inversion symmetry of the atomic Coulomb potential. Therefore, systems with an interaction of the form of Eq. (1.4) can be considered as artificial atoms with an atomic potential with broken inversion symmetry. In the second part of this thesis we show that such longitudinal couplings allow for the creation of photon-number squeezed light characterized by a Fano factor $F \ll 1$.

Squeezed light

Interferometric measurements are sensitive to the phase difference of light that has traveled along different optical paths. Lasers are used as light sources for these experiments because they provide coherent light with large coherence lengths and times at high intensity and, therefore, allow for long optical pathways. Because of the quantized nature of light, the amplitude and phase of a monochromatic electromagnetic wave obey an uncertainty relation and cannot be instantaneously determined to arbitrary precision. Therefore, even an ideal laser shows shot noise fluctuations of its intensity and phase [21]. This ultimately limits the precision of interferometric measurements.

The usage of squeezed light has been proposed as way to overcome this quantum shot-noise limit [22]. For squeezed light the uncertainty of one quantum-mechanical observable is reduced at the cost of an increased uncertainty of its conjugate quantity. So-called quadrature-squeezed light is successfully applied to increase the phase-measurement sensitivity of gravitational wave detectors [23, 24]. Also spectroscopic measurements [25] and qubit read-out [26] benefit from the usage of squeezed light. Besides quadrature squeezing, intensity fluctuations can be decreased as well. A way to obtain such sub-Poissonian or photon-number squeezed radiation is presented in this thesis. Scully and Agarwal showed that in Ramsey-type interferometers the signal-to-noise ratio is proportional to the Fano factor F of the radiation used to excite the atoms and, therefore, the usage of photon-number squeezed light in Ramsey interferometry enhances the measurement sensitivity [27].

Contents

This thesis is organized as follows: In Chap. 2 the quantum-mechanical treatment of a laser based on a density-matrix description is introduced. We derive the Bloch-Redfield master equation which describes the coherent interaction of the atom with the radiation field as well as pumping, relaxation, and dephasing processes. Different approaches to solve this quantum master equation are presented. The semiclassical approach is reviewed briefly, because it provides estimates on the lasing threshold that are used in the following chapters.

In Chap. 3 the basic types of squeezed light are introduced and the Fano factor is defined, which is a measure for the photon-number squeezedness of radiation.

The influence of disorder on multi-atom lasing setups is investigated in Chap. 4. We use a semiquantum approach to calculate the photon-number expectation value $\langle n \rangle$ out of the Bloch-Redfield master equation. Disorder in the setup is modeled by a probability distribution that describes the spread of the lasing parameters around their intended mean values. A method to relate the mean photon-number expectation value to the standard deviation of this distribution is developed and applied to disorder in the detuning, the coupling strength, and the pumping strength. The mean photon-number expectation value is found to be surprisingly robust against disorder. The origin of this is a widening of the range of parameters that allow for lasing: In a multi-atom lasing setup the lasing resonance curve as a function of the detuning is broadened, the minimal required coupling strength to the resonator is lowered, and the lasing-threshold pumping strength is decreased compared to a single-atom laser. The origin of this effect is enhanced stimulated emission, which is shown by reformulating the multi-atom lasing equation as a set of coupled single-atom lasing equations that have to be solved self-consistently.

In the near future, experimental realizations of metamaterials are expected to consist of a not too large number of artificial atoms, e.g., of the order of 100 or below. Then, significant sample-to-sample specific deviations from the mean photon-number expectation value are likely. Similar deviations may also be caused by quasistatic fluctuations of the atomic parameters in a setup that is operated for a longer time. Therefore, in a last step we investigate these fluctuations numerically.

In Chap. 5 the influence of an additional longitudinal coupling to the resonator is examined. We study lasing in the presence of an interaction term given by Eq. (1.4). This generalized lasing Hamiltonian is mapped onto a Jaynes-Cummings-like Hamiltonian by a polaron transformation. In the interaction term of this polaron-transformed Hamiltonian the annihilation and creation operators are replaced by more complicated operators acting on the radiation field of the resonator. In particular, the effective coupling strength between atom and resonator vanishes for certain numbers of photons in the resonator. This opens a way to create photon-number squeezed light if the photon-number expectation value $\langle n \rangle$ is chosen close to such a root of the coupling. The master equation is solved for the polaron-transformed Hamiltonian following the approach of Scully and Lamb [17]. In a first step we calculate the photon statistics and the Fano factor of a single-atom laser and we discuss the implementation of a pumping process. Roots of the coupling exist for any mixing angle θ that allows for a nonzero σ_z and σ_x interaction. We discuss the dependence of squeezing on the mixing angle θ and it turns out that the creation of squeezed light is possible if there is a strong σ_z interaction between the atoms and the radiation field.

In a second step our results are generalized to a multi-atom lasing setup, which is treated in a mean-field theory. The photon-number expectation value scales linearly with the number of atoms, M, which opens a way to increase the output power of the laser. However, we find that the Fano factor F contains terms that scale proportional to M^2 and may spoil

squeezing. For a large number of atoms of the order of 100 or above, this restricts the range of lasing parameters that allow for the creation of photon-number squeezed light.

Finally, we investigate the influence of fluctuations in the mixing angle θ and the detuning on the multi-atom lasing setup. Such fluctuations are caused by charge or flux noise. We find that disorder decreases the photon-number expectation value and increases the Fano factor. However, even for large disorder a photon-number squeezed state can still be realized.

2. Quantum theory of the laser

A laser consists of three basic components [3]: First, a resonator is needed to store photons and to select particular modes of the radiation field. Second, an optically active medium is necessary which provides several energy levels. At least one transition energy between two levels should match the resonator frequency, such that photons are emitted into or absorbed out of the resonator by atomic transitions between these levels. This transition is also called the lasing transition. An atom interacting resonantly with a radiation field emits photons either by spontaneous or by stimulated emission. Stimulated emission is a coherent emission process triggered by an already excited radiation field. Spontaneous emission is independent of the excitation state of the radiation field and, in general, photons are incoherently emitted by spontaneous emission. In a laser, stimulated emission must dominate over spontaneous emission. Therefore, third, a pumping mechanism is needed that creates population inversion, i.e., contrary to a thermal population the upper state of the lasing transition has a higher occupation than the lower one. If population inversion is established, stimulated emission dominates over spontaneous emission and the interaction of the atom with the radiation field yields a highly coherent multi-photon state in the resonator.

In this chapter we discuss how to model these three components in a quantum theory of the laser. We start in Sec. 2.1 with an effective Hamiltonian which describes the coherent interaction of the atomic lasing transition with a radiation field. Pumping, relaxation, and dephasing processes are accounted for by Lindblad terms in a quantum master equation, which is derived in Sec. 2.2. In Sec. 2.4 we discuss different approaches to solve this quantum master equation and, finally, in Sec. 2.5 the semiclassical approach is reviewed because it provides expressions for the lasing threshold that are used in the following.

2.1. Effective lasing Hamiltonian

The interaction of a single atom with a single mode of the radiation field is modeled by the following Jaynes-Cummings Hamiltonian [17]:

$$H_{\mathrm{JC}} = \hbar\omega a^\dagger a + \frac{1}{2}\epsilon\sigma_z + \hbar g\left(\sigma_+ a + \sigma_- a^\dagger\right).\tag{2.1}$$

The radiation field of the resonator is described by a harmonic oscillator with bosonic annihilation and creation operators a and $a^\dagger$, respectively. Only the lasing transition of the atom is considered, which is modeled as a two-level system with level-splitting energy ϵ. We denote the Pauli matrices by $\sigma_{x,y,z}$. The matrices $\sigma_\pm = \frac{1}{2}\left(\sigma_x \pm i\sigma_y\right)$ describe atomic transitions between the two lasing states. The interaction has a coupling strength g.

In this thesis multi-atom lasing setups are studied. Therefore, the Jaynes-Cummings Hamiltonian (2.1) needs to be generalized to M two-level atoms coupled to a common

resonator. If direct atomic interactions are neglected, the setup is described by the Tavis-Cummings Hamiltonian

$$H_{\mathrm{TC}} = \hbar\omega a^\dagger a + \sum_{j=1}^{M} \frac{1}{2}\epsilon_j \sigma_z^j + \sum_{j=1}^{M} \hbar g_j \left(\sigma_+^j a + \sigma_-^j a^\dagger \right) . \qquad (2.2)$$

The M individual atoms are labeled by the index j, $j \in \{1, \ldots, M\}$. Each atom may have an individual level splitting energy ϵ_j and an individual coupling strength g_j to the resonator. The superscript j at the Pauli and transition matrices $\sigma_{x,y,z,\pm}^j$ denotes the index of the atom they act on.

2.2. Quantum master equation in Bloch-Redfield form

The Hamiltonians (2.1) and (2.2) describe only the coherent interaction of a resonator field with a two-level system representing the lasing transition. In order to obtain a complete description of a laser, incoherent processes have to be accounted for as well: First, the pumping process is modeled as an incoherent excitation process of the two-level atom with an excitation or pumping rate $\Gamma_\uparrow$. Second, light is coupled out of the resonator in order to be used in experiments, which is essentially a photon loss process of the resonator. A method to account for both coherent and dissipative processes is to use a quantum master equation for the density matrix ρ of the system, which is derived in this section.

Coherent processes are described by a Liouville term that involves the coherent Hamiltonian H_{coh},

$$\left.\frac{\partial}{\partial t}\rho\right|_{\mathrm{coh}} = -\frac{i}{\hbar}\left[H_{\mathrm{coh}}, \rho\right] .$$

In our case, H_{coh} is the Jaynes-Cummings or the Tavis-Cummings Hamiltonian. Incoherent processes are modeled by Lindblad superoperators L_{inc},

$$\left.\frac{\partial}{\partial t}\rho\right|_{\mathrm{inc}} = L_{\mathrm{inc}}\rho .$$

If the master equation is considered as a set of coupled linear first-order differential equations for the matrix elements of the density matrix ρ, the Lindblad superoperators introduce terms describing a decay of the matrix elements. As a starting point for the derivation of particular Lindblad superoperators we derive the Bloch-Redfield form of the master equation. We follow the path described in Refs. [28] and [29].

A way to obtain an effective description of incoherent processes is to assume that the system under consideration, described by the Hamiltonian H_{S}, interacts with external baths, described by H_{R}, via an interaction H_{C}. Thus, the full Hamiltonian reads

$$H = H_{\mathrm{S}} + H_{\mathrm{R}} + H_{\mathrm{C}} .$$

The external baths represent a large environment whose macroscopic state is not perturbed by the interaction with the much smaller system. Later, the bath degrees of freedom are traced out to obtain an effective equation of motion for the system only, which then includes dissipative processes. H_{C} describes the interaction of the system with the baths, therefore we have the following commutation relations:

$$[H_{\mathrm{S}}, H_{\mathrm{R}}] = 0 ,$$
$$[H_{\mathrm{S}}, H_{\mathrm{C}}] \neq 0 ,$$
$$[H_{\mathrm{R}}, H_{\mathrm{C}}] \neq 0 .$$

The equation of motion of the full density matrix χ for the system and the external baths is given by the Liouville equation with the full Hamiltonian H,

$$\frac{\mathrm{d}}{\mathrm{d}t}\chi = -\frac{i}{\hbar}\left[H, \chi\right].$$

In the interaction picture with respect to $H_{\mathrm{S}} + H_{\mathrm{R}}$ we obtain

$$\frac{\mathrm{d}}{\mathrm{d}t}\chi_{\mathrm{I}} = -\frac{i}{\hbar}\left[H_{\mathrm{C,I}}, \chi_{\mathrm{I}}\right], \tag{2.3}$$
$$\chi_{\mathrm{I}}(t) = e^{i(H_{\mathrm{S}}+H_{\mathrm{R}})(t-t_0)/\hbar}\chi(t)e^{-i(H_{\mathrm{S}}+H_{\mathrm{R}})(t-t_0)/\hbar},$$
$$H_{\mathrm{C,I}}(t) = e^{i(H_{\mathrm{S}}+H_{\mathrm{R}})(t-t_0)/\hbar}H_{\mathrm{C}}e^{-i(H_{\mathrm{S}}+H_{\mathrm{R}})(t-t_0)/\hbar}.$$

In the interaction picture $H_{\mathrm{C,I}}$ is explicitly time-dependent. Equation (2.3) can be cast into a corresponding integro-differential equation,

$$\frac{\mathrm{d}}{\mathrm{d}t}\chi_{\mathrm{I}}(t) = -\frac{i}{\hbar}\left[H_{\mathrm{C,I}}(t), \chi_{\mathrm{I}}(t_0)\right] + \left(-\frac{i}{\hbar}\right)^2\int_{t_0}^{t}\mathrm{d}t'\left[H_{\mathrm{C,I}}(t), \left[H_{\mathrm{C,I}}(t'), \chi_{\mathrm{I}}(t')\right]\right]. \tag{2.4}$$

Now, several assumptions are made: First, we assume that at the time t_0 the full density matrix χ factorizes into a product of a density matrix $\rho(t_0)$, describing the state of the system, and a density matrix $R(t_0)$, describing the state of the reservoir,

$$\chi_{\mathrm{I}}(t_0) = \chi(t_0) = \rho(t_0) \otimes R(t_0).$$

The reference time t_0 may be far in the past, $t_0 \to -\infty$. In order to eliminate the first term on the right-hand side of Eq. (2.4), we assume that the reservoir coupling operators have zero expectation value with respect to $R(t_0)$,

$$\mathrm{Tr}_{\mathrm{R}}\left(H_{\mathrm{C,I}}R(t_0)\right) = 0.$$

This condition can always be fulfilled by including a nonzero expectation value into the system Hamiltonian.

Second, a Born approximation is performed. Since the bath is assumed to be much larger than the system, its initial state $R(t_0)$ should not be changed significantly by the interaction with the system, i.e.,

$$\chi(t) \approx \rho(t) \otimes R(t_0).$$

Third, the system is assumed to be Markovian, i.e., the time evolution of $\rho(t)$ only depends on its present state. This is equivalent to the assumption that the bath correlation time is much shorter than the timescale on which the system changes.

Using these assumptions we can trace out the bath degrees of freedom and obtain an equation of motion for the reduced density matrix of the system,

$$\frac{\mathrm{d}}{\mathrm{d}t}\rho_{\mathrm{I}}(t) = -\frac{1}{\hbar^2}\int_{t_0}^{t}\mathrm{d}t'\,\mathrm{Tr}_{\mathrm{R}}\left(\left[H_{\mathrm{C,I}}(t), \left[H_{\mathrm{C,I}}(t'), \rho_{\mathrm{I}}(t) \otimes R(t_0)\right]\right]\right). \tag{2.5}$$

As a fourth assumption, we specify the interaction term H_{C} to be a linear interaction between time-independent Schrödinger operators,

$$H_{\mathrm{C}} = \hbar X O,$$

where X is a bath operator and O is a system operator, thus $[X, O] = [H_S, X] = [H_R, O] = 0$. In the interaction picture we have

$$H_{C,I}(t) = \hbar e^{iH_S(t-t_0)/\hbar} O e^{-iH_S(t-t_0)/\hbar} e^{iH_R(t-t_0)/\hbar} X e^{-iH_R(t-t_0)/\hbar} = \hbar O_I(t) X_I(t) .$$

Then, Eq. (2.5) is given by

$$\frac{\mathrm{d}}{\mathrm{d}t}\rho_I(t) = -\int_{t_0}^{t} \mathrm{d}t' \Big(\quad [O_I(t)O_I(t')\rho_I(t) - O_I(t')\rho_I(t)O_I(t)] \langle X_I(t)X_I(t')\rangle_R$$
$$+ [\rho_I(t)O_I(t')O_I(t) - O_I(t)\rho_I(t)O_I(t')] \langle X_I(t')X_I(t)\rangle_R \Big) ,$$

where the abbreviation $\langle AB \rangle_R = \mathrm{Tr}_R(R(t_0)AB)$ was introduced. If A and B are time-independent Schrödinger operators, the correlator $\langle A(t)B(t')\rangle_R$ is invariant under a translation in time, i.e., it depends only on the time difference $t' - t$. Transforming back to the Schrödinger picture and introducing $\tau = t' - t$ we obtain the Bloch-Redfield form of the master equation,

$$\frac{\mathrm{d}}{\mathrm{d}t}\rho(t) = -\frac{i}{\hbar}[H_S, \rho(t)] + \left[\tilde{O}_+\rho(t)O + O\rho(t)\tilde{O}_- - O\tilde{O}_+\rho(t) - \rho(t)\tilde{O}_-O\right] , \qquad (2.6a)$$

$$\tilde{O}_+ = \int_{-\infty}^{0} \mathrm{d}\tau\, e^{iH_S\tau/\hbar} O e^{-iH_S\tau/\hbar} \langle X_I(0)X_I(\tau)\rangle_R , \qquad (2.6b)$$

$$\tilde{O}_- = \int_{-\infty}^{0} \mathrm{d}\tau\, e^{iH_S\tau/\hbar} O e^{-iH_S\tau/\hbar} \langle X_I(0)X_I(-\tau)\rangle_R . \qquad (2.6c)$$

The properties of the bath enter via the correlators $\langle X_I(0)X_I(\pm\tau)\rangle_R$. Their Fourier transform is the spectral density of the bath,

$$S(\epsilon) = \int_{-\infty}^{\infty} \mathrm{d}\tau\, \langle X_I(0)X_I(\tau)\rangle_R\, e^{-i\epsilon\tau} .$$

For later we also introduce the half-sided Fourier-transformed quantities

$$\frac{1}{2}S_+(\epsilon) = \int_{-\infty}^{0} \mathrm{d}\tau\, \langle X_I(0)X_I(\tau)\rangle_R\, e^{-i\epsilon\tau} = \frac{1}{2}S(\epsilon) + i\mathcal{P}\int_{0}^{\infty} \frac{\mathrm{d}\omega}{2\pi}\frac{S(\omega)}{\epsilon - \omega} , \qquad (2.7a)$$

$$\frac{1}{2}S_-(\epsilon) = \int_{0}^{\infty} \mathrm{d}\tau\, \langle X_I(0)X_I(\tau)\rangle_R\, e^{-i\epsilon\tau} = \frac{1}{2}S(\epsilon) - i\mathcal{P}\int_{0}^{\infty} \frac{\mathrm{d}\omega}{2\pi}\frac{S(\omega)}{\epsilon - \omega} , \qquad (2.7b)$$

where $\mathcal{P}\int$ denotes the Cauchy principle value integral. It holds $S(\epsilon) = \frac{1}{2}S_+(\epsilon) + \frac{1}{2}S_-(\epsilon)$.

2.3. Lindblad superoperators of dissipative atomic and resonator processes

In order to derive a Lindblad superoperator describing relaxation effects of a resonator, Eq. (2.6) is evaluated for a coupling operator $O_{\mathrm{res}} = a^\dagger + a$. An explicit derivation of this superoperator is given in Sec. 5.8, where we also account for effects arising from a polaron transformation of the Hamiltonian. One obtains the following Lindblad superoperator [28]:

$$L_R\rho = \frac{\kappa}{2}(N_{\mathrm{th}} + 1)\left(2a\rho a^\dagger - a^\dagger a\rho - \rho a^\dagger a\right) + \frac{\kappa}{2}N_{\mathrm{th}}\left(2a^\dagger\rho a - aa^\dagger\rho - \rho aa^\dagger\right) , \qquad (2.8)$$

where κ is the damping rate of the resonator and N_{th} is the thermal photon number in the resonator. Equation (2.8) is a specialization of the results obtained in Sec. 5.8 in the limit $p_0 \to 0$.

Atomic pure dephasing is derived using the coupling operator $O_{\mathrm{pd}} = \sigma_z$. Relaxation and pumping processes are obtained using $O_{\mathrm{pr}} = \sigma_x$. Dephasing, relaxation, and pumping can be included into a single Lindblad superoperator

$$L_{\mathrm{Q}}\rho = \frac{\Gamma_\downarrow}{2}\left(2\sigma_-\rho\sigma_+ - \rho\sigma_+\sigma_- - \sigma_+\sigma_-\rho\right) + \frac{\Gamma_\uparrow}{2}\left(2\sigma_+\rho\sigma_- - \rho\sigma_-\sigma_+ - \sigma_-\sigma_+\rho\right) \qquad (2.9)$$
$$+ \frac{\Gamma_\varphi^*}{2}\left(\sigma_z\rho\sigma_z - \rho\right),$$

where $\Gamma_\uparrow$ is the pumping rate, $\Gamma_\downarrow$ is the relaxation rate, and Γ_φ^* is the pure dephasing rate. Again, a derivation of this superoperator is given in Sec. 5.8, where additional effects due to the polaron transformation of the system are also taken into account.

2.4. Approaches to solve the quantum master equation

The dynamics of a laser consisting of M atoms coupled to a common resonator is modeled by the following quantum master equation:

$$\frac{\mathrm{d}}{\mathrm{d}t}\rho = -\frac{i}{\hbar}\left[H_{\mathrm{TC}}, \rho\right] + L_{\mathrm{R}}\rho + \sum_{j=1}^{M} L_{\mathrm{Q},j}\rho. \qquad (2.10)$$

Here H_{TC} is the Tavis-Cummings Hamiltonian given by Eq. (2.2). The Lindblad superoperators L_{R} and $L_{\mathrm{Q},j}$ are defined in Eqs. (2.8) and (2.9). The subscript j denotes that $L_{\mathrm{Q},j}$ acts only on atom j.

There are several ways to solve Eq. (2.10). If only the photon-number expectation value $\langle n \rangle$ is of interest, a semiclassical or semiquantum approach can be used, which amounts to derive a closed set of equations for the photon-number expectation value $\langle n \rangle$. In order to obtain such a closed set of equations, certain expectation values have to be factorized, which is equivalent to neglecting the corresponding quantum-mechanical fluctuations.

Using the master equation (2.10) and the cyclic property of the trace we obtain the following equation of motion for the expectation value of any time-independent operator X:

$$\frac{\mathrm{d}}{\mathrm{d}t}\langle X \rangle = \mathrm{Tr}\left(\dot{\rho}X\right) = \frac{i}{\hbar}\mathrm{Tr}\left(\left[H, X\right]\rho\right) + \mathrm{Tr}\left(\left(L_{\mathrm{R}}\rho\right)X\right) + \sum_{j=1}^{M}\mathrm{Tr}\left(\left(L_{\mathrm{Q},j}\rho\right)X\right). \qquad (2.11)$$

In the *semiclassical* model all correlations between atomic and resonator states are neglected, for instance, $\langle \sigma_z^j a \rangle \approx \langle \sigma_z^j \rangle \langle a \rangle$. This is equivalent to assuming a factorization ansatz for the density matrix, $\rho = \rho_{\mathrm{atom}} \otimes \rho_{\mathrm{res}}$ [30, 31]. It turns out that this description neglects spontaneous emission, but yields a good description of the lasing threshold [32]. In the *semiquantum* model only products of radiation field operators with diagonal atomic operators are factorized, e.g., $\langle \sigma_z^j a^\dagger a \rangle \approx \langle \sigma_z^j \rangle \langle a^\dagger a \rangle$. This approach accounts for spontaneous emission and the photon-number expectation value $\langle n \rangle$ calculated in the semiquantum model coincides well with a direct solution of the master equation (2.10) [33].

Alternatively, the master equation (2.10) can be solved directly. Using this approach one can calculate not only the photon-number expectation value $\langle n \rangle$, but also the photon statistics of the laser.

2.5. Semiclassical approach

In this thesis, an analytical solution of the master equation is calculated in Chap. 5 in order to analyze the influence of longitudinal couplings. The semiquantum approach is used in Chap. 4 to investigate the influence of disorder in the lasing setup.

The semiquantum model predicts a smooth lasing crossover where the system switches from a low, close to thermal average photon number $\langle n \rangle$ to a high photon number. In the limit of large numbers of atoms, this crossover becomes a sharp, kink-like transition, which coincides with the position of the lasing transition predicted by the semiclassical model. Semiclassical and semiquantum model yield the same results in the limit of large photon numbers or large numbers of atoms. However, it has been shown that the position of the lasing transition in the semiclassical approach also provides a good estimate for the position of the lasing crossover in the semiquantum model, even for small numbers of atoms [32]. Therefore, in this section the semiclassical approach for multi-atom lasing setups is briefly discussed and the semiclassical expression for the lasing threshold is derived, following Ref. [34].

Within the semiclassical approach, equations of motion for the expectation values $\langle a \rangle$, $\langle \sigma_z^j \rangle$, and $\left\langle \sigma_-^j \right\rangle$ are calculated. Using Eq. (2.11) and the Tavis-Cummings Hamiltonian (2.2) the following equations of motion are found:

$$\frac{\mathrm{d}}{\mathrm{d}t} \langle a \rangle = -\left(i\omega + \frac{\kappa}{2} \right) \langle a \rangle - \sum_{j=1}^{M} ig_j \left\langle \sigma_-^j \right\rangle ,$$

$$\frac{\mathrm{d}}{\mathrm{d}t} \left\langle \sigma_z^j \right\rangle = 2ig_j \left(\left\langle \sigma_-^j a^\dagger \right\rangle - \left\langle \sigma_+^j a \right\rangle \right) - \Gamma_{1,j} \left\langle \sigma_z^j \right\rangle + \Gamma_{1,j} D_{0,j} ,$$

$$\frac{\mathrm{d}}{\mathrm{d}t} \left\langle \sigma_-^j \right\rangle = -(\Gamma_{\varphi,j} + i\epsilon_j) \left\langle \sigma_-^j \right\rangle + ig_j \left\langle \sigma_z^j a \right\rangle .$$

All correlations between atomic and resonator operators are neglected, i.e., $\langle \sigma_\nu^j a \rangle \approx \langle \sigma_\nu^j \rangle \langle a \rangle$ for $\nu \in \{+, -, z\}$. Decomposing the expectation values into a slowly-varying classical amplitude and a high-frequent oscillation,

$$\langle a \rangle = \alpha(t) e^{-i\omega t} ,$$

$$\left\langle \sigma_\pm^j \right\rangle = s_\pm^j(t) e^{\pm i\omega t} ,$$

$$\left\langle \sigma_z^j \right\rangle = s_z^j(t) ,$$

we obtain the following equations of motion for the classical amplitudes:

$$\frac{\mathrm{d}}{\mathrm{d}t} \alpha = -\frac{\kappa}{2} \alpha - \sum_{j=1}^{M} ig_j s_-^j , \tag{2.12a}$$

$$\frac{\mathrm{d}}{\mathrm{d}t} s_z^j = 2ig_j \left(s_-^j \alpha^* - s_+^j \alpha \right) - \Gamma_{1,j} s_z^j + \Gamma_{1,j} D_{0,j} , \tag{2.12b}$$

$$\frac{\mathrm{d}}{\mathrm{d}t} s_-^j = -\Gamma_{\varphi,j} s_-^j - i\Delta_j s_-^j + ig_j s_z^j \alpha , \tag{2.12c}$$

where $\Delta_j = \epsilon_j/\hbar - \omega$ is the detuning of atom j. The classical field amplitude $\alpha(t)$ decays on a timescale of the order of κ^{-1}, whereas $s_z^j(t)$ and $s_\pm^j(t)$ decay on a timescale of $\Gamma_{1,j}^{-1}$ and $\Gamma_{\varphi,j}^{-1}$, respectively. For typical lasing setups it holds $\kappa \ll \Gamma_1, \Gamma_\varphi$ and, therefore, atomic and resonator dynamics can be decoupled using an adiabatic approximation: We assume that s_z^j and $s_\pm^j$ adapt to changes in α quasi-instantaneously with respect to the timescale on which α evolves. Using the stationary solution of Eqs. (2.12b) and (2.12c), s_-^j is eliminated in Eq. (2.12a), yielding

$$\frac{\mathrm{d}}{\mathrm{d}t} \alpha = -\frac{\kappa}{2} \alpha + \sum_{j=1}^{M} \frac{g_j^2}{\Gamma_{\varphi,j} + i\Delta_j} \frac{D_0}{1 + \frac{|\alpha|^2}{\tilde{n}_{0,j}^{\mathrm{sc}}}} \alpha .$$

Here $\tilde{n}_{0,j}^{\text{sc}}$ is the photon saturation number in the semiclassical theory,

$$\tilde{n}_{0,j}^{\text{sc}} = \frac{\Gamma_{1,j}}{4g_j^2} \frac{\Gamma_{\varphi,j}^2 + \Delta_j^2}{\Gamma_{\varphi,j}} \,. \tag{2.13}$$

The photon-number expectation value in the resonator is given by $|\alpha|^2$. Its stationary value $\langle n \rangle = |\alpha|_{\text{st}}^2$ is defined by

$$\left(\kappa - \sum_{j=1}^{M} 2g_j^2 \frac{\Gamma_{\varphi,j}}{\Gamma_{\varphi,j}^2 + \Delta_j^2} \frac{D_0}{1 + \frac{\langle n \rangle}{\tilde{n}_{0,j}^{\text{sc}}}} \right) \langle n \rangle = 0 \,.$$

For systems consisting of M identical atoms, this equation can be solved explicitly for $\langle n \rangle$. By replacing $\Delta_j = \Delta$, $g_j = g$, $\Gamma_{1,j} = \Gamma_1$, $\Gamma_{\varphi_j} = \Gamma_\varphi$, $\tilde{n}_{0,j}^{\text{sc}} = \tilde{n}_0^{\text{sc}}$ for all atoms j, the following quadratic equation for the photon-number expectation value is obtained:

$$\langle n \rangle^2 + \langle n \rangle \left(\tilde{n}_0^{\text{sc}} - M \frac{\Gamma_1 D_0}{2\kappa} \right) = 0 \,.$$

There is a positive stationary photon-number expectation value if the following condition holds:

$$\tilde{n}_0^{\text{sc}} < M \frac{D_0 \Gamma_1}{2\kappa} \,. \tag{2.14}$$

The laser operates above its lasing threshold, i.e., at a nonzero photon-number expectation value $\langle n \rangle > 0$, if the condition (2.14) is fulfilled. If all but one lasing parameters are fixed, Eq. (2.14) defines a lasing threshold value for the remaining free parameter. For instance, if all lasing parameters except of the detuning Δ are fixed, the laser operates above threshold if the detuning does not exceed a maximum value Δ_{max},

$$|\Delta| < \Delta_{\text{max}} = \Gamma_\varphi \sqrt{2g^2 M \frac{D_0}{\kappa \Gamma_\varphi} - 1} \,. \tag{2.15}$$

Likewise, if all parameters except of the coupling strength g are fixed, the laser operates above threshold if the coupling strength is larger than a minimal value g_{min},

$$g > g_{\text{min}} = \sqrt{\frac{\kappa}{2M D_0} \frac{\Gamma_\varphi^2 + \Delta^2}{\Gamma_\varphi}} \,. \tag{2.16}$$

Finally, the corresponding condition for the pumping strength D_0 is

$$D_0 > D_{0,\text{min}} = \frac{\kappa}{2g^2} \frac{\Gamma_\varphi^2 + \Delta^2}{\Gamma_\varphi} \frac{1}{M} \,. \tag{2.17}$$

These expressions provide a good estimate for the position of the lasing crossover in the semiquantum model and are used in Chap. 4.

3. Squeezed Light

In this chapter the basic concepts of squeezed light are introduced, which are needed later. We derive the amplitude and phase fluctuations of a quantized electromagnetic field and introduce quadrature and photon-number squeezing. The Fano factor is introduced as a measure of the squeezedness of a photon-number squeezed state. Our argumentation follows Refs. [21] and [35].

3.1. Canonical quantization of the electromagnetic field

The vector potential $\boldsymbol{A}$ of the free electromagnetic field canonically quantized in the radiation gauge, $\nabla \cdot \boldsymbol{A} = 0$ and $\Phi = 0$, is given by [36]

$$\boldsymbol{A}(\boldsymbol{x}, t) = \sum_{\boldsymbol{k}} \sum_{\lambda} \sqrt{\frac{\hbar}{2\omega_k \epsilon_0 V}} \boldsymbol{\epsilon}_{\boldsymbol{k},\lambda} \left(a_{\boldsymbol{k},\lambda} e^{i\boldsymbol{k}\boldsymbol{x} - i\omega_k t} + a_{\boldsymbol{k},\lambda}^\dagger e^{-i\boldsymbol{k}\boldsymbol{x} + i\omega_k t} \right) .$$

The scalar potential Φ is chosen to be zero for a free field. The wave vector of the field modes is denoted by $\boldsymbol{k}$, $\lambda \in \{1, 2\}$ are the polarization degrees of freedom, and $\omega_k = c \, |\boldsymbol{k}|$ is the dispersion relation of the field. The normalized polarization vectors $\boldsymbol{\epsilon}_{\boldsymbol{k},\lambda}$ are orthogonal to each other and to the wave vector $\boldsymbol{k}$. The quantization volume is denoted by V and ϵ_0 is the electric constant. The bosonic creation and annihilation operators for a photon with wave vector $\boldsymbol{k}$ and polarization λ are denoted by $a_{\boldsymbol{k},\lambda}$ and $a_{\boldsymbol{k},\lambda}^\dagger$, respectively. They obey the following commutation relation:

$$\left[a_{\boldsymbol{k},\lambda}, a_{\boldsymbol{k}',\lambda'}^\dagger \right] = \delta(\boldsymbol{k} - \boldsymbol{k}')\delta_{\lambda,\lambda'} .$$

All other commutators are zero. The electric field strength is defined as $\boldsymbol{E} = -\partial_t \boldsymbol{A} - \nabla\Phi$ and reads

$$\boldsymbol{E}(\boldsymbol{x}, t) = \sum_{\boldsymbol{k}} \sum_{\lambda} i\boldsymbol{\epsilon}_{\boldsymbol{k},\lambda} \sqrt{\frac{\hbar\omega_k}{2\epsilon_0 V}} \left(a_{\boldsymbol{k},\lambda} e^{i\boldsymbol{k}\boldsymbol{x} - i\omega_k t} - a_{\boldsymbol{k},\lambda}^\dagger e^{-i\boldsymbol{k}\boldsymbol{x} + i\omega_k t} \right) .$$

The Hamiltonian of the electromagnetic field is the sum of harmonic oscillators with angular frequency $\omega_{\boldsymbol{k},\lambda}$ that represent the single modes,

$$H = \sum_{\boldsymbol{k}} \sum_{\lambda} \hbar\omega_{\boldsymbol{k},\lambda} \left(a_{\boldsymbol{k},\lambda}^\dagger a_{\boldsymbol{k},\lambda} + \frac{1}{2} \right) .$$

The term $1/2$ is a constant vacuum energy and is usually neglected.

3.2. Quantum-mechanical fluctuations of a monochromatic electromagnetic field

We now focus on a linearly polarized single mode of the electromagnetic field in a one-dimensional cavity along the z-axis. Then, the electromagnetic field takes the following
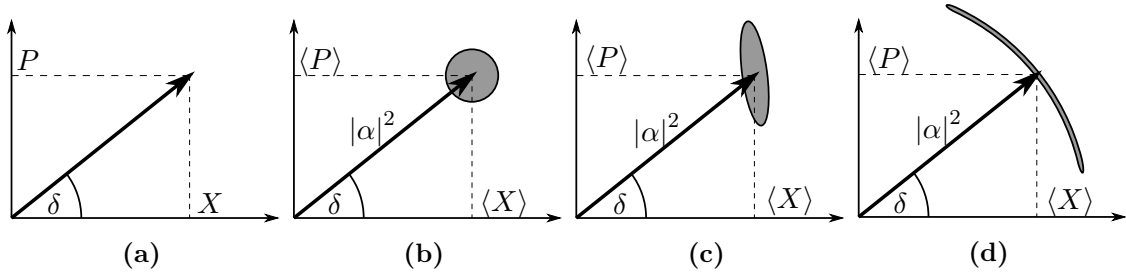
Figure 3.1.: Quadrature plot of **(a)** classical and **(b)** – **(d)** quantum-mechanical electromagnetic fields. The quantum-mechanical fields represent a coherent, a quadrature-squeezed, and a photon-number squeezed state, respectively. The gray area indicates the fluctuations due to the uncertainty relation $\left\langle (\Delta X)^2 \right\rangle \left\langle (\Delta P)^2 \right\rangle \geq 1/16$. Figures based on Ref. [21].

form [37]:

$$E(z,t) = \frac{E_0(z)}{2} \left(a e^{-i\omega t} + a^\dagger e^{i\omega t} \right) .$$

The indices $\boldsymbol{k}$ and λ have been dropped because only one mode is considered. The prefactor $E_0(z)$ describes the spatial variation of the field and the wave vector k must satisfy the boundary conditions of the cavity. By introducing the quadrature operators

$$X = \frac{1}{2} \left(a + a^\dagger \right) \quad \text{and} \quad P = \frac{1}{2i} \left(a - a^\dagger \right)$$

the electric field can be rewritten as

$$E(z,t) = E_0(z) \left(X \cos(\omega t) + P \sin(\omega t) \right) . \tag{3.1}$$

Such a monochromatic electromagnetic field is the output of an ideal single-mode laser.

For a classical electromagnetic field, X and P are real numbers which define its amplitude $\sqrt{X^2 + P^2}$ and its phase δ uniquely. In a quadrature plot, the state of a classical monochromatic electromagnetic field is represented by a constant phase vector (X, P), which is also called a phasor (Fig. 3.1a). In order to obtain the time-dependence of the electric field, the phasor is rotated around the origin at an angular frequency ω and its projection on the X axis is taken, according to Eq. (3.1).

The quantum-mechanical state with the same properties for the expectation value of the electric field operator, $\langle E \rangle$, is a coherent state $|\alpha\rangle$. Coherent states are eigenstates of the annihilation operator, $a |\alpha\rangle = \alpha |\alpha\rangle$. They have the following decomposition into photon-number Fock states,

$$|\alpha\rangle = e^{-|\alpha|^2/2} \sum_{n=0}^{\infty} \frac{\alpha^n}{\sqrt{n!}} |n\rangle = \sum_{n=0}^{\infty} \rho(n) |n\rangle .$$

From this equation it can be read off that a coherent state has a Poissonian photon statistics $\rho(n)$. The expectation values of the quadrature operators for a coherent state are $\langle X \rangle = |\alpha| \cos\delta$ and $\langle P \rangle = |\alpha| \sin\delta$, and the field amplitude is $\left\langle a^\dagger a \right\rangle = |\alpha|^2 = \sqrt{\langle X \rangle^2 + \langle P \rangle^2}$.

However, contrary to the classical case X and P are non-commuting operators, $[X, P] = i/2$, and, therefore, an uncertainty relation holds for any quantum mechanical state describing an electromagnetic field,

$$\left\langle (\Delta X)^2 \right\rangle \left\langle (\Delta P)^2 \right\rangle \geq \frac{1}{16} ,$$

where we introduced the fluctuation ΔO of an operator O around its expectation value, $\Delta O = O - \langle O \rangle$. The equality holds for so-called minimum uncertainty states, for instance, coherent states and the vacuum state. Hence, amplitude and phase of a quantum-mechanical monochromatic electromagnetic wave cannot be specified at arbitrary precision, but they must satisfy an uncertainty relation. Therefore, as a consequence of the fundamentals of quantum mechanics frequency-independent shot-noise in the amplitude and phase of an electromagnetic field arises. In the quadrature plot the classical phasor is replaced by an uncertainty region which is centered at the point $(\langle X \rangle, \langle P \rangle)$ and whose area is proportional to $\langle (\Delta X)^2 \rangle \langle (\Delta P)^2 \rangle$, shown in Fig. 3.1b.

3.3. Types of squeezed light

For coherent states and the vacuum state, the uncertainty region is a circle. However, it is possible to decrease the uncertainty along one direction in the quadrature plot at the cost of an increase of the uncertainty along another direction. This process is called squeezing. There are two different types of squeezed states, quadrature-squeezed states and photon-number squeezed states.

For quadrature-squeezed states the uncertainty circle is deformed into an ellipse, i.e., fluctuations along a given direction in the quadrature plot are reduced and they are increased along the perpendicular direction (Fig. 3.1c). Using quadrature-squeezed light, the sensitivity of interferometric experiments can be enhanced [22]. This is used, for instance, in gravitational wave detectors [23].

For photon-number squeezed states the uncertainty of the amplitude $\langle n \rangle$ is reduced at the cost of an increased phase uncertainty. Hence, the deformation of the uncertainty area is performed in a polar instead of a cartesian geometry (Fig. 3.1d). Photon-number squeezed light opens a way to improve the signal-to-noise ratio of Ramsey interferometry [27, 38]. In Chap. 5 we discuss a way to create photon-number squeezed light using quantum metamaterials as active lasing medium.

3.4. Fano factor

A measure for the squeezedness of a photon-number squeezed state is the Fano factor F, which is defined as the expectation value of the variance $\langle (\Delta n)^2 \rangle$ normalized to the field amplitude $\langle n \rangle$,

$$F = \frac{\langle n^2 \rangle - \langle n \rangle^2}{\langle n \rangle} \geq 0 \,. \tag{3.2}$$

For a thermal state, the Fano factor takes the value $F = \langle n \rangle + 1$. A Poissonian or coherent state corresponds to a Fano factor $F = 1$ and a photon-number squeezed state has $F < 1$. Photon-number squeezed states are also called sub-Poissonian. The Fano factor is used in Chap. 5 to quantify the squeezedness of the calculated photon statistics of the laser.

4. Disordered active lasing materials

In this chapter the influence of disorder in the atomic parameters on the photon-number expectation value of a laser is examined. In Sec. 4.1 we use the semiquantum approach introduced in Sec. 2.4 to derive a fixed point equation for the photon-number expectation value $\langle n \rangle_M$ of a M-atom lasing setup. In this setup each atom may have individual values for its lasing parameters. Disorder is modeled by a probability distribution that describes the spread of the lasing parameters around their intended mean values. In Sec. 4.2 we develop a method to calculate the mean photon-number expectation value $\overline{\langle n \rangle}_M$ for a given disorder probability distribution out of this fixed point equation. This method is exact in the limit of large numbers of atoms. We apply it for disorder in the atomic detuning Δ, the coupling strength g, and the pumping strength D_0 and we find that collective effects modify the lasing contribution of a single-atom and widen the range of parameters for which the system is in a lasing state. Therefore, multi-atom lasing setups acquire robustness against disorder.

In Sec. 4.3 the physical origin of this collective effect is analyzed. In a first step we show that in ordered M-atom lasing setups the minimal coupling strength required for lasing is lowered by a factor of $\sqrt{M}^{-1}$ and the maximum allowed detuning is enhanced by a factor of $\sqrt{M}$ compared to a single-atom laser. Likewise, the threshold pumping strength is lowered by a factor of M^{-1}. In order to describe disordered setups the fixed point equation is decomposed into a set of coupled single-atomic contributions $\langle n_i \rangle$ to the total photon-number expectation value $\langle n \rangle = \sum_{i=1}^{M} \langle n_i \rangle$, which have to be solved self-consistently. Using this decomposition we show that the widening of the range of lasing parameters is caused by an enhanced stimulated emission of each individual atom in a multi-atom lasing setup and that it is also present in disordered setups.

In the near future, quantum metamaterials are expected to have a rather small number of artificial atoms $M \lesssim 100$. Hence, the approximations made in Sec. 4.2 describe the mean photon number $\overline{\langle n \rangle}_M$ correctly, but significant sample-specific or quasistatic fluctuations of the actual photon number $\langle n \rangle_M$ around $\overline{\langle n \rangle}_M$ are expected. These fluctuations are examined numerically in Sec. 4.4.

4.1. Semiquantum approach

Within the semiquantum approach equations of motion for the expectation values of the photon number $\langle n \rangle \equiv \langle a^\dagger a \rangle$, the atomic polarization $\langle \sigma_z^j \rangle$, and the quantity $\langle \sigma_+^j a \rangle$ are considered. Using the M-atom Tavis-Cummings Hamiltonian (2.2) and Eq. (2.11) we obtain

$$\frac{\mathrm{d}}{\mathrm{d}t} \langle a^\dagger a \rangle = \sum_{j=1}^{M} ig_j \left(\langle \sigma_+^j a \rangle - \langle \sigma_-^j a^\dagger \rangle \right) - \kappa \left(\langle a^\dagger a \rangle - N_{\text{th}} \right) , \tag{4.1a}$$

$$\frac{\mathrm{d}}{\mathrm{d}t} \langle \sigma_z^j \rangle = 2ig_j \left(\langle \sigma_-^j a^\dagger \rangle - \langle \sigma_+^j a \rangle \right) - \Gamma_{1,j} \langle \sigma_z^j \rangle + \Gamma_{1,j} D_{0,j} , \tag{4.1b}$$

$$\frac{\mathrm{d}}{\mathrm{d}t}\left\langle\sigma_+^j a\right\rangle = -\left(\Gamma_{\kappa,j} - i\Delta_j\right)\left\langle\sigma_+^j a\right\rangle - ig_j\left\langle\sigma_z^j a^\dagger a\right\rangle - i\frac{g_j}{2}\left(1 + \left\langle\sigma_z^j\right\rangle\right) \tag{4.1c}$$

$$- \sum_{k=1}^{M} ig_k\left\langle\sigma_+^j\sigma_-^k\right\rangle\left(1 - \delta_{k,j}\right).$$

Some approximations are performed in order to get a closed system of differential equations. First, direct atomic interactions are neglected, i.e., $\left\langle\sigma_+^j\sigma_-^k\right\rangle = 0$ for $j \neq k$. Second, correlations of the diagonal atomic operator σ_z^j and the photon-number operator $a^\dagger a$ are neglected, $\left\langle\sigma_z^j a^\dagger a\right\rangle \approx \left\langle\sigma_z^j\right\rangle\left\langle a^\dagger a\right\rangle$. Contrary to the semiclassical approach discussed in Sec. 2.5 the expectation value $\left\langle\sigma_+^j a\right\rangle$ is not factorized, hence, correlations of $\sigma_\pm$ and $a^{(\dagger)}$ are now accounted for in the calculation. Third, like for the semiclassical model an adiabatic approximation holds because for typical lasing parameters the resonator decay rate κ is much smaller than the atomic pumping, relaxation, and dephasing rates $\Gamma_\uparrow$, $\Gamma_\downarrow$, and Γ_φ^*. Therefore, atomic and resonator processes are decoupled by inserting the stationary solution of Eq. (4.1c) into Eqs. (4.1a) and (4.1b). We obtain the following rate equations for the photon number $\langle n\rangle \equiv \left\langle a^\dagger a\right\rangle$ and the atomic polarization:

$$\frac{\mathrm{d}}{\mathrm{d}t}\langle n\rangle = \sum_{j=1}^{M} 2g_j^2\frac{\Gamma_{\kappa,j}}{\Gamma_{\kappa,j}^2 + \Delta_j^2}\left(\left\langle\sigma_z^j\right\rangle\langle n\rangle + \frac{1}{2}\left(1 + \left\langle\sigma_z^j\right\rangle\right)\right) - \kappa\langle n\rangle + \kappa N_{\mathrm{th}}, \tag{4.2a}$$

$$\frac{\mathrm{d}}{\mathrm{d}t}\langle\sigma_z\rangle = -4g_j^2\frac{\Gamma_{\kappa,j}}{\Gamma_{\kappa,j}^2 + \Delta_j^2}\left(\left\langle\sigma_z^j\right\rangle\langle n\rangle + \frac{1}{2}\left(1 + \left\langle\sigma_z^j\right\rangle\right)\right) - \Gamma_{1,j}\left\langle\sigma_z^j\right\rangle + \Gamma_{1,j}D_{0,j}. \tag{4.2b}$$

In contrast to the semiclassical model the semiquantum approach accounts for a thermal photon number N_{th} in the resonator and for spontaneous emission, which is described by the terms proportional to $(1 + \left\langle\sigma_z^j\right\rangle)/2$ in Eq. (4.2). The terms proportional to $\left\langle\sigma_z^j\right\rangle\langle n\rangle$ describe the stimulated emission of photons by atom j.

Using the adiabatic approximation a second time the stationary solution of Eq. (4.2b) is plugged into Eq. (4.2a), yielding a fixed point equation that implicitly defines the photon-number expectation value $\langle n\rangle$,

$$\langle n\rangle = N_{\mathrm{th}} + \sum_{j=1}^{M} \beta_j\frac{D_{0,j}\left(\langle n\rangle + \frac{1}{2}\right) + \frac{1}{2}}{\Gamma_{\kappa,j}^2 + \Delta_j^2 + \alpha_j\left(\langle n\rangle + \frac{1}{2}\right)}, \tag{4.3}$$

where the factors α_j and β_j are defined to be

$$\alpha_j = 4g_j^2\frac{\Gamma_{\kappa,j}}{\Gamma_{1,j}} \quad\text{and}\quad \beta_j = 2g_j^2\frac{\Gamma_{\kappa,j}}{\kappa}.$$

The photon-number expectation value $\langle n\rangle$ appears on the right-hand side of the fixed point equation because of the terms that describe stimulated emission in Eq. (4.2). In the following, the solution of Eq. (4.3) is denoted by $\langle n\rangle_M$, where M is the number of atoms in the setup. Within this thesis, numerical solutions of fixed point equations are obtained using the `FindRoot` function implemented in WOLFRAM MATHEMATICA, version 9.0.1.0.

Considering the limit $\langle n\rangle \to \infty$ on the right-hand side of Eq. (4.3) we obtain the maximum photon number that can be reached for given pumping and decay rates,

$$\langle n\rangle_M^{\mathrm{max}} = N_{\mathrm{th}} + \sum_{j=1}^{M} \frac{\Gamma_{\uparrow,j} - \Gamma_{\downarrow,j}}{2\kappa}. \tag{4.4}$$
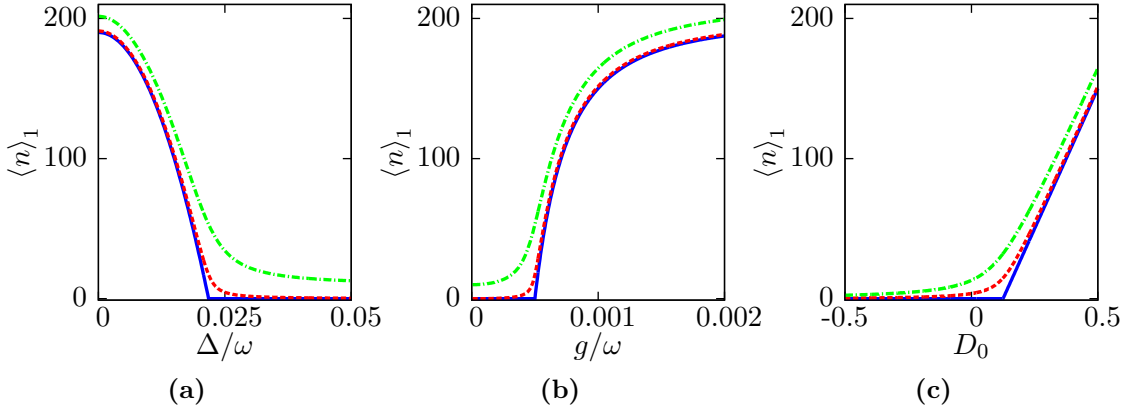
Figure 4.1.: Photon-number expectation value $\langle n \rangle_1 (\Delta, g, D_0)$ for a single-atom laser. **(a):** $\langle n \rangle_1 (\Delta, g, D_0)$ as function of the detuning Δ for a coupling strength $g = 0.001\,\omega$ and a pumping strength $D_0 = 0.5$. **(b):** $\langle n \rangle_1 (\Delta, g, D_0)$ as function of the coupling strength g for a detuning $\Delta = 0.01\,\omega$ and a pumping strength $D_0 = 0.5$. **(c):** $\langle n \rangle_1 (\Delta, g, D_0)$ as function of the pumping strength D_0 for a detuning $\Delta = 0.01\,\omega$ and a coupling strength $g = 0.001\,\omega$. Solid blue lines are the results obtained out of the semiclassical theory, dashed red and dash-dotted green lines represent the results obtained out of the semiquantum theory for a thermal photon number $N_{\mathrm{th}} = 0$ and $N_{\mathrm{th}} = 10$, respectively. Plot parameters are $\Gamma_1 = 0.008\,\omega$, $\Gamma_\varphi^* = 0.001\,\omega$, and $\kappa = 1 \times 10^{-5}\,\omega$.

For a single-atom laser Eq. (4.3) is solved by the following single-atom lasing curve:

$$\langle n \rangle_1 = X + \sqrt{X^2 + N_{\mathrm{th}}\tilde{n}_0 + \frac{N_{\mathrm{th}}}{2} + \frac{\Gamma_1}{4\kappa}(D_0 + 1)}, \tag{4.5}$$

$$X = -\frac{1}{4} + \frac{N_{\mathrm{th}}}{2} + \frac{D_0 \Gamma_1}{4\kappa} - \frac{\tilde{n}_0}{2},$$

$$\tilde{n}_0 = \frac{\Gamma_1}{4g^2} \frac{\Gamma_\kappa^2 + \Delta^2}{\Gamma_\kappa}. \tag{4.6}$$

The subscript j at the rates and the coupling strength has been dropped as only one atom is considered. By $\tilde{n}_0$ we denote the photon saturation number derived from the semiquantum theory. Compared to the semiclassical photon saturation number $\tilde{n}_0^{\mathrm{sc}}$, defined in Eq. (2.13), $\Gamma_\varphi = \Gamma_1/2 + \Gamma_\varphi^*$ has been extended to $\Gamma_\kappa = \Gamma_\varphi + \kappa/2$. Typical lasing parameters satisfy $\kappa \ll \Gamma_\uparrow, \Gamma_\downarrow, \Gamma_\varphi^*$, hence the difference is negligible and we have $\tilde{n}_0^{\mathrm{sc}} \approx \tilde{n}_0$.

In Fig. 4.1 the single-atom lasing curves $\langle n \rangle_1$ obtained out of the semiclassical and the semiquantum theory are compared. The semiclassical theory (solid blue curves) predicts a sharp, kink-like transition from a state with zero photons in the resonator to a lasing state. In the semiquantum theory (dashed red curves) this is replaced by a smeared-out crossover. However, the lasing threshold of the semiclassical theory, derived in Sec. 2.5, provides a good estimate for the position of this crossover. Semiclassical and semiquantum theory yield identical results for large photon numbers if thermal photons in the resonator are neglected, $N_{\mathrm{th}} = 0$. A nonzero thermal photon number in the resonator increases the semiquantum photon expectation value by N_{th} and slightly broadens the lasing crossover region (dash-dotted green curves).

4.2. Mean photon-number expectation value for large systems

In order to study disorder in the lasing system we introduce a probability distribution $p(\Delta, g, \dots)$ that models the spread of the different lasing parameters around their intended mean values. There are several ways to relate the photon-number expectation value $\langle n \rangle_M$ to the parameters of the probability distribution p:

- For a small system size, $M \leq 3$, the fixed point equation (4.3) can be solved analytically and the result can be averaged over p. This approach is not suitable to study large quantum metamaterials.

- For any system size M a set of lasing parameters $\{\Delta_j\}, \{g_j\}, \ldots$ can be chosen randomly according to the probability distribution p. This represents a realization of a particular M-atom lasing system and Eq. (4.3) can be solved numerically for this particular set of parameters. Statistical information is acquired by averaging over a large ensemble of randomly chosen lasing systems. This approach is used in Sec. 4.4 to study fluctuations of $\langle n \rangle_M$ around its mean value $\overline{\langle n \rangle}_M$ that arise because of a finite system size M.

- Information on the mean value $\overline{\langle n \rangle}_M$ can be acquired on a numerically less demanding way: If the system size M is large enough, the sum in Eq. (4.3) can be rewritten as an integral over the probability distribution p. A modified fixed point equation is obtained which depends on the parameters of p and is solved numerically. This approach is justified and used in the following.

An alternative approach is to reformulate Eq. (4.3) as a set of modified single-atom lasing equations that have to be solved self-consistently. This reformulation gives further insight into the physics of the problem and is discussed in Sec. 4.3.2.

We now pursue the third way and derive a fixed point equation for the mean photon-number expectation value $\overline{\langle n \rangle}_M$. For large numbers of atoms, $M \gg 1$, the sum over individual atoms can be replaced by an integral: As the labeling of the individual atoms is arbitrary, they can be resorted by their lasing parameters, for instance, by increasing detuning and coupling strength. For a sufficiently large system size M, the number of atoms within a certain range of lasing parameters, e.g., $[\Delta_0, \Delta_0 + \delta\Delta] \times [g_0, g_0 + \delta g]$, is approximately given by $Mp(\Delta_0, g_0)\delta\Delta\delta g$, where $p(\Delta, g)$ is the underlying probability distribution of the lasing parameters of a single atom. Therefore, we perform the following replacement in Eq. (4.3):

$$\sum_{j=1}^{M} \cdots = M \iint \mathrm{d}\Delta \, \mathrm{d}g \ldots p(\Delta, g, \ldots) \ldots . \tag{4.7}$$

The system size M required to sample p sufficiently well depends on the width of p. If M is chosen too small, large sample-to-sample fluctuations of $\langle n \rangle_M$ arise. Such fluctuations are studied in Sec. 4.4.

Having rewritten the sum we obtain the following form of Eq. (4.3):

$$\langle n \rangle = N_{\mathrm{th}} + M \iint \mathrm{d}\Delta \, \mathrm{d}g \ldots p(\Delta, g, \ldots) \beta \frac{D_0\left(\langle n \rangle + \frac{1}{2}\right) + \frac{1}{2}}{\Gamma_\kappa^2 + \Delta^2 + \alpha\left(\langle n \rangle + \frac{1}{2}\right)} . \tag{4.8}$$

The integration yields a modified fixed point equation for $\overline{\langle n \rangle}_M$, which is solved numerically.

In the following, disorder in only one lasing parameter at a time is considered. A Gaussian and a box distribution are used, which allow to solve the integrals analytically,

$$p_{\mathrm{G}}(x) = \frac{1}{\sqrt{2\pi}\sigma} \exp\left(-\frac{(x-\mu)^2}{\sigma^2}\right) ,$$

$$p_{\mathrm{B}}(x) = \frac{1}{b}\left[\Theta\left(x - \mu + \frac{b}{2}\right) - \Theta\left(x - \mu - \frac{b}{2}\right)\right] .$$

Here x is the variable to be averaged over, μ is its mean value and σ is its standard deviation. The width of the box distribution is b, which is related to its standard deviation via

$$b = \sqrt{12}\sigma .$$

By $\Theta(x)$ we denote the Heaviside step function, which is equal to unity for $x \geq 0$ and zero otherwise.

Typically, there are restrictions in the allowed range of values of the lasing parameters. For instance, the coupling strength g_j and the level-splitting energy ϵ_j should be positive and, therefore, the detuning should suffice $\Delta_j \geq -\omega$. These conditions put constraints on the allowed values of the disorder standard deviation σ. If a Gaussian distribution $p_{\mathrm{G}}(x)$ is used, the standard deviation σ must be chosen such that the area of the tail of the distribution below a minimal value $x_{\min}$ does not exceed a certain ratio ϵ of the total area of the distribution. The area of this tail is given by the cumulative distribution function

$$P_{\mathrm{G}}(x) = \int_{-\infty}^{x} p_{\mathrm{G}}(t)\mathrm{d}t = \frac{1}{2}\operatorname{erfc}\left(\frac{\mu - x}{\sqrt{2}\sigma}\right),$$

where erfc denotes the complementary error function. Now we can reformulate the condition $P(x_{\min}) \leq \epsilon$ as a threshold for the disorder standard deviation σ:

$$\sigma \leq \frac{\mu - x_{\min}}{\sqrt{2}\operatorname{erfc}^{-1}(2\epsilon)}. \tag{4.9}$$

If x is bound by an upper value $x_{\max}$, the corresponding threshold for σ is given by

$$\sigma \leq \frac{x_{\max} - \mu}{\sqrt{2}\operatorname{erfc}^{-1}(2\epsilon)}.$$

For the box distribution the width b can be increased up to $x_{\min} - \mu + b/2 = 0$ or $x_{\max} - \mu - b/2 = 0$. These conditions yield

$$\sigma \leq \frac{\mu - x_{\min}}{\sqrt{3}} \quad \text{or} \quad \sigma \leq \frac{x_{\max} - \mu}{\sqrt{3}}, \tag{4.10}$$

respectively.

In the following subsections we use Eq. (4.8) to calculate the mean photon-number expectation value $\overline{\langle n \rangle}_M$ for disorder in the detuning, the coupling strength, and the pumping.

4.2.1. Disorder in the detuning

In this section disorder in the atomic detuning Δ is investigated. The mean detuning be $\overline{\Delta} = 0$, i.e., the atoms ideally be on resonance. Having performed the integration in Eq. (4.8) we obtain the following fixed point equation for the photon-number expectation value $\langle n \rangle$:

$$\langle n \rangle = N_{\mathrm{th}} + M\beta\left[D_0\left(\langle n \rangle + \frac{1}{2}\right) + \frac{1}{2}\right]I\left(\zeta_{\langle n \rangle}\right), \tag{4.11}$$

$$\zeta_{\langle n \rangle} = \sqrt{\Gamma_\kappa^2 + \alpha\left(\langle n \rangle + \frac{1}{2}\right)}.$$

The integrals $I(\zeta)$ for the two types of distributions are given by

$$I_{\mathrm{G}}(\zeta) = \sqrt{\frac{\pi}{2}}\frac{1}{\zeta\sigma_\Delta}\exp\left(\frac{\zeta^2}{2\sigma_\Delta^2}\right)\operatorname{erfc}\left(\frac{\zeta}{\sqrt{2}\sigma_\Delta}\right),$$

$$I_{\mathrm{B}}(\zeta) = \frac{1}{\sqrt{3}\zeta\sigma_\Delta}\arctan\left(\frac{\sqrt{3}\sigma_\Delta}{\zeta}\right).$$

Again, erfc denotes the complementary error function.
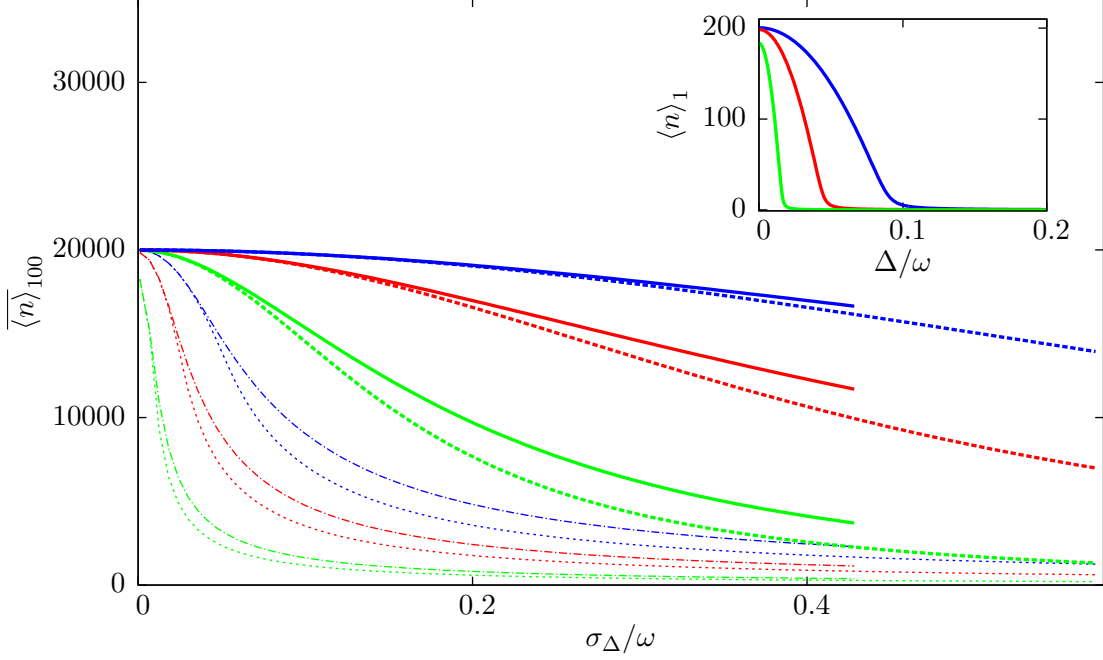
Figure 4.2.: Photon-number expectation value $\overline{\langle n \rangle}_{100}(\sigma_\Delta)$ for a lasing setup with $M = 100$ atoms and disorder in the atomic detuning Δ. Thick solid lines are calculated for a Gaussian disorder distribution with mean detuning $\overline{\Delta} = 0$ and standard deviation σ_Δ, thick dashed lines represent a box distribution with the same parameters. In oder to avoid unphysical values of the detuning the results for the Gaussian distribution are plotted only for $\sigma_\Delta \leq 0.43\,\omega$. **Inset**: Single-atom lasing curves $\langle n \rangle_1(\Delta)$. The remarkably slow decrease of $\overline{\langle n \rangle}_{100}(\sigma_\Delta)$ cannot be explained by averaging the single-atomic resonance curves over the same probability distributions, which yields $\overline{\langle n \rangle}_M^{\text{bare}}$ represented by the curves plotted with thin lines in the main plot. The thin dash-dotted and dotted lines correspond to a Gaussian and a box distribution, respectively. Plot parameters are $\Gamma_\uparrow = 0.006\,\omega$, $\Gamma_\downarrow = 0.002\,\omega$, $\Gamma_\varphi^* = 0.001\,\omega$, $\kappa = 1 \times 10^{-5}\,\omega$, and $N_{\text{th}} = 0$. Blue curves $g = 0.004\,\omega$, red curves $g = 0.002\,\omega$, and green curves $g = 0.00075\,\omega$.

In Fig. 4.2 numerical results for the mean photon-number expectation value $\overline{\langle n \rangle}_M$ are shown for a $M = 100$ atom lasing setup and the two types of distribution $p_{\text{G/B}}(\Delta)$ (thick solid and dashed lines, respectively). Three different coupling strengths to the resonator are used, corresponding to the different colors. The level splitting energy ϵ_j of each atom should be positive and, therefore, the atomic detuning must fulfill $\Delta_j \geq -\omega$. Equations (4.9) and (4.10) yield the following constraints on the standard deviation σ_Δ:

$$\sigma_\Delta \lesssim 0.430\,\omega \text{ for the Gaussian distribution and } \epsilon = 0.01,$$
$$\sigma_\Delta \lesssim 0.577\,\omega \text{ for the box distribution.}$$

The results for $\overline{\langle n \rangle}_M$ for the two types of distribution are plotted up to these different maximum values of the disorder standard deviation in Fig. 4.2.

Remarkably, the mean photon-number expectation value $\overline{\langle n \rangle}_{100}$ in Fig. 4.2 decreases only weakly with increasing disorder standard deviation σ_Δ. The magnitude of the decrease depends on the coupling strength g. Up to $\sigma_\Delta = 0.2\,\omega$ the setup is still operating at at least 40% of the maximal photon number obtained for an ordered setup, which is given by the limit $\sigma_\Delta \to 0$. This reveals that the lasing activity of an atom changes significantly compared to the single-atom lasing curve $\langle n \rangle_1$ if the atom is part of a multi-atom lasing setup. The bare single-atom lasing curves $\langle n \rangle_1$ are given by Eq. (4.5) and are shown in the inset of Fig. 4.2. In order to compare the expected lasing behavior based on these bare

single-atom lasing curves $\langle n \rangle_1$ with the numerical results for $\overline{\langle n \rangle}_M$, we average $\langle n \rangle_1$ over the same disorder distribution,

$$\overline{\langle n \rangle}_M^{\text{bare}}(\sigma_\Delta) = M \int \mathrm{d}\Delta \, p(\Delta) \, \langle n \rangle_1(\Delta) \,.$$

The thin lines in Fig. 4.2 represent the results for $\overline{\langle n \rangle}_M^{\text{bare}}(\sigma_\Delta)$. They decrease much faster than $\overline{\langle n \rangle}_M(\sigma_\Delta)$ because the fraction of atoms at a detuning larger than the single-atom lasing threshold, $\Delta_j > \Delta_{\max}(1)$, grows with increasing disorder standard deviation. These atoms are expected not to contribute to the lasing process any more and the photon-number expectation value $\overline{\langle n \rangle}_M^{\text{bare}}$ decreases accordingly. The observed slow decrease of $\overline{\langle n \rangle}_M$ indicates that the atoms in a multi-atom lasing setup tolerate a much larger detuning than a single-atom, while they are still participating in the lasing process.

As a second observation, the mean photon expectation values $\overline{\langle n \rangle}_{100}$ and $\overline{\langle n \rangle}_{100}^{\text{bare}}$ differ for a weak coupling strength $g = 0.00075\,\omega$ in the limit $\sigma_\Delta \to 0$. According to the green single-atom lasing curve $\langle n \rangle_1(\Delta)$ in the inset we expect a maximum contribution to the overall photon number of $\langle n \rangle_1(\Delta = 0) \approx 183$ photons by a weakly coupled resonant single atom. But we actually observe a larger contribution per atom of $\overline{\langle n \rangle}_{100}(\sigma_\Delta \to 0)/100 \approx 200$ photons in the multi-atom lasing setup.

Finally, the results obtained for a Gaussian and a box distribution coincide for small disorder standard deviations $\sigma_\Delta \lesssim 0.1\,\omega$. For sufficiently narrow distributions the actual shape of the distribution does not matter any more. This effect is discussed in the Appendix A.

In conclusion, the observed slow decrease of $\overline{\langle n \rangle}_M$ implies that atoms in a multi-atom lasing setup are described by an effective lasing curve which differs from the bare single-atom lasing curve $\langle n \rangle_1$, given by Eq. (4.5), in the following aspects:

1. The lasing curve as a function of the detuning is broadened, i.e., the range of tolerable atomic detuning is increased in the multi-atom lasing setup.

2. The lasing activity of resonant atoms at a weak coupling strength is enhanced, i.e., resonant atoms in a multi-atom lasing setup emit more photons into the resonator than predicted by the bare single-atom lasing curve $\langle n \rangle_1(\Delta = 0)$.

The reason for this behavior is discussed in Sec. 4.3.2.

4.2.2. Disorder in the coupling strength

Disorder in the coupling strength g between the atoms and the resonator is examined similarly to the previous subsection. Having performed the integration over the coupling strength g in Eq. (4.8) the fixed point equation takes the following form:

$$\langle n \rangle = N_{\text{th}} + \frac{M\Gamma_1}{2\kappa} \left(D_0 + \frac{1}{2\langle n \rangle + 1} \right) I\left(c_{\langle n \rangle}\right) , \tag{4.12}$$

$$c_{\langle n \rangle} = \sqrt{\frac{\Gamma_1(\Gamma_\kappa^2 + \Delta^2)}{4(\langle n \rangle + 1/2)\Gamma_\kappa}} \,,$$

where the integrals are given by

$$I_{\text{G}}(c) = 1 - \pi c V(\overline{g}, \sigma_g, c) \,,$$

$$I_{\text{B}}(c) = 1 - \frac{c}{\sqrt{12}\sigma_g} \left[\arctan\left(\frac{\overline{g} + \sqrt{3}\sigma_g}{c}\right) - \arctan\left(\frac{\overline{g} - \sqrt{3}\sigma_g}{c}\right) \right] \,.$$

(a) Mean coupling strength $\overline{g} = 0.001\,\omega$ close to the single-atom lasing threshold
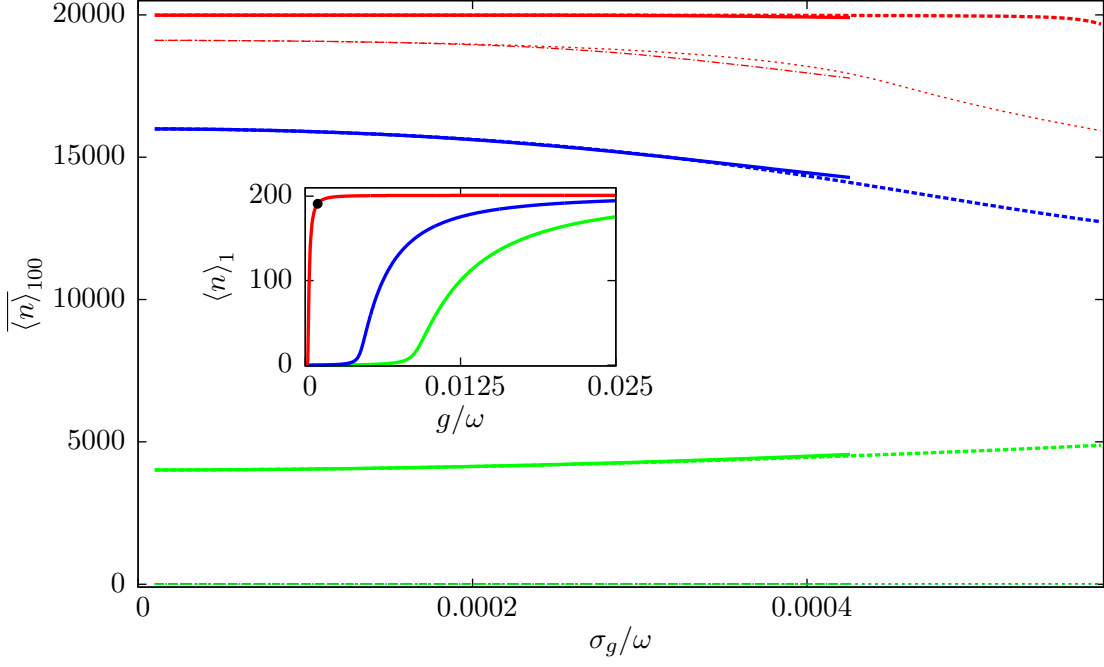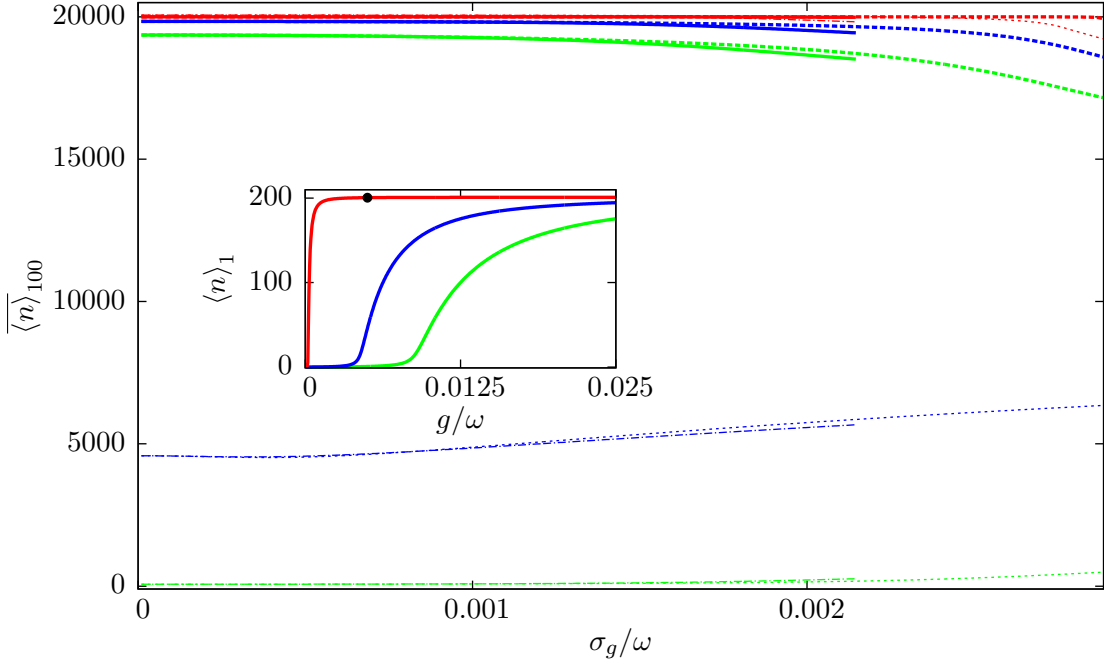
(b) Mean coupling strength $\overline{g} = 0.005\,\omega$ above the single-atom lasing threshold

Figure 4.3.: Photon-number expectation value $\overline{\langle n \rangle}_{100}(\sigma_g)$ for a lasing setup with $M = 100$ atoms and disorder in the coupling strength g. Thick solid lines are calculated for a Gaussian disorder distribution with mean coupling strength $\overline{g}$ and standard deviation σ_g, thick dashed lines represent a box distribution with the same parameters. In order to avoid unphysical values of the coupling strength, the results for the Gaussian distribution are only plotted up to a maximum disorder standard deviation $\sigma_\mathrm{g} = 4.3 \times 10^{-4}\,\omega$ and $\sigma_\mathrm{g} = 2.15 \times 10^{-3}\,\omega$, respectively. **Inset**: Single-atom lasing curves $\langle n \rangle_1(g)$. The remarkably slow decrease of $\overline{\langle n \rangle}_{100}(\sigma_g)$ cannot be explained by an average of the single-atomic lasing curves $\langle n \rangle_1(g)$ over the same probability distributions, which yields $\overline{\langle n \rangle}_M^{\mathrm{bare}}$ represented by the thin curves. The thin dash-dotted an dotted curves correspond to a Gaussian and a box disorder distribution, respectively. Plot parameters are $\Gamma_\uparrow = 0.006\,\omega$, $\Gamma_\downarrow = 0.002\,\omega$, $\Gamma_\varphi^* = 0.001\,\omega$, $\kappa = 1 \times 10^{-5}\,\omega$, and $N_\mathrm{th} = 0$. Red curves $\Delta = 0\,\omega$, blue curves $\Delta = 0.1\,\omega$, and green curves $\Delta = 0.2\,\omega$.

V is the Voigt function

$$V(\overline{g}, \sigma_g, x) = \sqrt{\frac{\pi}{2}} \frac{1}{2\pi\sigma_g} \exp\left[\left(\frac{x - i\overline{g}}{\sqrt{2}\sigma_g}\right)^2\right] \text{erfc}\left(\frac{x - i\overline{g}}{\sqrt{2}\sigma_g}\right) + \text{c.c.} \, .$$

In Fig. 4.3 numerical results for the mean photon-number expectation value $\overline{\langle n \rangle}_M$ are shown for a setup consisting of $M = 100$ atoms and the two types of distribution $p_{G/B}(g)$ (thick solid and dashed lines, respectively). Figure 4.3a corresponds to a mean coupling strength $\overline{g} = 0.001\,\omega$ close to the single-atom lasing transition, Fig. 4.3b to a mean coupling strength $\overline{g} = 0.005\,\omega$ above the single-atom lasing transition. The value of $\overline{g}$ is indicated by a black circle at the single-atom lasing curves $\langle n \rangle_1$ in the insets. Three different values for the atomic detuning are used, corresponding to the different colors.

Again, the range of physically reasonable values of the disorder standard deviation σ_g is restricted. The coupling strength $g \geq 0$ be positive, which imposes via Eqs. (4.9) and (4.10) the following constraints on σ_g for $\overline{g} = 0.001\,\omega$:

$$\sigma_g \lesssim 4.30 \times 10^{-4}\,\omega \text{ for the Gaussian distribution and } \epsilon = 0.01,$$
$$\sigma_g \lesssim 5.77 \times 10^{-4}\,\omega \text{ for the box distribution.}$$

Likewise, for $\overline{g} = 0.005\,\omega$ we obtain

$$\sigma_g \lesssim 2.15 \times 10^{-3}\,\omega \text{ for the Gaussian distribution and } \epsilon = 0.01,$$
$$\sigma_g \lesssim 2.89 \times 10^{-3}\,\omega \text{ for the box distribution.}$$

In Fig. 4.3 the results for $\overline{\langle n \rangle}_M$ are plotted up to these different maximum values of the disorder standard deviation.

Like for disorder in the detuning, $\overline{\langle n \rangle}_{100}(\sigma_g)$ is remarkably independent of the disorder standard deviation σ_g over a quite large range of values. The results cannot be explained by the properties of the bare single-atom lasing curves $\langle n \rangle_1$, given by Eq. (4.5) and shown in the insets of Fig. 4.3. For comparison we average these bare single-atom lasing curves $\langle n \rangle_1$ over the same disorder distribution and obtain

$$\overline{\langle n \rangle}_M^{\text{bare}}(\sigma_g) = M \int \text{d}g \; p(g) \, \langle n \rangle_1(g) \, ,$$

which corresponds to the thin lines in Fig. 4.3.

In a first step we compare the photon-number expectation value $\overline{\langle n \rangle}_M(\sigma_g)$ to the average $\overline{\langle n \rangle}_M^{\text{bare}}(\sigma_g)$ for resonant atoms at a mean coupling strength $\overline{g}$ close to the single-atom lasing transition (red curves in Fig. 4.3a). The average over the bare single-atom lasing curves predicts a smaller photon-number expectation value, $\overline{\langle n \rangle}_M^{\text{bare}} < \overline{\langle n \rangle}_M$, because some atoms have a very small coupling strength $g < \overline{g}$ and, therefore, do not contribute significantly to the lasing process. However, we observe that the contribution of each atom to the photon number is actually $\overline{\langle n \rangle}_{100}/100 \approx 200$ photons, i.e., all atoms emit the maximum possible photon number irrespective of the individual coupling strength g. This is a hint that the collective lasing threshold coupling strength $g_{\min}$ in the multi-atom setup is actually much lower than the corresponding value in a single-atom lasing setup.

The lowering of the threshold coupling strength and, therefore, an enhancement of the lasing activity per atom in the multi-atom lasing setup is even more obvious for the blue and green curves in Fig. 4.3a, corresponding to a detuning $\Delta = 0.1\,\omega$ and $\Delta = 0.15\,\omega$, respectively. For these values of the detuning the single-atom lasing resonance curves

predict no lasing at all, whereas the multi-atom setup is still operating at approximately 80% and 20% of its maximum photon number, respectively. Even an increase of the average photon-number expectation value $\overline{\langle n \rangle}_M$ as a function of the disorder standard deviation σ_g is observed for $\Delta = 0.15\,\omega$.

In a typical lasing experiment the laser is operated far above the lasing threshold of a single resonant atom. The results corresponding to this parameter regime are shown in Fig. 4.3b. For resonant atoms far above the lasing threshold, $\overline{\langle n \rangle}_M^{\mathrm{bare}}$ and $\overline{\langle n \rangle}_M$ coincide for almost all values of the disorder standard deviation σ_g. However, for detuned atoms, $|\Delta| > 0$, the bare single-atom lasing curves predict a small or even close to zero photon number whereas the actual mean photon-number expectation value $\overline{\langle n \rangle}_M$ is still close to the maximum photon number of approximately 20000 photons and depends surprisingly weakly on the detuning Δ.

In conclusion, also for disorder in the coupling strength the effective contribution of each atom in a multi-atom lasing setup to the overall photon number differs from the bare single-atom lasing curve $\langle n \rangle_1$:

1. The lasing-threshold coupling strength g_{min} in a multi-atom setup is lowered compared to its value in a single-atom setup.

2. The lasing activity of detuned atoms is enhanced, i.e., detuned atoms in a multi-atom lasing setup emit more photons into the resonator than expected from the single-atomic lasing curve $\langle n \rangle_1$.

An explanation for this observations is given in Sec. 4.3.2.

4.2.3. Disorder in the pumping strength

Finally, disorder in the pumping strength is considered. A measure for the pumping strength is the stationary atomic polarization

$$D_0 = \frac{\Gamma_\uparrow - \Gamma_\downarrow}{\Gamma_\uparrow + \Gamma_\downarrow}\,.$$

It is a function of the pumping and relaxation rates $\Gamma_\uparrow$ and $\Gamma_\downarrow$. These rates appear in Eq. (4.8) via the expression D_0, but also via the total relaxation rate $\Gamma_1 = \Gamma_\uparrow + \Gamma_\downarrow$. Therefore, in principle disorder in D_0 has to be modeled by disorder in the pumping and relaxation rates, which instantaneously implies disorder in Γ_1, too. However, in this section we concentrate on disorder in D_0 only, while Γ_1 is assumed to be constant.

Experimental motivation for considering only disorder in D_0

A motivation for this step is provided by experiments, for instance, the laser constructed out of a superconducting single-electron transistor (SSET) presented in Ref. [6]. A sketch of the circuit is shown in Fig. 4.4. The SSET consists of a charge qubit whose island (I) is connected by an additional Josephson junction to a drain electrode (D). The electric potential of this additional electrode can be adjusted by the voltage source V_D in order to allow for single-electron tunneling from the island to the drain electrode. This establishes a pumping process. Furthermore, the island of the qubit is capacitively coupled to a coplanar-waveguide resonator, which acts as a laser cavity. The system is described by the following Hamiltonian:

$$H_{\mathrm{SSET}} = E_C(N - N_G)^2 - E_J \cos(\phi_L) - eV_D N_R + g(N-1)(a + a^\dagger) + \omega a^\dagger a\,.$$

Here E_C is the charge energy of the island, N is the number of electrons on the island, N_R is the number of electrons that tunneled from the island to the drain electrode, and N_G is
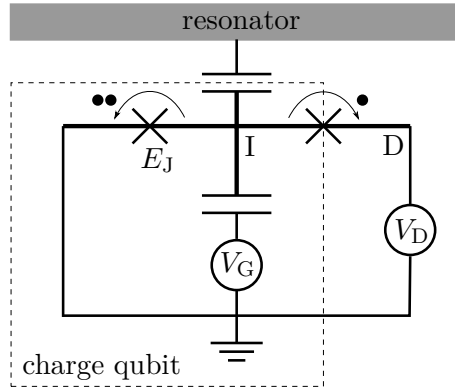
Figure 4.4.: Circuit of a superconducting single-electron transistor (SSET). The SSET is a charge qubit (dashed box) where the superconducting island (I) is connected to an additional drain electrode (D) by a second Josephson junction. For a suitable drain voltage V_D single electrons tunnel from the island to the drain. Figure based on Ref. [6].

the number of control charges on the island, which is adjusted by the external voltages V_G and V_D. The superconducting phase difference across the left Josephson junction separating the island from ground is denoted by ϕ_L. It is the conjugated variable to N. As usual, ω is the frequency of the resonator and a ($a^\dagger$) are the annihilation (creation) operators of the radiation field. By choosing E_J appropriately one can restrict the system to the three eigenstates with lowest energy. Diagonalization of this restricted Hamiltonian yields

$$H = \frac{1}{2}\delta E \sigma_z + E_C(1 - N_G)^2 \left|1\right\rangle\left\langle1\right| + \text{const},$$

with $\delta E = \sqrt{16(N_G - 1)^2 E_C^2 + E_J^2}$. The eigenstates are given by

$$\left|\uparrow\right\rangle = \cos\frac{\theta}{2}\left|0\right\rangle - \sin\frac{\theta}{2}\left|2\right\rangle,$$
$$\left|\uparrow\right\rangle = \sin\frac{\theta}{2}\left|0\right\rangle + \cos\frac{\theta}{2}\left|2\right\rangle,$$
$$\left|1\right\rangle,$$

where $\left|N\right\rangle$ is the state with N electrons on the island and the mixing angle θ is defined by $\tan\theta = -E_J/(4(N_G - 1)E_C)$. Charge noise in the SSET causes quasistatic fluctuations of the angle θ on a timescale of hours, which translates into a change of the eigenstates. The pumping process is described by the following quasiparticle tunneling Hamiltonian:

$$H_{qp} = \sum_{i,k} T_{i,k}\gamma_{i,I}\gamma_{k,D}^\dagger e^{-i\phi_R/2} + \text{h.c.},$$

where $T_{i,k}$ are the tunneling coefficients and γ_j ($\gamma_j^\dagger$) are the quasiparticle annihilation (creation) operators for the mode i on the island (I) and the drain (D), respectively. Using Fermi's golden rule the following dependence of the transition rates on the mixing angle is found:

$$\Gamma_{\uparrow\to1} \propto \sin^2\frac{\theta}{2}, \qquad\qquad \Gamma_{1\to\downarrow} \propto \sin^2\frac{\theta}{2},$$
$$\Gamma_{\downarrow\to1} \propto \cos^2\frac{\theta}{2}, \qquad\qquad \Gamma_{1\to\uparrow} \propto \cos^2\frac{\theta}{2}.$$

Assuming that the population of the intermediate pumping state $|1\rangle$ is constant, $\dot{\rho}_{1,1} = 0$, we obtain effective pumping rates between the states $|\downarrow\rangle$ and $|\uparrow\rangle$,

$$\Gamma_\uparrow = \frac{\Gamma_{\downarrow\to1}\Gamma_{1\to\uparrow}}{\Gamma_{\downarrow\to1} + \Gamma_{1\to\uparrow}} \propto \cos^4\frac{\theta}{2},$$

$$\Gamma_\downarrow = \frac{\Gamma_{\uparrow\to1}\Gamma_{1\to\downarrow}}{\Gamma_{\uparrow\to1} + \Gamma_{1\to\downarrow}} \propto \sin^4\frac{\theta}{2}.$$

Therefore, a quasistatic change of the mixing angle θ translates into a fluctuation of D_0 and Γ_1 according to

$$D_0 \propto \frac{2\cos\theta}{1 + \cos^2\theta},$$

$$\Gamma_1 \propto \frac{1}{2}\left(1 + \cos^2\theta\right).$$

Typically, the mixing angle fulfills $\theta \lesssim \pi/2$, hence D_0 fluctuates proportional to $\theta - \pi/2$ whereas Γ_1 is approximately constant. Therefore, we focus in this section on disorder only in the pumping strength D_0.

Analysis of disorder in D_0

Having performed the integration over the pumping strength D_0 in Eq. (4.8) we obtain the following fixed point equation:

$$\langle n\rangle = N_{\text{th}} + M\beta \frac{\overline{D}_0\left(\langle n\rangle + \frac{1}{2}\right) + \frac{1}{2}}{\Gamma_\kappa^2 + \Delta^2 + \alpha(\langle n\rangle + \frac{1}{2})}.$$

Its solution is given by

$$\overline{\langle n\rangle}_M = X + \sqrt{X^2 + N_{\text{th}}\tilde{n}_0 + \frac{N_{\text{th}}}{2} + M\frac{\Gamma_1}{4\kappa}(\overline{D}_0 + 1)}, \qquad (4.13)$$

$$X = -\frac{1}{4} + \frac{N_{\text{th}}}{2} + M\frac{\overline{D}_0\Gamma_1}{4\kappa} - \frac{\tilde{n}_0}{2}.$$

An obvious difference between the case of disorder in the pumping strength and the previously analyzed cases of disorder in the detuning or the coupling strength is that the averaged fixed point equation depends only on the mean pumping strength $\overline{D}_0$. There is no dependence of the disorder standard deviation σ_g and any probability distribution p with mean $\overline{D}_0$ yields the same averaged fixed point equation irrespective of its shape.

Again we compare three different scenarios: First, a mean pumping strength $\overline{D}_0 = 0.6$ far above the lasing threshold at zero detuning is examined (left subplot of Fig. 4.5). Second, we choose a nonzero detuning $\Delta = 0.015\,\omega$, but we keep the mean pumping strength $\overline{D}_0 = 0.6$ fixed (central subplot). Third, we examine a mean pumping strength $\overline{D}_0 = 0.15$ close to the lasing threshold at zero detuning (right subplot of Fig. 4.5). The pumping strength D_0 must take values in the range $[-1, 1]$. Therefore, Eq. (4.9) restricts the allowed values for the disorder standard deviation to $\sigma_{D_0} \lesssim 0.17\,\omega$ for a Gaussian distribution in the first and the second scenario, and to $\sigma_{D_0} \lesssim 0.36\,\omega$ in the third scenario.

For the first scenario, $\overline{D}_0 = 0.6$ and $\Delta = 0\,\omega$, we find that the mean photon-number expectation value $\overline{\langle n\rangle}_M$ is well approximated by an average over the individual lasing resonance curves $\langle n\rangle_1(D_0)$. For typical lasing parameters above the threshold Eq. (2.14) and the following relations hold:

$$\Gamma_1 D_0 \gg \kappa, \qquad\qquad\qquad (4.14\text{a})$$

$$M\frac{D_0\Gamma_1}{2\kappa} \gg N_{\text{th}}. \qquad\qquad\qquad (4.14\text{b})$$
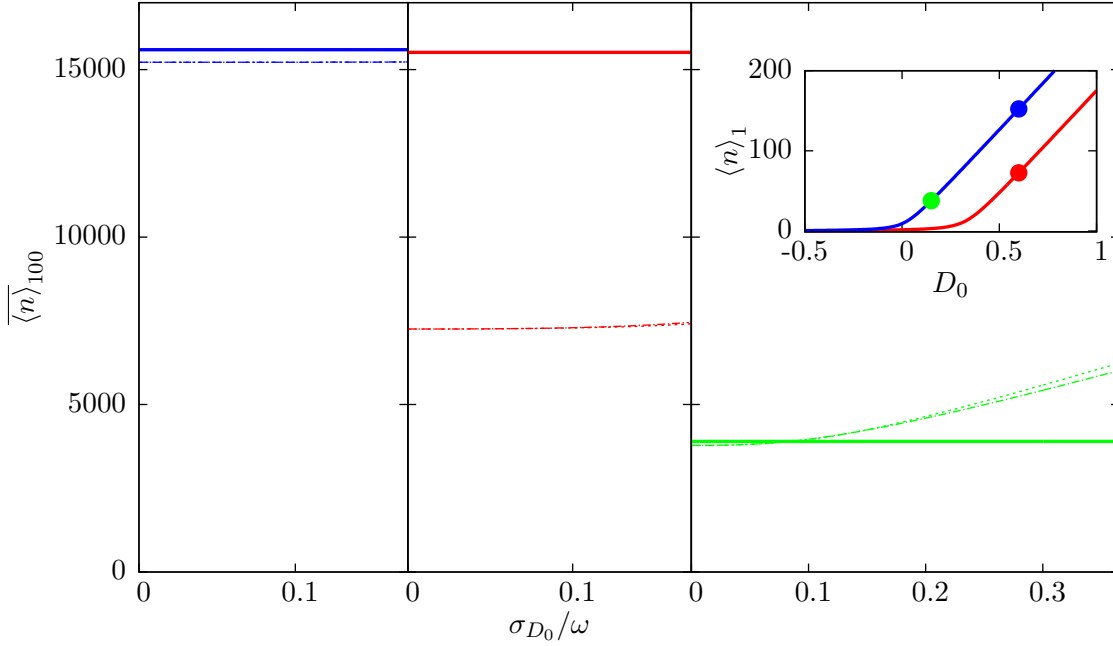
Figure 4.5.: Photon-number expectation value $\overline{\langle n \rangle}_{100}(\sigma_{D_0})$ for a lasing setup with $M = 100$ atoms and disorder in the pumping strength D_0. The results for $\overline{\langle n \rangle}_{100}$ (thick lines) are identical for a Gaussian and a box distribution. **Inset**: Single-atom lasing curves $\langle n \rangle_1 (D_0)$. The thin dash-dotted and dotted lines in the main plot represent an average over the single-atom lasing contributions for a Gaussian and a box distribution, respectively. Both curves coincide in the left and the central subplot. Plot parameters are $g = 0.001 \, \omega$, $\Gamma_1 = 0.0052 \, \omega$, $\Gamma_\varphi^* = 0.001 \, \omega$, $\kappa = 1 \times 10^{-5} \, \omega$, and $N_{\text{th}} = 0$. Blue curves $\Delta = 0 \, \omega$, $\overline{D}_0 = 0.6$. Red curves $\Delta = 0.015 \, \omega$, $\overline{D}_0 = 0.6$. Green curves $\Delta = 0 \, \omega$, $\overline{D}_0 = 0.15$. These values are indicated in the inset by colored circles.

Then, for zero detuning the mean photon number $\overline{\langle n \rangle}_M$ reduces to

$$\overline{\langle n \rangle}_M \approx N_{\text{th}} + M \frac{\Gamma_1 \overline{D}_0}{2\kappa} - \tilde{n}_0(0) \, .$$

Analogously, the same linear dependence on D_0 is obtained for the single-atom lasing curve (4.5),

$$\langle n \rangle_1 \approx N_{\text{th}} + \frac{\Gamma_1 D_0}{2\kappa} - \tilde{n}_0(0) \, ,$$

with a photon saturation number $\tilde{n}_0(0)$ of the order of unity. Therefore, for atoms on resonance and a sufficiently narrow disorder distribution, such that all values of D_0 are large enough that the assumption (4.14a) holds, the mean photon-number expectation value $\overline{\langle n \rangle}_M$ is expected to be equivalent to the average over the bare single-atom lasing curves $\langle n \rangle_1$,

$$\overline{\langle n \rangle}_M^{\text{bare}} = M \int \mathrm{d}D_0 \; p(D_0) \; \langle n \rangle_1(D_0) \, .$$

The thick blue curve in the left subplot of Fig. 4.5 represents $\overline{\langle n \rangle}_M$ and the coinciding thin dashed and dash-dotted curves represent $\overline{\langle n \rangle}_M^{\text{bare}}$ for a Gaussian and a box distribution, respectively. The average over single-atom lasing curves $\overline{\langle n \rangle}_M^{\text{bare}}$ describes the mean photon-number expectation value $\overline{\langle n \rangle}_M$ of the multi-atom lasing setup quite well, but we still

observe a small enhancement of the lasing activity in the multi-atom setup for the chosen parameters.

However, for a nonzero detuning $\overline{\langle n \rangle}_M^{\text{bare}}$ deviates significantly from the photon-number expectation value $\overline{\langle n \rangle}_M$ of the multi-atom lasing setup (central subplot in Fig. 4.5). The behavior of $\overline{\langle n \rangle}_M^{\text{bare}}$ can be understood as follows: The bare single-atom lasing curves $\langle n \rangle_1 (D_0)$ in the inset show a crossover from a very low photon number at pumping strengths below the lasing threshold to a nonzero photon number that depends linearly on the pumping strength above the lasing threshold. This threshold pumping strength increases for nonzero detuning, but the slope of the lasing curve above the threshold is still the same, i.e., the single-atom lasing curve $\langle n \rangle_1$ is effectively shifted along the D_0 axis for a nonzero detuning. Therefore, the single-atom photon-number expectation value $\langle n \rangle_1$ at a fixed pumping strength $\overline{D}_0$ decreases for a nonzero detuning. Surprisingly, comparing the thick red and blue curves in Fig. 4.5 we find that the actual mean photon-number expectation value $\overline{\langle n \rangle}_M$ is quite independent of the detuning. This implies that the effective lasing-threshold pumping strength for detuned atoms in a multi-atom lasing setup is significantly lowered and is actually close to zero.

Also for the third scenario, resonant atoms at a mean pumping strength $\overline{D}_0$ close to the lasing transition, $\overline{\langle n \rangle}_M$ and $\overline{\langle n \rangle}_M^{\text{bare}}$ differ significantly (right subplot of Fig. 4.5). For a small disorder standard deviation σ_{D_0} the average $\overline{\langle n \rangle}_M^{\text{bare}}$ is almost constant, which is the expected behavior if an average over the linear part $\langle n \rangle_1 \propto D_0$ of the single-atom lasing curve is taken: The increase of the photon number for atoms at a pumping strength $D_0 > \overline{D}_0$ is compensated by a decrease of the photon number for atoms at $D_0 < \overline{D}_0$. However, for $\sigma_{D_0} \gtrsim 0.1\,\omega$ the average $\overline{\langle n \rangle}_M^{\text{bare}}$ starts to increase with σ_{D_0}. In this regime the probability distribution is sufficiently broad such that some atoms have a pumping strength $D_0 \lesssim 0$ and, therefore, do not contribute to the lasing process any more. Hence, they cannot compensate for the increase of the photon number for atoms at $D_0 > \overline{D}_0$ and the overall average photon number $\overline{\langle n \rangle}_M^{\text{bare}}$ increases. However, the actual multi-atom photon-number expectation value $\overline{\langle n \rangle}_M$ is found to be independent of the disorder standard deviation σ_{D_0}. This implies that the single-atom lasing curve $\langle n \rangle_1$ is modified in a multi-atom lasing setup and has a linear dependence on the pumping strength D_0, even for a pumping strength close to zero.

In conclusion, for disorder in the pumping strength the mean photon-number expectation value $\overline{\langle n \rangle}_M$ is only a function of $\overline{D}_0$ and, in particular, independent of the disorder standard deviation σ_{D_0}. For resonant atoms above the pumping threshold, $\Delta = 0$ and $\overline{D}_0 > 0$, the observed collective behavior is explained quite well by an average over single-atom lasing curves $\langle n \rangle_1$. However, the observed behavior of $\overline{\langle n \rangle}_M$ for non-resonant atoms or a mean pumping strength close to the single-atom lasing-threshold pumping strength implies that the single-atom lasing curve $\langle n \rangle_1$ is modified in a multi-atom lasing setup as follows:

1. The lasing-threshold pumping strength of detuned atoms in a multi-atom lasing setup is decreased compared to its value in a single-atom lasing setup, and

2. the effective lasing curve of atoms in a multi-atom lasing setup shows a linear dependence on the pumping strength D_0, even for a pumping strength close to zero.

An explanation for these observations is given in Sec. 4.3.2.

4.3. Collective effects caused by stimulated emission

The results of the previous section show that a multi-atom lasing setup is rather robust against disorder in the atomic detuning, the coupling strength, and the pumping strength.

The observed dependence of the mean photon-number expectation value $\overline{\langle n \rangle}_M$ on the disorder standard deviation suggests, that

1. the range of tolerable atomic detuning increases with the system size M,

2. the minimal coupling strength to the resonator required for lasing decreases with the system size M, and

3. the lasing-threshold pumping strength in a multi-atom lasing setup is close to zero, even for detuned atoms, and the single-atom lasing curve has a linear dependence on the pumping strength D_0, even for a pumping strength close to zero.

In this section this collective effect is examined in more detail. First, we discuss ordered multi-atom systems. There we already observe a widening of the range of parameters that allow for lasing in multi-atom systems. In a second step, Eq. (4.3) is reformulated as a set of M coupled equations, each describing the lasing activity of a single atom, which have to be solved self-consistently. Using this approach we discuss disordered setups and show that the observed collective effect is caused by enhanced stimulated emission.

4.3.1. Widening of the range of lasing parameters in ordered systems

Before dealing with disorder in the atomic parameters, the properties of ordered systems are studied. For ordered systems Eq. (4.3) can be solved analytically. Having replaced $\Delta_j = \Delta$, $g_j = g$, $\Gamma_{1,j} = \Gamma_1$, $\Gamma_{\kappa,j} = \Gamma_\kappa$, $D_{0,j} = D_0$ for all atoms $j \in \{1, \dots, M\}$, an evaluation of the the sum yields

$$\langle n \rangle = N_{\text{th}} + M\beta \frac{D_0 \left(\langle n \rangle + \frac{1}{2} \right) + \frac{1}{2}}{\Gamma_\kappa^2 + \Delta^2 + \alpha \left(\langle n \rangle + \frac{1}{2} \right)} .$$

The stationary photon-number expectation value of an ordered system is

$$\langle n \rangle_M^0 = X + \sqrt{X^2 + N_{\text{th}} \tilde{n}_0 + \frac{N_{\text{th}}}{2} + M \frac{\Gamma_1}{4\kappa}(D_0 + 1)}, \qquad (4.15)$$

$$X = -\frac{1}{4} + \frac{N_{\text{th}}}{2} + M \frac{D_0 \Gamma_1}{4\kappa} - \frac{\tilde{n}_0}{2},$$

where the superscript 0 denotes the ordered system. For a single atom, $M = 1$, $\langle n \rangle_M^0$ is identical to the single-atom lasing curve $\langle n \rangle_1$ given by Eq. (4.5). The following scaling relation for the photon-number expectation value per atom, $\langle n \rangle_M^0 / M$, holds [32]:

$$\frac{1}{M} \langle n \rangle_M^0 \left(\frac{g}{\sqrt{M}}, \Delta, M N_{\text{th}} \right) \approx \langle n \rangle_1^0 (g, \Delta, N_{\text{th}}) .$$

In Fig. 4.6, the consequences of this scaling relation are illustrated:

- Provided that the coupling strength in the multi-atom system is rescaled by a factor of $\sqrt{M}^{-1}$, the qualitative dependence of $\langle n \rangle_M^0 / M$ on the detuning Δ or the coupling strength g is the same for different numbers of atoms, M, and the total photon number $\langle n \rangle_M^0$ grows linearly with the number of atoms.

- For $M \to \infty$ the smeared-out crossover from a non-lasing state to a lasing state is replaced by a sharp, kink-like lasing transition. The position of this kink coincides with the lasing threshold obtained out of the semiclassical theory. Thus, semiclassical and semiquantum theory yield identical results in the limit $M \to \infty$.

(a)   **(b)**
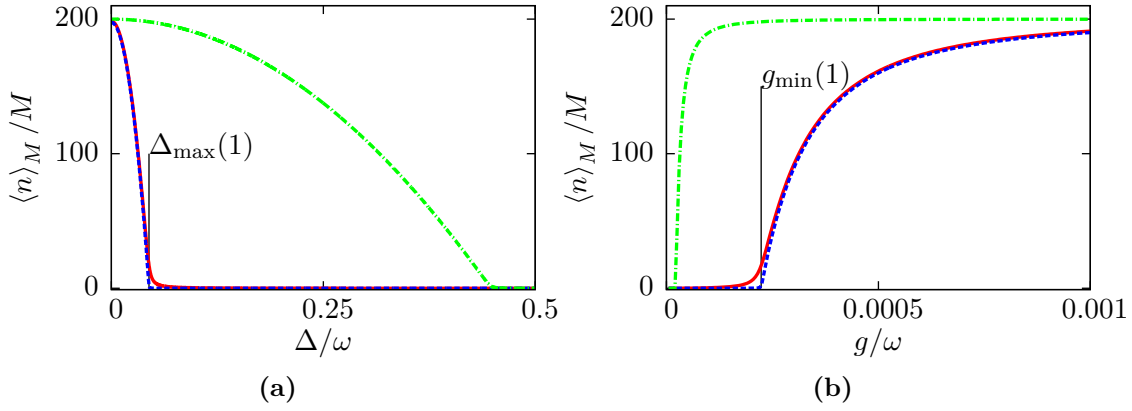
Figure 4.6.: Properties of the photon-number expectation value per atom, $\langle n \rangle_M^0 (\Delta, g)/M$, in an ordered M-atom lasing setup. **(a)**: Plots as a function of the atomic detuning Δ for a coupling strength $g = 0.002\,\omega$. **(b)**: Plots as a function of the coupling strength g for atoms on resonance, $\Delta = 0\,\omega$. Solid red curves represent $\langle n \rangle_1^0 (g, \Delta)$, dashed blue curves $\langle n \rangle_M^0 (g/\sqrt{M}, \Delta)/M$, and dash-dotted green curves $\langle n \rangle_M^0 (g, \Delta)/M$. For a fixed coupling strength g an increase of the system size M increases the maximum tolerable detuning. For a fixed detuning it lowers the minimal coupling strength required for lasing. In the limit $M \to \infty$ the semiquantum theory predicts a sharp, kink-like lasing transition that coincides with the one predicted by the semiclassical theory. Plot parameters are $\Gamma_\uparrow = 0.006\,\omega$, $\Gamma_\downarrow = 0.002\,\omega$, $\Gamma_\varphi^* = 0.001\,\omega$, $\kappa = 1 \times 10^{-5}\,\omega$, $N_{\text{th}} = 0$, and $M = 100$.

- If the coupling strength is not rescaled by a factor of $\sqrt{M}^{-1}$, the width of $\langle n \rangle_M /M$ as a function of the detuning increases and the minimum coupling strength decreases with the number of atoms. From Eqs. (2.15) and (2.16) we obtain the following scaling behavior:

$$\Delta_{\text{max}} \propto \sqrt{M}\,,$$
$$g_{\text{min}} \propto \frac{1}{\sqrt{M}}\,.$$

These relations imply that for a fixed coupling strength a many-atom lasing system tolerates a larger detuning than a single-atom laser, while still being in a lasing state. Furthermore, the coupling strength of the individual atoms to the resonator can be lowered compared to that of a single-atom laser, while the system is still in a lasing state. From Eq. (2.17) we read off that the required minimal pumping strength is also lowered in a multi-atom lasing setup,

$$D_{0,\text{min}} \propto \frac{1}{M}\,.$$

In conclusion, for ordered multi-atom systems the range of atomic parameters for which the system is in a lasing state is actually widened compared to the corresponding range of parameters for a single-atom laser. There is a collective broadening of the tolerable range of atomic detuning and a lowering of the minimal coupling and pumping strength, consistent with the observations made in Sec. 4.2.

4.3.2. Self-consistent superposition of single-atomic resonance curves

In order to discuss these collective effects for disordered setups, Eq. (4.3) is reformulated as a set of M equations for the single-atomic photon contribution $\langle n_j \rangle$ to the overall photon-number expectation value $\langle n \rangle_M$. The set of equations has to be solved self-consistently.

This reformulation of the problem allows to demonstrate the widening of the range of lasing parameters also for disordered systems and reveals that it is caused by stimulated emission.

The total photon number $\langle n \rangle$ is split into contributions of the individual atoms, $\langle n_j \rangle$, by rewriting

$$\langle n \rangle = \sum_{j=1}^{M} \langle n_j \rangle = \langle n_i \rangle + \left\langle n_{\text{add}}^i \right\rangle , \tag{4.16a}$$

$$\left\langle n_{\text{add}}^i \right\rangle = \sum_{\substack{j \neq i \\ j=1}}^{M} \langle n_j \rangle , \tag{4.16b}$$

where $i \in \{1, \dots, M\}$ is the index of an arbitrarily chosen atom. The quantity $\left\langle n_{\text{add}}^i \right\rangle$ is the number of photons that are emitted into the resonator by all atoms except of atom i, including the corresponding fraction of the thermal photon number. It forms a background of additional photons in the resonator that does not originate from the lasing activity of atom i. By inserting Eq. (4.16a) into the stationary limit of Eq. (4.1a) the photon-number expectation value (4.1a) is separated into M equations describing the individual atomic contributions $\langle n_i \rangle$ to the overall photon number. Using Eqs. (4.1b) and (4.1c) we obtain

$$\langle n_i \rangle = \frac{N_{\text{th}}}{M} + \beta_i \frac{D_{0,i} \left(\langle n_i \rangle + \langle n_{\text{add}}^i \rangle + \frac{1}{2} \right) + \frac{1}{2}}{\Gamma_{\kappa,i}^2 + \Delta_i^2 + \alpha_i \left(\langle n_i \rangle + \langle n_{\text{add}}^i \rangle + \frac{1}{2} \right)} . \tag{4.17}$$

For a single-atom laser, i.e., $i = 1$, $M = 1$, $\langle n_1 \rangle = \langle n \rangle$, and $\langle n_{\text{add}}^1 \rangle = 0$, this equation reduces to the single-atom case of Eq. (4.3). A summation over all M atoms yields the general fixed point equation (4.3).

The fixed point equation (4.17) for the individual atomic contributions $\langle n_i \rangle$ is solved by

$$\langle n_i \rangle = \tilde{X} + \sqrt{\tilde{X}^2 + \frac{N_{\text{th}}}{M} \left(\tilde{n}_{0,i} + \langle n_{\text{add}}^i \rangle + \frac{1}{2} \right) + \frac{\Gamma_{1,i}}{4\kappa} \left(D_{0,i} \left(2 \langle n_{\text{add}}^i \rangle + 1 \right) + 1 \right)}, \tag{4.18}$$

$$\tilde{X} = -\frac{1}{4} - \frac{\langle n_{\text{add}}^i \rangle}{2} + \frac{N_{\text{th}}}{2M} + \frac{\Gamma_{1,i} D_{0,i}}{4\kappa} - \frac{\tilde{n}_0}{2} .$$

The M equations for $\langle n_i \rangle$, $i \in \{1, \dots, M\}$, and Eq. (4.16) form a set of coupled equations which have to be solved self-consistently. This is done numerically using the following iterative algorithm:

1. Initially, the resonator is assumed to have zero photon number, i.e., $\langle n \rangle = 0$ and $\langle n_{\text{add}}^i \rangle = 0$ for all atoms $i \in \{1, \dots, M\}$.

2. The contribution of each atom to the photon number in the resonator, $\langle n_i \rangle$, is calculated.

3. New values for $\langle n \rangle$ and $\langle n_{\text{add}}^i \rangle$ are calculated using Eq. (4.16).

4. The procedure is continued starting from step 2 until $\langle n \rangle$ changes between two iterations less than a previously chosen threshold.

The calculations of the mean photon-number expectation value $\overline{\langle n \rangle}_M$ performed in the previous sections effectively solved this self-consistent set of coupled equations. However, this reformulation of the problem allows to study the broadening and enhancement effects observed in Sec. 4.2 also for disordered systems.

On the right-hand side of Eq. (4.18) the photon background $\langle n_{\text{add}}^i \rangle$ appears always together with $\langle n_i \rangle$, which is the term accounting for the stimulated emission of atom i. Therefore,
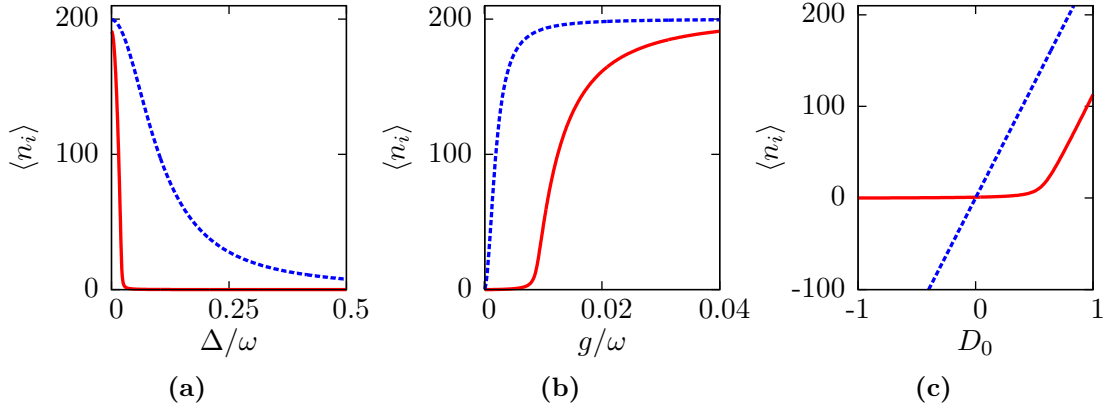
Figure 4.7.: Modification of the single-atom lasing curve $\langle n_i \rangle$ in the presence of additional photons in the resonator. **(a)**: $\langle n_i \rangle (\Delta, g, D_0)$ as a function of the atomic detuning Δ for a fixed coupling strength $g = 0.001\,\omega$ and $D_0 = 0.5$. **(b)**: $\langle n_i \rangle (\Delta, g, D_0)$ as a function of the coupling strength g for a fixed detuning $\Delta = 0.2\,\omega$ and $D_0 = 0.5$. **(c)**: $\langle n_i \rangle (\Delta, g, D_0)$ as a function of the pumping strength D_0 for a fixed detuning $\Delta = 0.02\,\omega$ and a fixed coupling strength $g = 0.001\,\omega$. Solid red curves represent the bare lasing curve without additional photons in the resonator, dashed blue curves represent the modified lasing curve in the presence of $\langle n_{add}^i \rangle = 4000$ additional photons in the resonator. The presence of additional photons broadens the resonance curve as a function of the detuning and decreases the minimal threshold coupling strength required for lasing. The lasing threshold pumping strength vanishes such that $\langle n_i \rangle (D_0)$ is proportional to D_0 for all pumping rates. Negative pumping decreases the number of photons in the resonator. Plot parameters are $\Gamma_\uparrow = 0.006\,\omega$, $\Gamma_\downarrow = 0.002\,\omega$, $\Gamma_\varphi^* = 0.001\,\omega$, and $\kappa = 1 \times 10^{-5}\,\omega$. Subfigure (c) has $\Gamma_1 = 0.0052\,\omega$.

the presence of additional photons in the resonator modifies the stimulated emission lasing activity of the atom. The effect can be illustrated by simply assuming the existence of additional photons, wherever they actually come from. In Fig. 4.7 the individual atomic contribution $\langle n_i \rangle$ is plotted for $\langle n_{add}^i \rangle = 0$ and $\langle n_{add}^i \rangle = 4000$ additional photons, respectively.

In Fig. 4.7a the atomic lasing contribution $\langle n_i \rangle$ is plotted as a function of the detuning Δ. The presence of additional photons broadens the curve, i.e., the range of tolerable values of the atomic detuning is significantly widened, as deducted from the plot of $\overline{\langle n \rangle}_M(\sigma_\Delta)$ in Fig. 4.2. The presence of additional photons in the resonator increases the lasing activity of detuned atoms and effectively "drags" them into resonance. Furthermore, an enhancement of the photon-number expectation value $\langle n_i \rangle$ at zero detuning is observed, which is also consistent with the observations made in Fig. 4.2.

Similarly, $\langle n_i \rangle (g)$ is plotted as a function of the coupling strength g in Fig. 4.7b. A lowering of the minimal coupling strength $g_{min}(M)$, rigorously derived for ordered setups, is also shown qualitatively by $\langle n_i \rangle (g)$ in the presence of additional photons. Hence, also in disordered setups a collective lowering of the lasing threshold coupling strength takes place, consistent with the observations made in Fig. 4.3. Simultaneously, for large coupling strengths $g \gg g_{min}(1)$ the presence of additional photons enhances $\langle n_i \rangle (g)$ up to a maximum photon number per atom $\langle n \rangle_M^{max}/M$, irrespective of the actual detuning of the atom. The maximum photon number $\langle n \rangle_M^{max}$ is defined by Eq. (4.4) and depends on the pumping and decay rates of the system. This enhancement is the reason for the remarkably weak dependence of $\overline{\langle n \rangle}_{100}(\sigma_g)$ on the detuning Δ observed in Fig. 4.3b.

In Fig. 4.3a, we observed that $\overline{\langle n \rangle}_M(\sigma_g)$ increases or decreases as a function of σ_g, depending on the detuning Δ. This behavior is connected to the local curvature of the modified atomic

resonance curves $\langle n_i \rangle (g)$ at the mean coupling strength $\bar{g}$. An expansion of $\langle n_i \rangle$ around $\bar{g}$,

$$\langle n_i \rangle (g) = a + b(g - \bar{g}) + c(g - \bar{g})^2 + \mathcal{O}\left((g - \bar{g})^3\right),$$

yields

$$\int_{-\infty}^{\infty} dg\, p(g) \langle n_i \rangle (g) = a + c\sigma_g^2.$$

If $\langle n_i \rangle (g)$ is dominantly a linear function of the coupling strength at $\bar{g}$, i.e., $c \approx 0$, the mean photon-number expectation value $\overline{\langle n \rangle}_M(\sigma_g)$ is a constant. Likewise, if the curvature of $\langle n_i \rangle (g)$ at $\bar{g}$ cannot be neglected, i.e., $|c| \gtrsim |b|$, its sign determines the behavior of $\overline{\langle n \rangle}_M(\sigma_g)$ with increasing σ_g.

Finally, Fig. 4.7c illustrates the changes of the single-atom lasing contribution $\langle n_i \rangle$ as a function of the pumping strength D_0 in the presence of additional photons. The plot of $\langle n_i \rangle (D_0)$ shows the expected linear dependence on the pumping strength D_0, even for $D_0 \lesssim 0$, which was concluded from the observations made in Fig. 4.5. As a second observation we note that the pumping threshold is zero even though the atom has a nonzero detuning. The lasing crossover, where $\langle n_i \rangle$ changes smoothly from a close to zero photon number to a linear dependence on D_0, does not appear any more. Instead, for a negative pumping strength the number of photons in the resonator is decreased by the inverse lasing activity of the atom. The dependence on the pumping strength is linear for negative pumping if the absolute value of $\langle n_i \rangle$ is much smaller than the number of externally created additional photons, $|\langle n_i \rangle| \ll \langle n_{\mathrm{add}}^i \rangle$. The linear dependence on D_0 and the absence of a threshold coupling strength is consistent with the observations made in Fig. 4.5.

Application of the method to ordered systems

For disordered setups we showed that atoms above the lasing threshold, for instance, close to resonance, "drag" others which appeared to be below the lasing threshold also into a lasing state. Finally, a self-organized stationary state is established. But in Sec. 4.3.1 a widening of the range of parameters allowing for lasing was observed also in the case of ordered systems. In particular, there is a nonzero multi-atom photon-number expectation value in ordered systems, $\langle n \rangle_M^0 \neq 0$, even when all atoms have a detuning $\Delta > \Delta_{\max}(1)$, which would be completely off-resonant in a single-atom setup. The reformulation of the fixed point equation (4.3) as a set of self-consistently added single-atomic lasing contributions $\langle n_i \rangle$ reproduces this nonzero value of $\langle n \rangle_M^0$ as well. In order to understand this we consider M identical atoms which would all be off-resonant in the single-atom setup, $\Delta > \Delta_{\max}(1)$. As seen in Fig. 4.1 the semiquantum model does not exhibit a sharp transition to the lasing state. Therefore, each of the atoms produces a small but non-vanishing contribution $\langle n_i \rangle$ to the total photon number $\langle n \rangle_M^0$ even at a detuning $\Delta > \Delta_{\max}(1)$. This possibly very small contribution is then enhanced by the presence of all other ones, which is sufficient to drive the system into the lasing state.

4.4. Fluctuations of the photon-number expectation value for finite-size systems

In the near future, experimental realizations of lasers using quantum metamaterials as optically active medium will probably be constructed out of a not too large number of atoms, e.g., $M \lesssim 100$. Therefore, one should expect significant sample-specific deviations from the average photon number $\overline{\langle n \rangle}_M$ calculated in the previous sections. Consequently, statistical fluctuations of $\langle n \rangle_M$ around its mean value $\overline{\langle n \rangle}_M$ are studied in this section.

In order to study fluctuations of the photon-number expectation value $\langle n \rangle_M$, an ensemble of N_{ens} lasing setups is chosen with randomly distributed lasing parameters according to a
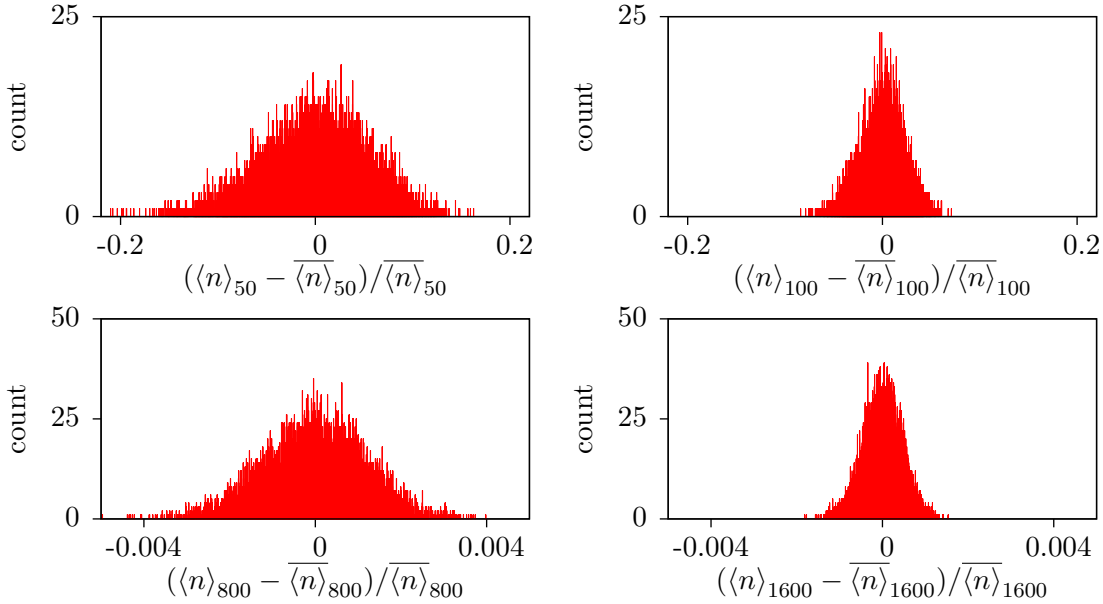
Figure 4.8.: Fluctuations of the photon-number expectation value $\langle n \rangle_M$ around $\overline{\langle n \rangle}_M$ for disorder in the detuning Δ due to a non-perfect sampling of a Gaussian disorder distribution with mean $\overline{\Delta} = 0$ and standard deviation $\sigma_\Delta = 0.2\,\omega$. Histograms are created for $N_{\text{ens}} = 10000$ setups, randomly chosen according to a Gaussian disorder distribution, for system sizes of $M = 50, 100, 800,$ and 1600 atoms, respectively. The mean photon number is given by $\overline{\langle n \rangle}_{50} = 7479$, $\overline{\langle n \rangle}_{100} = 16976$, $\overline{\langle n \rangle}_{800} = 156184$, and $\overline{\langle n \rangle}_{1600} = 316100$ photons, respectively. Plot parameters are $\overline{\Delta} = 0\,\omega$, $g = 0.002\,\omega$, $\Gamma_\uparrow = 0.006\,\omega$, $\Gamma_\downarrow = 0.002\,\omega$, $\Gamma_\varphi^* = 0.001\,\omega$, $\kappa = 1 \times 10^{-5}\,\omega$, and $N_{\text{th}} = 0$.

given probability distribution p. For each of these setups Eq. (4.3) is solved numerically for the photon number $\langle n \rangle_M$. This approach can be used to model two types of disorder:

1. Static disorder, e.g., sample-to-sample specific fluctuations of the lasing parameters caused by the production process, and

2. quasistatic disorder on long timescales of the order of hours which is, for instance, caused by two-level fluctuators, charge, or flux noise in superconducting qubits.

Fig. 4.8 shows the results for Gaussian disorder in the detuning Δ with a standard deviation $\sigma_\Delta = 0.2\,\omega$. With increasing system size M the sampling of the ideal disorder distribution p by the setup becomes better, which decreases the error made by rewriting the sum as an integral in Eq. (4.8). In the plots in Fig. 4.8 this manifests as a decrease of the fluctuations around $\overline{\langle n \rangle}_M$ with increasing system size M. Their standard deviation is given by 386, 352, 181, and 136 photons for $M = 50, 100, 800,$ and 1600 atoms, respectively. However, even for $M = 1600$ atoms fluctuations of the order of one percent of $\overline{\langle n \rangle}_M$ are expected.

Similar effects arise for disorder in the coupling strength g. The corresponding results are shown in Fig. 4.9. When the mean coupling strength $\overline{g}$ is chosen close to the lasing transition of a single-atom setup, the histogram of $\langle n \rangle_M$ shows a main peak around $\overline{\langle n \rangle}_M$ and a long tail consisting of a few ensembles with smaller photon number. The main peak shows the expected narrowing with increasing system size M: If all histogram bins with less than 10 counts are cut away, the standard deviation of the main peak is given by 0.25, 0.19, 0.17, and 0.15 photons for $M = 50, 100, 800,$ and 1600 atoms, respectively. The long tail is due to the fact that some atoms have such a weak coupling strength that they either cannot participate in the lasing process at all or participate only with a reduced photon number $\langle n_i \rangle < \langle n \rangle_1^{\text{max}}$. Figure 4.7b shows that such a situation is realized for a coupling strength close to zero, even in the presence of additional photons in the resonator.

(a) Mean coupling strength $\overline{g} = 0.002\,\omega$ close to the single-atom lasing threshold

(b) Mean coupling strength $\overline{g} = 0.005\,\omega$ above the single-atom lasing threshold
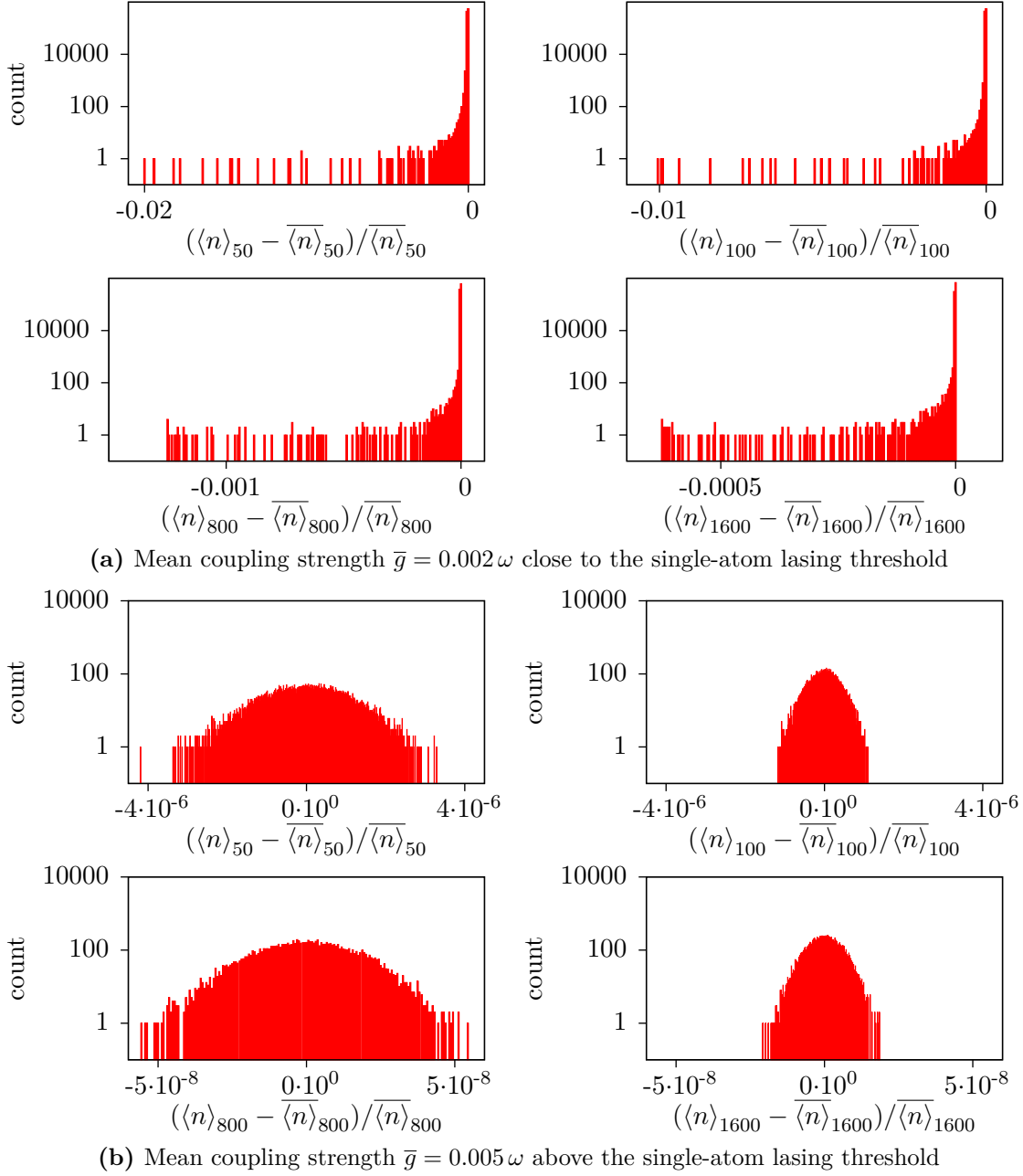
Figure 4.9.: Fluctuations of the photon-number expectation value $\langle n \rangle_M$ around $\overline{\langle n \rangle}_M$ for disorder in the coupling strength g due to a non-perfect sampling of a Gaussian disorder distribution with mean $\overline{g}$ and standard deviation $\sigma_g = 0.0004\,\omega$ and $M = 50, 100, 800$, and 1600 atoms, respectively. **(a)**: The mean coupling strength $\overline{g} = 0.002\,\omega$ is chosen close to the lasing transition of a single atom on resonance. The distribution has a main peak at $\overline{\langle n \rangle}_M$ and a large tail of a small number of systems with $\langle n \rangle_M < \overline{\langle n \rangle}_M$, which is not completely smooth even for $N_{\mathrm{ens}} = 1000000$ randomly chosen setups. The main peak is situated at $\overline{\langle n \rangle}_{50} = 9998$, $\overline{\langle n \rangle}_{100} = 19998$, $\overline{\langle n \rangle}_{800} = 159998$, and $\overline{\langle n \rangle}_{1600} = 319998$ photons, respectively. **(b)**: The mean coupling strength $\overline{g} = 0.005\,\omega$ is chosen far above the lasing transition of a single atom on resonance. Data is obtained for $N_{\mathrm{ens}} = 10000$ randomly chosen setups. In this regime only the main peak is observed at $\overline{\langle n \rangle}_{50} = 10001$, $\overline{\langle n \rangle}_{100} = 200001$, $\overline{\langle n \rangle}_{800} = 160001$, and $\overline{\langle n \rangle}_{1600} = 320001$ photons, respectively. The plot parameters $\Gamma_\uparrow = 0.006\,\omega$, $\Gamma_\downarrow = 0.002\,\omega$, $\Gamma_\varphi^* = 0.001\,\omega$, $\kappa = 1 \times 10^{-5}\,\omega$, and $N_{\mathrm{th}} = 0$ are identical for both subfigures.

These events occur so rarely that a smooth distribution is not even found for a very large ensemble of $N_{\mathrm{ens}} = 10^6$ setups.

In a typical lasing experiment the mean coupling strength $\overline{g}$ is chosen far above the single-atom lasing threshold. In this regime only the main peak at $\overline{\langle n \rangle}_M$ is observed, as shown in Fig. 4.9b. For the chosen parameters the fluctuations in the photon number caused by disorder in the detuning dominate over the ones originating from disorder in the coupling strength.

In conclusion, lasing setups with a finite number M of atoms show quasistatic or static fluctuations of the photon-number expectation value $\langle n \rangle_M$ of the order of a percent of the mean photon number. Fluctuations decrease when the system size M is increased.

The long-term stability of current microwave generators depends not only on the source itself, but also on the power amplifier and temperature fluctuations in the laboratory. It is mainly influenced by fluctuations of the power amplifier bias point and the amplification of parasitic signals [39]. If these effects are taken into account, the laser discussed here may compete with current microwave sources for large system sizes M. For measurements on short timescales, e.g., when the laser is used to control qubit operations in a quantum computer, these long-term fluctuations do not matter. There, fluctuations on short timescales originating from the photon statistics of the laser are more relevant. The photon statistics cannot be derived within the semiquantum approximation. Instead, a direct solution of the master equation is needed, similar to the calculations in the following chapter.

5. Longitudinal couplings

5.1. Generalized lasing Hamiltonian

In the previous chapter the Tavis-Cummings Hamiltonian defined in Eq. (2.2) was considered as model of a multi-atom laser. It contains a dipole interaction between the atoms and the radiation field, $H_{\text{int}} \propto \sigma_x(a + a^\dagger)$, which takes the form $H_{\text{int}} \propto \sigma_+ a + \sigma_- a^\dagger$ under a rotating wave approximation. However, quantum metamaterials can be built out of artificial atoms that couple to the radiation field differently. As discussed in the introduction superconducting qubits exhibit not only a transversal σ_x coupling, but also a longitudinal σ_z coupling. For flux qubits, charge qubits, and quantum dot systems Eq. (2.2) needs to be generalized as follows:

$$H_M = \hbar\omega a^\dagger a + \sum_{j=1}^{M} \frac{1}{2}\epsilon_j \sigma_z^j + \sum_{j=1}^{M} \hbar g_j \left(\cos(\theta_j)\sigma_z^j + \sin(\theta_j)\sigma_x^j \right) \left(a^\dagger + a \right) . \qquad (5.1)$$

The photon creation and annihilation operators are denoted by $a^\dagger$ and a, respectively, and ω is the frequency of the (single-mode) resonator. By ϵ_j we denote the level splitting energy of the lasing transition of atom j, $j \in \{1, \ldots, M\}$, and g_j is the coupling strength of this atom to the resonator. The mixing angle $\theta_j \in [0, \pi/2]$ determines the relative strength of σ_x and σ_z interaction. The Pauli matrices acting on the two states of atom j are denoted by $\sigma_{x,y,z}^j$. Contrary to the Tavis-Cummings Hamiltonian a rotating wave approximation has not yet been applied.

In this chapter the photon statistics of a laser with both a longitudinal and a transversal coupling between atoms and radiation field is calculated. We solve the quantum master equation of the system in several stages: In Secs. 5.2 to 5.4 the photon statistics for a single-atom laser with both a longitudinal and a transversal coupling is derived. In Sec. 5.5 we discuss how to create photon-number squeezed light in a system described by the Hamiltonian (5.1). The assumptions made on the suppression of higher-order transitions and the pumping process are justified in Secs. 5.7 and 5.8. In Sec. 5.10 the results are generalized to a multi-atom lasing setup with M identical atoms. Finally, in Sec. 5.11 individual mixing angles θ_j are considered which arise, for instance, because of flux noise in a multi-atom lasing setup.

5.2. Single-atom lasing: Polaron transformation and quantum master equation

The generalized lasing Hamiltonian (5.1) for a single atom, $M = 1$, is given by

$$H_1 = \hbar\omega a^\dagger a + \frac{1}{2}\epsilon\sigma_z + \hbar g \left(\cos(\theta)\sigma_z + \sin(\theta)\sigma_x \right) \left(a^\dagger + a \right) . \qquad (5.2)$$

For the sake of a compact notation the following abbreviations are introduced:

$$x = x_0 \left(a^\dagger + a \right) = \hbar g \sin(\theta) \left(a^\dagger + a \right) , \tag{5.3a}$$

$$p = i p_0 \left(a^\dagger - a \right) = i \frac{g}{\omega} \cos(\theta) \left(a^\dagger - a \right) . \tag{5.3b}$$

H_1 is transformed into a Jaynes-Cummings-like Hamiltonian using the unitary polaron transformation

$$U = \exp \left[\frac{g}{\omega} \cos(\theta) \left(a - a^\dagger \right) \sigma_z \right] = \exp \left(i p \sigma_z \right) , \tag{5.4}$$

yielding (cf. Appendix B.1)

$$H = U^\dagger H_1 U = \hbar \omega a^\dagger a + \frac{1}{2} \epsilon \sigma_z + \hbar g \left(\sigma_+ \frac{e^{-ip} x e^{-ip}}{\hbar g} + \sigma_- \frac{e^{ip} x e^{ip}}{\hbar g} \right) - \frac{\hbar g^2}{\omega} \cos^2(\theta) . \tag{5.5}$$

The irrelevant constant shift of energy is neglected in the following. The polaron-transformed Hamiltonian has the structure of the Jaynes-Cummings Hamiltonian (2.1) with the photon creation and annihilation operators replaced by the dimensionless operators

$$A = \frac{1}{\hbar g} e^{-ip} x e^{-ip} \quad \text{and} \tag{5.6a}$$

$$A^\dagger = \frac{1}{\hbar g} e^{ip} x e^{ip} , \tag{5.6b}$$

respectively. The properties of these operators are discussed in Sec. 5.3.

As basis of the Hilbert space in the polaron frame the direct product of the photon states $|n\rangle$, $n \in \mathbb{N}_0$, and the states $|\uparrow\,/\,\downarrow\rangle$ of the two-level system is chosen,

$$|\uparrow\,/\,\downarrow, n\rangle \equiv |\uparrow\,/\,\downarrow\rangle \otimes |n\rangle .$$

The field operators and the Pauli matrices act on these states as usual,

$$\begin{aligned} a^\dagger a |n\rangle &= n |n\rangle , & \sigma_z |\uparrow\,/\,\downarrow\rangle &= \pm |\uparrow\,/\,\downarrow\rangle , \\ a^\dagger |n\rangle &= \sqrt{n+1} |n+1\rangle , & \sigma_x |\uparrow\,/\,\downarrow\rangle &= |\downarrow\,/\,\uparrow\rangle , \\ a |n\rangle &= \sqrt{n} |n-1\rangle . \end{aligned}$$

Because we have performed a polaron transformation, the state $|n\rangle$ does not represent a Fock state with n photons in the resonator as it was the case in the previous chapters. In the following a photon-number Fock state with n photons in the resonator cavity is denoted by $|n_\mathrm{c}\rangle$. The basis state $|n\rangle$ in the polaron frame is a superposition of different Fock states according to

$$|\sigma\rangle \otimes |n\rangle = U^\dagger |\sigma\rangle \otimes |n_\mathrm{c}\rangle .$$

This has implications on the calculation of the photon-number expectation value and is discussed in Sec. 5.5. The expansion of the state $|n\rangle$ in the polaron frame into Fock states $|m_\mathrm{c}\rangle$ in the cavity frame is derived in the Appendix B.2.

The quantum master equation describing the coherent lasing interaction as well as pumping, relaxation, and dephasing processes in the polaron frame is given by

$$\frac{\mathrm{d}}{\mathrm{d}t} \rho = -\frac{i}{\hbar} [H, \rho] + L_\mathrm{R} \rho + L_\mathrm{Q} \rho , \tag{5.7}$$

where L_{R} and L_{Q} are the Lindblad superoperators for the resonator and the two level system as introduced in Eqs. (2.8) and (2.9),

$$L_{\mathrm{R}}\rho = \frac{\kappa}{2}(N_{\mathrm{th}}+1)\left(2a\rho a^{\dagger} - a^{\dagger}a\rho - \rho a^{\dagger}a\right) + \frac{\kappa}{2}N_{\mathrm{th}}\left(2a^{\dagger}\rho a - aa^{\dagger}\rho - \rho aa^{\dagger}\right),$$

$$L_{\mathrm{Q}}\rho = \frac{\Gamma_{\downarrow}}{2}\left(2\sigma_{-}\rho\sigma_{+} - \rho\sigma_{+}\sigma_{-} - \sigma_{+}\sigma_{-}\rho\right) + \frac{\Gamma_{\uparrow}}{2}\left(2\sigma_{+}\rho\sigma_{-} - \rho\sigma_{-}\sigma_{+} - \sigma_{-}\sigma_{+}\rho\right)$$
$$+ \frac{\Gamma_{\varphi}^{*}}{2}\left(\sigma_{z}\rho\sigma_{z} - \rho\right).$$

In Sec. 5.8 we show that this common form of the Lindblad superoperators is not changed by the polaron transformation. The relaxation rate of the resonator is denoted by κ, $\Gamma_{\uparrow}$ and $\Gamma_{\downarrow}$ are effective pumping and relaxation rates of the atom, respectively, and Γ_{φ}^{*} is the effective pure dephasing rate of the atom. The master equation (5.7) is solved in Sec. 5.4.

5.3. Matrix elements of the generalized field operators

Before solving the quantum master equation (5.7) we analyze the properties and matrix elements of the generalized field operators $A = e^{-ip}xe^{-ip}/(\hbar g)$ and $A^{\dagger} = e^{ip}xe^{ip}/(\hbar g)$.

As a preparation we consider the matrix elements of the operator $e^{\pm 2ip}$, which are calculated in the momentum space. We introduce the dimensionless variables $\xi = x/\tilde{x}_0$ and $\eta = p/\tilde{p}_0$, where $\tilde{x}_0 = \sqrt{\hbar/(m\omega)}$ and $\tilde{p}_0 = \sqrt{\hbar m\omega}$ are constants with the dimension of a length and a momentum, respectively. The field operators are related to ξ and η as follows:

$$a = \frac{1}{\sqrt{2}}\left(\xi + i\eta\right),$$

$$a^{\dagger} = \frac{1}{\sqrt{2}}\left(\xi - i\eta\right).$$

Now, $e^{\pm 2ip}$ can be rewritten as follows:

$$e^{\pm 2ip} = \exp\left[\pm 2\frac{g}{\omega}\cos(\theta)\left(a - a^{\dagger}\right)\right] = e^{\beta\eta},$$

$$\beta = \pm 2\sqrt{2}i\frac{g}{\omega}\cos(\theta) = \pm 2\sqrt{2}ip_0.$$

The momentum-space representation of the state $|n\rangle$ is given by

$$\langle \boldsymbol{p}|n\rangle = \frac{N_0}{\sqrt{n!}}\left(\frac{-i}{\sqrt{2}}\right)^{n}H_n(\eta)e^{-\eta^2/2},$$

where $N_0^{-1} = \sqrt[4]{\pi}\sqrt{\tilde{p}_0}$ is a normalization constant and $H_n(\eta)$ are the Hermite polynomials

$$H_n(\eta) = (-1)^{n}e^{\eta^2}\frac{\mathrm{d}^{n}}{\mathrm{d}\eta^{n}}e^{-\eta^2}.$$

In the momentum space we obtain

$$\langle n|e^{\beta\eta}|n+m\rangle = \frac{p_0 N_0^2}{\sqrt{n!(n+m)!}}\frac{1}{2^{n}}\left(\frac{-i}{\sqrt{2}}\right)^{m}e^{\beta^2/4}\int_{-\infty}^{\infty}\mathrm{d}x\,e^{-x^2}H_n\left(x+\frac{\beta}{2}\right)H_{n+m}\left(x+\frac{\beta}{2}\right).$$

The integral is simplified by means of the properties of the Hermite polynomials,

$$H_n(x+y) = \sum_{k=0}^{n}\binom{n}{k}H_k(x)(2y)^{n-k},$$

$$\int_{-\infty}^{\infty}\mathrm{d}x\,e^{-x^2}H_k(x)H_l(x) = 2^{k}k!\sqrt{\pi}\delta_{k,l},$$

and by means of the definition of the generalized Laguerre polynomials,

$$L_n^m(x) = \sum_{j=0}^{n} (-1)^j \binom{n+m}{n-j} \frac{x^j}{j!} \, .$$

We obtain the following formula for the matrix elements of $e^{\pm 2ip}$:

$$T_{n,m}^{\pm} = \langle n| \, e^{\pm 2ip} \, |n+m\rangle \tag{5.8}$$

$$= \begin{cases} (\pm 1)^m e^{-2p_0^2} (2p_0)^m \sqrt{\frac{n!}{(n+m)!}} L_n^m(4p_0^2) & \text{for } n \in \mathbb{N}_0, \, m \in \mathbb{N}_0, \\ (\mp 1)^{|m|} e^{-2p_0^2} (2p_0)^{|m|} \sqrt{\frac{(n-|m|)!}{n!}} L_{n-|m|}^{|m|}(4p_0^2) & \text{for } n \in \mathbb{N}, \, m \in \mathbb{Z}, \, -n \le m < 0. \end{cases}$$

Now, we proceed to the operators of interest, A and $A^\dagger$. Their matrix elements can be expressed in terms of $T_{n,m}^{\pm}$,

$$\langle n| \, A \, |n+m\rangle = \langle n| \, \frac{1}{\hbar g} e^{-ip} x e^{-ip} \, |n+m\rangle$$
$$= \sin\theta \left(\sqrt{n+m+1} T_{n,m+1}^{-} + \sqrt{n+m} T_{n,m-1}^{-} \right) + 2\frac{g}{\omega} \sin\theta \cos\theta T_{n,m}^{-} \, ,$$
$$\langle n| \, A^\dagger \, |n+m\rangle = \langle n| \, \frac{1}{\hbar g} e^{ip} x e^{ip} \, |n+m\rangle$$
$$= \sin\theta \left(\sqrt{n+m+1} T_{n,m+1}^{+} + \sqrt{n+m} T_{n,m-1}^{+} \right) - 2\frac{g}{\omega} \sin\theta \cos\theta T_{n,m}^{+} \, .$$

The generalized Laguerre polynomials obey the following relations:

$$(m+x)L_n^m(x) = x L_n^{m+1}(x) + (n+m) L_n^{m-1}(x) \, ,$$
$$(m-x)L_{n-m}^m(x) = x L_{n-m-1}^{m+1} + (n-m+1) L_{n-m+1}^{m-1}(x) \, .$$

This allows to simplify the matrix elements of A and $A^\dagger$ by using

$$\sqrt{n+m+1} T_{n,m+1}^{\pm} + \sqrt{n+m} T_{n,m-1}^{\pm} = \pm \left(\frac{m}{2p_0} + 2p_0 \right) T_{n,m}^{\pm}$$

for any $n \in \mathbb{N}_0$ and $m \in \mathbb{Z}$, $-n \le m < \infty$. Thus, we finally obtain the following compact form:

$$\langle n| \, A \, |n+m\rangle = \langle n| \, \frac{1}{\hbar g} e^{-ip} x e^{-ip} \, |n+m\rangle = -\frac{m}{2} \frac{\sin\theta}{\frac{g}{\omega} \cos\theta} T_{n,m}^{-} = -\frac{1}{\hbar g} \frac{m}{2} \frac{x_0}{p_0} T_{n,m}^{-} \, , \tag{5.9a}$$

$$\langle n| \, A^\dagger \, |n+m\rangle = \langle n| \, \frac{1}{\hbar g} e^{+ip} x e^{+ip} \, |n+m\rangle = +\frac{m}{2} \frac{\sin\theta}{\frac{g}{\omega} \cos\theta} T_{n,m}^{+} = +\frac{1}{\hbar g} \frac{m}{2} \frac{x_0}{p_0} T_{n,m}^{+} \, . \tag{5.9b}$$

Figure 5.1 shows a plot of the matrix element $\langle n| \, A \, |n+1\rangle$. The operators A and $A^\dagger$ have the following properties:

- All matrix elements $\langle n| \, A^{(\dagger)} \, |n+m\rangle$ are purely real, which is read off from Eqs. (5.8) and (5.9).

- For all $n \in \mathbb{N}$ we have $\langle n| \, A^{(\dagger)} \, |n\rangle = 0$.

- For $\theta = \pi/2$ the polaron transformation is a trivial transformation and $A = A^\dagger = a^\dagger + a$. Hence, the matrix elements show for $\theta = \pi/2$ the usual behavior of the creation and annihilation operators, $\langle n| \, A \, |n+1\rangle = \sqrt{n+1}$, known from the Jaynes-Cummings Hamiltonian (solid green line in Fig 5.1).
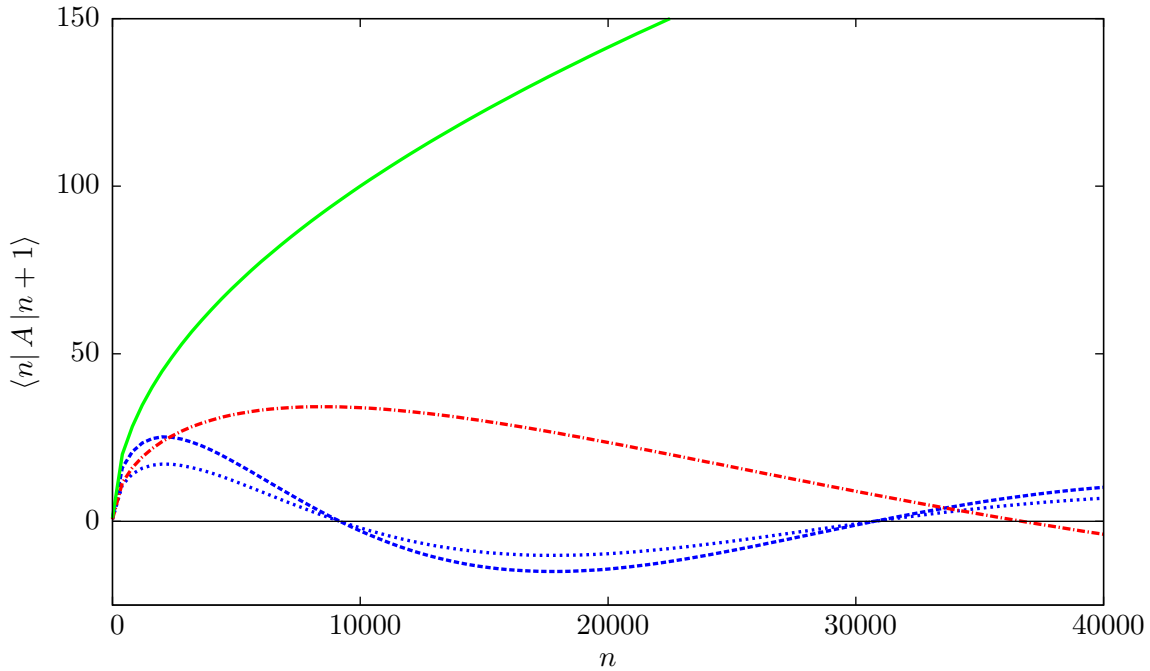
Figure 5.1.: Coupling matrix element $\langle n| A |n+1\rangle$ of the coupling operator $A = e^{-ip}xe^{-ip}/(\hbar g)$. For $\theta = \pi/2$ the coupling matrix elements reduce to the conventional Jaynes-Cummings coupling matrix elements, $\langle n| A |n+1\rangle = \sqrt{n+1}$, represented by the solid green line. For $\theta < \pi/2$ the coupling matrix elements have roots at photon numbers n_0^i. The position of these roots depends on $p_0 = \frac{g}{\omega}\cos\theta$. The blue curves have identical values of p_0, but different coupling strengths and mixing angles: Dashed line $g = 0.02\,\omega$ and $\theta = \pi/3$, dotted line $g = 0.012\,\omega$ and $\theta = \pi/5$. The red curve represents half the coupling strength, $g = 0.006\,\omega$ and $\theta = \pi/5$. Therefore, p_0 has half the value of the dotted blue line and the positions of the roots are shifted towards higher photon numbers.

- For $0 \leq \theta < \pi/2$ the polaron transformation is a nontrivial unitary transformation. At sufficiently small photon numbers n the matrix element grows proportional to $\sqrt{n+1}$. However, for larger n it deviates from the $\sqrt{n}$-behavior and exhibits oscillations. In particular, there are photon numbers n_0^i where the matrix element changes its sign. The index $i \in \mathbb{N}$ labels these photon numbers in an ascending order. In the following, we refer to them as "roots of the coupling matrix element". However, it should be noted that the matrix elements $\langle n| A |n + m\rangle$ are defined only for integer values of n and m. Hence, for arbitrary values of g, ω, and θ the value of the matrix element $\langle n_0^i| A |n_0^i + m\rangle$ is in general close to zero, but not exactly zero.

- The matrix elements at a mixing angle $\theta = \pi/2$ are an upper bound for the matrix elements at arbitrary mixing angles $0 \leq \theta \leq \pi/2$:

$$\langle n| A |n+1\rangle \leq \sqrt{n+1}\,.$$

- For $0 \leq \theta < \pi/2$ the positions of the roots of the coupling matrix elements depend on the quantity $p_0 = \frac{g}{\omega}\cos(\theta)$. If p_0 is increased, the positions n_0^i of the roots decrease (compare the dotted blue and dash-dotted red line in Fig. 5.1). Hence, for a given resonator frequency ω the positions of the roots can be adjusted either via the coupling strength g or via the mixing angle θ.

- For a small mixing angle θ, i.e., almost pure σ_z coupling, the positions n_0^i of the roots converge to constant values, but the amplitude of the coupling matrix elements tends to zero. The positions of the roots n_0^i for a small mixing angle θ are defined by the

asymptotic value of p_0,

$$\lim_{\theta \to 0} p_0 = \frac{g}{\omega} \, .$$

Therefore, the first root of the matrix elements, n_0^1, is always at a finite photon number $n_0^1 > 0$. However, the amplitude of the matrix elements depends on θ, too, and decays proportional to θ:

$$\langle n| \, A^{(\dagger)} \, |n + m\rangle = \pm \frac{m}{2} \frac{\omega}{g} \tan(\theta) T_{n,m}^{\pm} \approx \pm \frac{m}{2} \frac{\omega}{g} \theta T_{n,m}^{\pm} \, , \tag{5.10}$$

where $A^\dagger$ takes the upper sign.

5.4. Stationary photon statistics in the polaron frame

5.4.1. Recursion relation of the photon statistics

In this section the quantum master equation (5.7) is solved analytically for the stationary photon statistics of the laser, following the path described in Ref. [17]. We assume that only resonant transitions occur in the Hamiltonian H:

$$\langle n| \, A \, |n + m\rangle = 0 \text{ and } \langle n + m| \, A^\dagger \, |n\rangle = 0 \text{ if } m \neq 1 \, .$$

This assumption is equivalent to a rotating wave approximation and is justified in Sec. 5.7.

The photon statistics $\rho(n)$ of the laser is given by the diagonal entries of the reduced density matrix of the resonator, ρ^{res},

$$\rho(n) = \langle n| \, \rho^{\text{res}} \, |n\rangle = \sum_\sigma \langle \sigma, n| \, \rho \, |\sigma, n\rangle \, .$$

The equation of motion of ρ^{res} is obtained by tracing out the atomic degrees of freedom in the full master equation (5.7),

$$\frac{\mathrm{d}}{\mathrm{d}t} \rho^{\text{res}} = -i\omega \left[a^\dagger a, \rho^{\text{res}} \right] - ig \, \mathrm{Tr}_{\text{atom}} \left(\left[\sigma_+ A + \sigma_- A^\dagger, \rho \right] \right) + L_{\text{R}} \rho^{\text{res}} \, . \tag{5.11}$$

Details of this step are given in the Appendix C. Because of the interaction term the equation of motion of the reduced density matrix ρ^{res} is still coupled to the master equation (5.7) of the full density matrix ρ.

To simplify this system of differential equations we decouple the dynamics of atomic processes and changes of the resonator state by an adiabatic approximation [40]. The Lindblad superoperator $L_{\text{Q}} \rho$ describes atomic decay processes that happen on a timescale of $\Gamma_\uparrow^{-1}$, $\Gamma_\downarrow^{-1}$, and $(\Gamma_\varphi^*)^{-1}$. Resonator decay processes described by $L_{\text{R}} \rho$ happen on a timescale of κ^{-1}. For typical lasing parameters it holds $\kappa \ll \Gamma_\uparrow, \Gamma_\downarrow, \Gamma_\varphi^*$ and, therefore, we neglect decay processes of the resonator in the full master equation (5.7). This yields the following simplified system of coupled differential equations:

$$\frac{\mathrm{d}}{\mathrm{d}t} \rho^{\text{res}} = -i\omega \left[a^\dagger a, \rho^{\text{res}} \right] - ig \, \mathrm{Tr}_{\text{atom}} \left(\left[\sigma_+ A + \sigma_- A^\dagger, \rho \right] \right) + L_{\text{R}} \rho^{\text{res}} \, , \tag{5.12a}$$

$$\frac{\mathrm{d}}{\mathrm{d}t} \rho = -\frac{i}{\hbar} \left[H, \rho \right] + L_{\text{Q}} \rho \, . \tag{5.12b}$$

In order to obtain the stationary photon statistics we calculate the stationary solution of Eq. (5.12a) for the diagonal elements of the reduced density matrix ρ^{res}. The matrix elements of ρ and ρ^{res} are denoted by $\rho_{\sigma,n;\tau,m} = \langle \sigma, n| \, \rho \, |\tau, m\rangle$ and $\rho_{n,m} = \langle n| \, \rho^{\text{res}} \, |m\rangle$,

respectively. To evaluate the trace over the interaction term in Eq. (5.12a) we need to know the matrix elements $\rho_{\uparrow,n;\downarrow,n+1}$ and $\rho_{\downarrow,n+1;\uparrow,n}$, which are obtained from the stationary solution of Eq. (5.12b) as follows: Defining the vector

$$
\boldsymbol{R}_{n,m} = \begin{pmatrix} \rho_{\uparrow,n;\uparrow,m} \\ \rho_{\uparrow,n;\downarrow,m+1} \\ \rho_{\downarrow,n+1;\uparrow,m} \\ \rho_{\downarrow,n+1;\downarrow,m+1} \end{pmatrix}
$$

and using $\rho_{n,m} = \rho_{\uparrow,n;\uparrow,m} + \rho_{\downarrow,n;\downarrow,m}$, Eq. (5.12b) is cast into a set of matrix differential equations

$$
\dot{\boldsymbol{R}}_{n,m} = M_{n,m} \cdot \boldsymbol{R}_{n,m} + \boldsymbol{A}_{n,m} \tag{5.13}
$$

for each photon number $n, m \in \mathbb{N}_0$. The matrix $M_{n,m}$ and the vector $\boldsymbol{A}_{n,m}$ are given by

$$
M_{n,m} = \begin{pmatrix} -i\omega(n-m) - \Gamma_1 & ig\langle m+1|A^\dagger|m\rangle & -ig\langle n|A|n+1\rangle & 0 \\ ig\langle m|A|m+1\rangle & -i\Delta - i\omega(n-m) - \Gamma_\varphi & 0 & -ig\langle n|A|n+1\rangle \\ -ig\langle n+1|A^\dagger|n\rangle & 0 & i\Delta - i\omega(n-m) - \Gamma_\varphi & ig\langle m+1|A^\dagger|m\rangle \\ 0 & -ig\langle n+1|A^\dagger|n\rangle & ig\langle m|A|m+1\rangle & -i\omega(n-m) - \Gamma_1 \end{pmatrix},
$$

$$
\boldsymbol{A}_{n,m} = \begin{pmatrix} \Gamma_\uparrow \rho_{n,m} \\ 0 \\ 0 \\ \Gamma_\downarrow \rho_{n+1,m+1} \end{pmatrix}.
$$

We introduced the abbreviations $\Gamma_1 = \Gamma_\uparrow + \Gamma_\downarrow$ and $\Gamma_\varphi = \Gamma_1/2 + \Gamma_\varphi^*$. The dynamics of the photon field in the resonator enter Eq. (5.13) via the matrix elements of the reduced density matrix ρ^{res} in the vector $\boldsymbol{A}_{n,m}$. According to the adiabatic approximation the vector $\boldsymbol{A}_{n,m}$ changes slowly compared to $\boldsymbol{R}_{n,m}$. Therefore, transient processes in $\boldsymbol{R}_{n,m}$ can be neglected and we take the stationary solution of Eq. (5.13),

$$
\boldsymbol{R}_{n,m} = -M_{n,m}^{-1} \cdot \boldsymbol{A}_{n,m} \ ,
$$

which yields for $n = m$

$$
\rho_{\uparrow,n;\downarrow,n+1} = g\Gamma_1 \frac{\langle n|A|n+1\rangle}{\det M_{n,n}} \left[\rho_{n,n}\Gamma_\uparrow(\Delta + i\Gamma_\varphi) - \rho_{n+1,n+1}\Gamma_\downarrow(\Delta + i\Gamma_\varphi) \right] , \tag{5.14a}
$$

$$
\rho_{\downarrow,n+1;\uparrow,n} = g\Gamma_1 \frac{\langle n+1|A^\dagger|n\rangle}{\det M_{n,n}} \left[\rho_{n,n}\Gamma_\uparrow(\Delta - i\Gamma_\varphi) - \rho_{n+1,n+1}\Gamma_\downarrow(\Delta - i\Gamma_\varphi) \right] , \tag{5.14b}
$$

$$
\det M_{n,n} = 4g^2\Gamma_1\Gamma_\varphi \langle n+1|A^\dagger|n\rangle \langle n|A|n+1\rangle + \Gamma_1^2\Delta^2 + \Gamma_1^2\Gamma_\varphi^2 \tag{5.14c}
$$

$$
= \Gamma_1^2\Gamma_\varphi^2 \left(1 + \frac{4g^2}{\Gamma_1\Gamma_\varphi}N_n \right) ,
$$

$$
N_n = \frac{\Delta^2}{4g^2}\frac{\Gamma_1}{\Gamma_\varphi} + \langle n+1|A^\dagger|n\rangle \langle n|A|n+1\rangle . \tag{5.14d}
$$

By defining the quantity $\mathcal{A} = \frac{2g^2}{\Gamma_1\Gamma_\varphi}$ the equation of motion for $\rho_{n,n}$ can be expressed as follows:

$$
\begin{aligned}
\frac{\mathrm{d}}{\mathrm{d}t}\rho_{n,n} =\ & \kappa(N_{\mathrm{th}}+1)(n+1)\rho_{n+1,n+1} - \kappa N_{\mathrm{th}}(n+1)\rho_{n,n} \\
& - \kappa(N_{\mathrm{th}}+1)n\rho_{n,n} + \kappa N_{\mathrm{th}}n\rho_{n-1,n-1} \\
& + \frac{\mathcal{A}}{1+2\mathcal{A}N_n}|\langle n|A|n+1\rangle|^2 \left(\Gamma_\downarrow\rho_{n+1,n+1} - \Gamma_\uparrow\rho_{n,n} \right) \\
& - \frac{\mathcal{A}}{1+2\mathcal{A}N_{n-1}}|\langle n-1|A|n\rangle|^2 \left(\Gamma_\downarrow\rho_{n,n} - \Gamma_\uparrow\rho_{n-1,n-1} \right) .
\end{aligned} \tag{5.15}
$$

For the stationary case a detailed balance condition applies and this equation separates into two recursion relations for the diagonal elements of ρ^{res},

$$\left(\kappa(N_{\mathrm{th}} + 1)n + \frac{\mathcal{A}}{1 + 2\mathcal{A}N_{n-1}} \left| \langle n - 1 | A | n \rangle \right|^2 \Gamma_\downarrow \right) \rho_{n,n}$$

$$= \left(\kappa N_{\mathrm{th}} n + \frac{\mathcal{A}}{1 + 2\mathcal{A}N_{n-1}} \left| \langle n - 1 | A | n \rangle \right|^2 \Gamma_\uparrow \right) \rho_{n-1,n-1} \, .$$

The second relation differs only by a shift $n \to n + 1$ and does not provide any further information. By reordering terms we find the following recursion relation for $\rho_{n,n}$:

$$\rho_{n,n} = f_n \rho_{n-1,n-1} \, , \tag{5.16a}$$

$$f_n = \frac{\kappa N_{\mathrm{th}} n + \Gamma_\uparrow \frac{\mathcal{A}}{1+2\mathcal{A}N_{n-1}} \left| \langle n - 1 | A | n \rangle \right|^2}{\kappa(N_{\mathrm{th}} + 1)n + \Gamma_\downarrow \frac{\mathcal{A}}{1+2\mathcal{A}N_{n-1}} \left| \langle n - 1 | A | n \rangle \right|^2} \, . \tag{5.16b}$$

The photon statistics $\rho(n) \equiv \rho_{n,n}$ is uniquely defined by Eq. (5.16a) and the normalization condition of the density matrix, $\mathrm{Tr}_n(\rho^{\mathrm{res}}) = 1$. It has a local maximum at photon numbers $n_{\max}$ that fulfill $f_{n_{\max}} = 1$ and $f'_{n_{\max}} < 0$.

The recursion coefficient f_n is defined only for integer values of n because it contains the matrix elements $\langle n - 1 | A | n \rangle$. In the following we denote by f'_n the value of the symmetric difference quotient

$$f'_n = \frac{f_{n+1} - f_{n-1}}{2} \, ,$$

which is the common definition of the derivative of functions with a discrete support.

5.4.2. Properties of the recursion coefficient

Before evaluating the recursion relation (5.16) in Sec. 5.4.3 we now investigate the properties of the recursion coefficient f_n.

In Fig. 5.2 the recursion coefficient f_n is compared to the result obtained for a conventional laser with pure σ_x coupling, i.e., $\theta = \pi/2$ (solid red vs. dotted blue curve). By introducing the effective atomic pumping and relaxation rates

$$\Gamma_{n \to n+1} = \frac{\mathcal{A}}{1 + 2\mathcal{A}N_n} \left| \langle n | A | n + 1 \rangle \right|^2 \Gamma_\uparrow \quad \text{and} \tag{5.17a}$$

$$\Gamma_{n+1 \to n} = \frac{\mathcal{A}}{1 + 2\mathcal{A}N_n} \left| \langle n | A | n + 1 \rangle \right|^2 \Gamma_\downarrow \, , \tag{5.17b}$$

the recursion coefficient can be rewritten in a compact form,

$$f_n = \frac{\kappa N_{\mathrm{th}} n + \Gamma_{n-1 \to n}}{\kappa(N_{\mathrm{th}} + 1)n + \Gamma_{n \to n-1}} \, . \tag{5.18}$$

The properties of the recursion coefficient are determined by the interplay of the resonator excitation and decay rates, $\kappa N_{\mathrm{th}} n$ and $\kappa(N_{\mathrm{th}} + 1)n$, and the corresponding effective atomic pumping and decay rates, $\Gamma_{n \to n+1}$ and $\Gamma_{n+1 \to n}$. The effective pumping and relaxation rates vanish at the roots n_0^i of the coupling matrix element $\langle n | A | n + 1 \rangle$. The recursion coefficient f_n has the following properties:

- The recursion coefficient for pure σ_x coupling, $f_n(\theta = \pi/2)$, is an upper bound for the recursion coefficient $f_n(\theta)$ at arbitrary mixing angles $0 \le \theta < \pi/2$,

$$f_n(\theta) \le f_n\left(\frac{\pi}{2}\right) \, ,$$
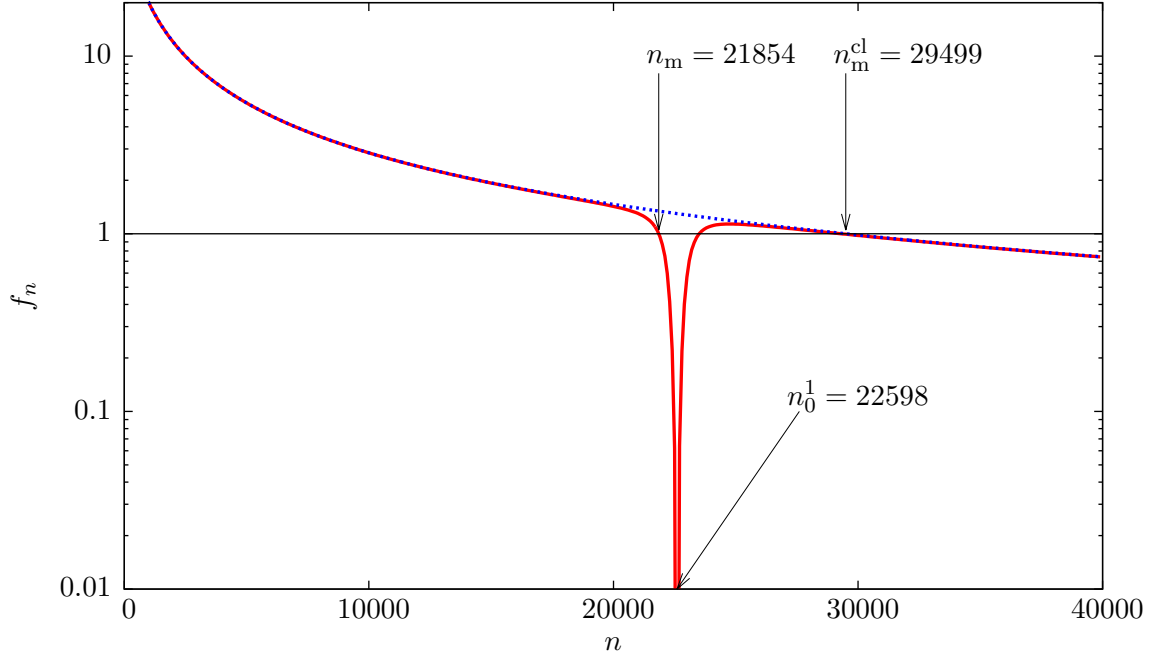
Figure 5.2.: Recursion coefficient f_n of a single-atom laser. The dotted blue line represents f_n for a conventional laser, i.e., $\theta = \pi/2$. The solid red line represents f_n for a laser with 90% σ_z coupling, i.e., $\theta = \pi/10$. Arrows indicate the maximum of the photon distribution for a conventional laser, n_m^cl, for the laser with additional σ_z couplings, n_m, and the first root of the coupling matrix element, n_0^1. Plot parameters are $g = 0.0067\,\omega$, $\Gamma_\uparrow = 0.006\,\omega$, $\Gamma_\downarrow = 0.0001\,\omega$, $\Gamma_\varphi^* = 0.001\,\omega$, $\Delta = 0\,\omega$, $N_\mathrm{th} = 0$, and $\kappa = 1 \times 10^{-7}\,\omega$.

because of the following reason: As discussed in Sec. 5.3 the matrix elements $\langle n|\, A\, |n+1\rangle$ have an upper bound $\langle n|\, A\, |n+1\rangle \le \sqrt{n+1}$, where the equality holds for $\theta = \pi/2$. This implies the following bound on the effective pumping rates:

$$\Gamma_{n \to n+1/n+1 \to n} \le \frac{\mathcal{A}(n+1)}{1 + 2\mathcal{A}\left(\frac{\Delta^2}{4g^2}\frac{\Gamma_1}{\Gamma_\varphi} + n + 1\right)} \Gamma_{\uparrow/\downarrow}\,.$$

For typical lasing parameters we have $\Gamma_\uparrow > \Gamma_\downarrow$, which finally yields

$$f_n(\theta) \le f_n\left(\frac{\pi}{2}\right) = \frac{\kappa N_\mathrm{th} n + \Gamma_\uparrow \dfrac{\mathcal{A}n}{1 + 2\mathcal{A}\left(\frac{\Delta^2}{4g^2}\frac{\Gamma_1}{\Gamma_\varphi} + n\right)}}{\kappa(N_\mathrm{th}+1)n + \Gamma_\downarrow \dfrac{\mathcal{A}n}{1 + 2\mathcal{A}\left(\frac{\Delta^2}{4g^2}\frac{\Gamma_1}{\Gamma_\varphi} + n\right)}}\,.$$

- For a resonant atom, $\Delta = 0$, and $\frac{1}{\mathcal{A}} = \frac{\Gamma_1\Gamma_\varphi}{2g^2} \ll 2n$ the recursion coefficient $f_n(\pi/2)$ is independent of the coupling strength g. In this regime the maximum of the photon distribution depends only on the bare pumping and loss rates $\Gamma_\uparrow$, $\Gamma_\downarrow$, and κ.

- The photon statistics $\rho(n)$ has a local maximum at photon numbers n_m where the conditions $f_{n_\mathrm{m}} = 1$ and $f'_{n_\mathrm{m}} < 0$ hold. For a conventional laser with pure σ_x coupling $f_n(\pi/2)$ is a monotonically decreasing function and there is exactly one maximum of the photon distribution, situated at

$$n_\mathrm{m}^\mathrm{cl} = \frac{1}{2}\left(\frac{\Gamma_\uparrow - \Gamma_\downarrow}{\kappa} - \frac{1}{\mathcal{A}}\right) - \frac{\Delta^2}{4g^2}\frac{\Gamma_1}{\Gamma_\varphi}\,.$$

For generalized couplings there are roots n_0^i of the coupling matrix elements where f_n takes the value

$$f_{n_0^i} = \frac{N_{\text{th}}}{N_{\text{th}} + 1} < 1 \,.$$

Hence, near each root of the coupling matrix element $f_n(\theta)$ deviates from the conventional recursion coefficient, $f_n(\pi/2)$, and drops down to the value $f_{n_0^i} < 1$. Therefore, near each root n_0^i of the coupling matrix element the conditions $f_n = 1$ and $f_n' < 0$ are fulfilled and additional local maxima of the photon statistics occur.

- For typical lasing experiments with artificial atoms at low temperature, it holds $N_{\text{th}} \approx 0$. Then, the recursion coefficient for a conventional laser, $f_n(\pi/2)$, reduces to

$$f_n\left(\frac{\pi}{2}\right) \propto \frac{\Gamma_\uparrow}{2\kappa} \frac{1}{n} \,.$$

A similar behavior is found for $f_n(\theta)$ at arbitrary mixing angles θ: For a sufficiently small effective relaxation rate, $\Gamma_{n \to n-1} \ll \kappa n$, the recursion coefficient is approximated by

$$f_n(\theta) \approx \frac{\Gamma_{n-1 \to n}}{\kappa n} \,.$$

For photon numbers n far away from the roots n_0^i of the coupling matrix elements the right-hand side simplifies to the same form as $f_n(\pi/2)$,

$$f_n(\theta) \approx \frac{\Gamma_\uparrow}{2\kappa} \frac{1}{n} \,. \tag{5.19}$$

However, close to the roots of the coupling matrix elements, i.e, if $n \approx n_0^i$ for an index $i \in \mathbb{N}$, the recursion coefficient $f_n(\theta)$ deviates significantly from the conventional behavior and is dominated by the dependence of the coupling matrix elements on the photon number,

$$f_n(\theta) \approx \frac{\Gamma_{n-1 \to n}}{\kappa n_0^i} = \frac{2g^2 \Gamma_\uparrow}{\Gamma_1 \Gamma_\varphi \kappa} \frac{|\langle n-1 | A | n \rangle|^2}{n_0^i} \,. \tag{5.20}$$

The range of photon numbers around the roots n_0^i where $f_n(\theta)$ deviates significantly from $f_n(\pi/2)$, is defined by the following condition:

$$|\langle n-1 | A | n \rangle|^2 \ll \frac{\Gamma_1 \Gamma_\varphi}{4g^2} \,.$$

This implies that the deviation range increases if the bare pumping, relaxation, and dephasing rates are chosen large or the coupling strength is chosen small.

- Depending on the values of the lasing parameters κ, $\Gamma_\uparrow$, and $\Gamma_\downarrow$ the recursion coefficient is bound from above by

$$f_n(\theta) \leq f_1(\theta) \leq \min\left(\frac{\Gamma_\uparrow}{\Gamma_\downarrow}, \frac{\Gamma_\uparrow}{2\kappa}\right) \,.$$

5.4.3. Numerical methods to calculate the photon statistics

Equation (5.16) can be evaluated numerically in order to obtain the photon statistics $\rho(n) \equiv \rho_{n,n}$ in a range of photon numbers $[n_{\text{lower}}, n_{\text{upper}}]$. The boundaries n_{lower} and n_{upper} should be chosen such that

1. the photon statistics $\rho(n)$ has probabilities close to zero at the edges of the interval, for instance $\rho(n_{\text{upper}}) = \rho(n_{\text{lower}}) = \mathcal{O}(10^{-100})$, and

2. all local maxima of the photon statistics with a probability of the order of unity are situated inside $[n_{\text{lower}}, n_{\text{upper}}]$. This condition is automatically fulfilled if $f_n > 1$ holds for all $n < n_{\text{lower}}$ and $f_n < 1$ holds for all $n > n_{\text{upper}}$.

Two numerical approaches to solve Eq. (5.16) have been implemented in WOLFRAM MATHEMATICA, version 9.0.1.0, and are described in the following.

First, the recursion relation (5.16) is evaluated directly. Therefore, an arbitrary initial photon number $n_{\text{i}} \in [n_{\text{lower}}, n_{\text{upper}}]$ and an arbitrary initial value $\rho(n_{\text{i}}) = \rho_{\text{i}}$ are chosen. Using Eq. (5.16) the values of $\rho(n)$ for all photon numbers in the considered range $[n_{\text{lower}}, n_{\text{upper}}]$ are calculated iteratively, starting from n_{i}. Once $\rho(n)$ has been calculated for all $n \in [n_{\text{lower}}, n_{\text{upper}}]$, the probability distribution is renormalized such that the normalization condition of the density matrix is fulfilled,

$$\text{Tr}_n\left(\rho^{\text{res}}\right) \approx \sum_{n=n_{\text{lower}}}^{n_{\text{upper}}} \rho(n) \overset{!}{=} 1 . \tag{5.21}$$

The trace over the resonator states is restricted to the interval $[n_{\text{lower}}, n_{\text{upper}}]$ because we assumed that the photon statistics has only peaks of the order of unity inside this interval and that $\rho(n)$ vanishes at the edges of the interval. In order to ensure numerical convergence of this algorithm the initial photon number n_{i} should be chosen close to the actual maximum of the photon statistics, n_{m}, and the initial value of the distribution, ρ_{i}, should be chosen not too small, e.g., of the order of unity.

Alternatively, we calculate the exponent R_n of the photon statistics,

$$\rho_{n,n} = e^{-R_n} . \tag{5.22}$$

Then, Eq. (5.16a) takes the form

$$R_n = -\log\left(f_n\right) + R_{n-1} . \tag{5.23}$$

In order to calculate the exponent R_n in the range $[n_{\text{lower}}, n_{\text{upper}}]$, we choose an arbitrary initial value for $R_{n_{\text{lower}}}$ and evaluate Eq. (5.23) iteratively for all photon numbers up to n_{upper}. There is a photon number n_{ext} where the exponent R_n takes its minimal value $R_{n_{\text{ext}}}$. As last step before calculating the actual photon statistics $\rho(n)$, R_n is shifted by the value of this minimum,

$$R_n \to \tilde{R}_n = R_n - R_{n_{\text{ext}}} . $$

This shift ensures that the photon statistics $\rho(n)$ obtained by applying Eq. (5.22) on $\tilde{R}_n$ has approximately the right order or magnitude: $\tilde{R}_{n_{\text{ext}}} = 0$ corresponds to the main peak of $\rho(n)$, which then has the probability $\rho(n_{\text{ext}}) = 1$. Finally, $\rho(n)$ is normalized to unity by imposing the condition (5.21).

Figure 5.3 compares numerical results for the photon statistics $\rho(n)$ obtained by the two different algorithms. If they are implemented in MATHEMATICA using symbolic calculation, both algorithms yield identical results. However, in a purely numeric programming
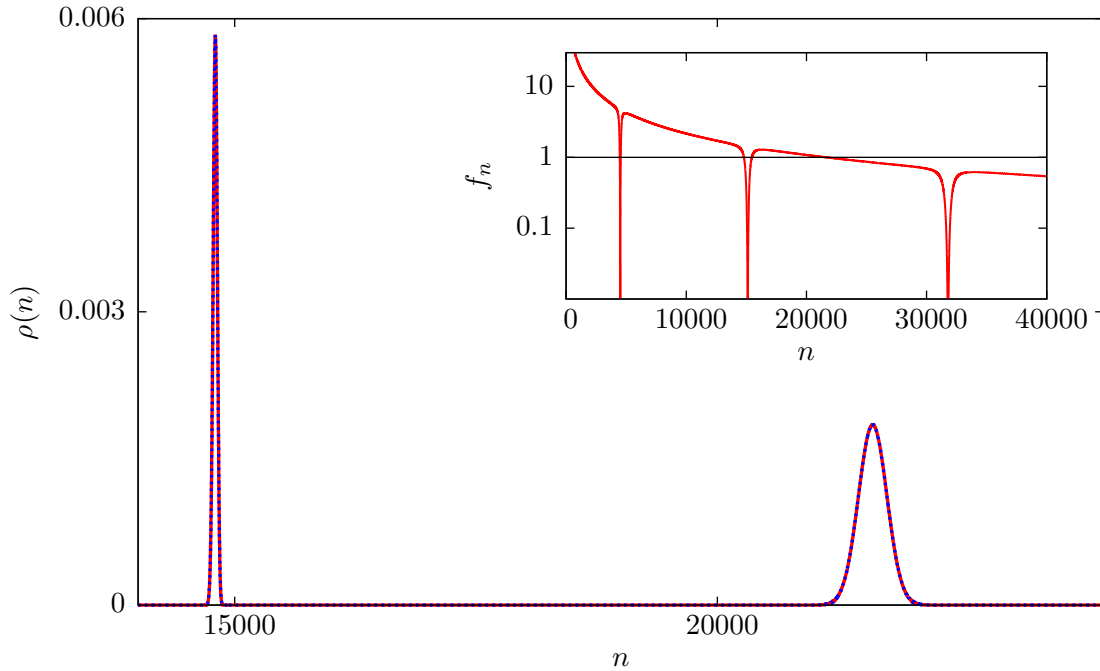
Figure 5.3.: Comparison of the numerical methods to calculate a double-peaked photon statistics. The solid red curve of the main plot is obtained using the direct evaluation of Eq. (5.16) whereas the coinciding dotted blue curve represents result obtained from the logarithmized recursion relation (5.22). The numerical differences of both results are smaller than 7×10^{-13}. **Inset**: recursion coefficient f_n. Plot parameters are $g = 0.015\,\omega$, $\theta = \pi/10$, $\Gamma_\uparrow = 0.006\,\omega$, $\Gamma_\downarrow = 0\,\omega$, $\Gamma_\varphi^* = 0.001\,\omega$, $\Delta = 0\,\omega$, $\kappa = 1.384 \times 10^{-7}\,\omega$, and $N_{\mathrm{th}} = 0$.

language the direct evaluation of the recursion relation is expected to be numerically less stable because of the following reasons: Away from the main peaks the photon statistics $\rho(n)$ takes very small values, e.g., of the order of 10^{-350} at $n = 15450$. These values may easily underflow the range of floating point values representable on a computer. Furthermore, multiplication of small numbers is prone to numerical errors. In the direct evaluation of Eq. (5.16) such a multiplication is performed in every iteration step and numerical errors add up. Hence, in a purely numeric programming language a single-peak photon statistics is calculated properly when the starting photon number n_{i} is chosen close to the maximum photon number n_{max}. But if the photon statistics has two or more peaks, the numerical results may diverge at the peaks far away of the initial photon number n_{i}. The logarithmic evaluation circumvents these problems because the values of R_n are of an order of magnitude that can easily be represented by a computer. Second, multiplication is replaced by addition circumventing numerical errors of multiplication of very small numbers.

In conclusion, in a symbolic programming language like MATHEMATICA both algorithms yield identical results, shown in Fig. 5.3, which is also a crosscheck of the implementation. However, in a purely numeric evaluation the evaluation of the logarithmized recursion relation (5.22) is expected to be numerically more stable.

5.5. Photon-number squeezing

A new feature of a laser built out of artificial atoms with additional longitudinal couplings to the radiation field is the presence of roots of this coupling. This changes the recursion coefficient f_n significantly compared to a conventional laser. In this section we examine the impact of these roots on the photon statistics $\rho(n)$. The photon statistics is expected to
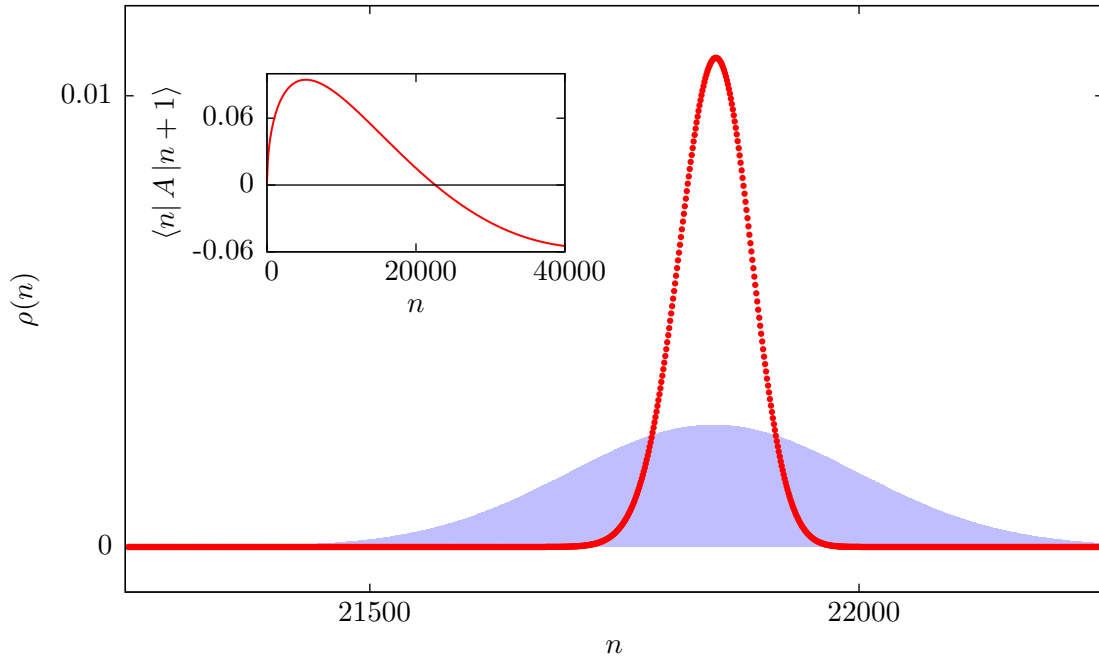
Figure 5.4.: Photon statistics of a single-atom laser. Red dots represent the photon statistics corresponding to the recursion coefficient f_n plotted in red in Fig. 5.2, i.e., 90% σ_z coupling or a mixing angle $\theta = \pi/10$. **Inset**: Coupling matrix element. The first root of the coupling matrix element at $n_0^1 = 22598$ causes the photon statistics to be peaked at the photon number $n_{\mathrm{m}} = 21854$ with a photon-number expectation value $\langle n \rangle = 21851$ and a Fano factor $F = 0.062$ in the cavity frame. The filled faint blue curve represents the Poissonian photon statistics of a conventional laser operating at the same photon-number expectation value $\langle n \rangle$, which has a Fano factor $F = 1$. Plot parameters are $g = 0.0067\,\omega$, $\Gamma_\uparrow = 0.006\,\omega$, $\Gamma_\downarrow = 0.0001\,\omega$, $\Gamma_\varphi^* = 0.001\,\omega$, $\Delta = 0\,\omega$, $N_{\mathrm{th}} = 0$, and $\kappa = 1 \times 10^{-7}\,\omega$.

deviate significantly from the one of a conventional laser if its photon-number expectation value $\langle n \rangle$ is close to a root n_0^i of the coupling matrix element. The red dots in Fig. 5.4 are numerical results for the photon statistics $\rho(n)$ corresponding to such lasing parameters. We compare this photon statistics to a Poissonian distribution with the same photon number expectation value $\langle n \rangle$, which is the result obtained for a conventional laser with only σ_x couplings (filled faint blue curve). For the given lasing parameters the photon statistics obtained for a laser with additional longitudinal couplings is much narrower than a Poissonian distribution, i.e., the laser has a sub-Poissonian or photon-number squeezed statistics. We use the Fano factor introduced in chapter 3 to quantify the squeezedness of the photon statistics $\rho(n)$.

5.5.1. Corrections to the Fano factor due to the polaron transformation

In Sec. 5.2 we introduced the polaron frame with the basis states $|\sigma, n\rangle$. All calculations in this chapter are performed in this basis. In particular, the photon statistics $\rho(n)$ is defined in the polaron frame. However, the Fano factor F given by Eq. (3.2) is defined with respect to the cavity photon states $|n_{\mathrm{c}}\rangle$, i.e., in the notation of this chapter it has the form

$$F = \frac{\langle n_{\mathrm{c}}^2 \rangle - \langle n_{\mathrm{c}} \rangle^2}{\langle n_{\mathrm{c}} \rangle} \,.$$

In order to calculate the Fano factor F out of a photon statistics in the polaron frame the expectation values $\langle n_{\mathrm{c}}^2 \rangle$ and $\langle n_{\mathrm{c}} \rangle$ have to be transformed to the polaron frame, which gives

rise to additional correction terms. For an arbitrary operator O it holds

$$\langle O_\mathrm{c} \rangle = \sum_{n,\sigma} \langle \sigma, n_\mathrm{c} | \, \rho_\mathrm{c} O_\mathrm{c} \, | \sigma, n_\mathrm{c} \rangle$$

$$= \sum_{n,\sigma} \langle \sigma, n_\mathrm{c} | \, UU^\dagger \rho_\mathrm{c} UU^\dagger O_\mathrm{c} UU^\dagger \, | \sigma, n_\mathrm{c} \rangle$$

$$= \sum_{n,\sigma} \langle \sigma, n | \, \rho O_\mathrm{p} \, | \sigma, n \rangle \, ,$$

where ρ and ρ_c are the density matrices in the polaron and the cavity frame, respectively. The polaron-transformed operators n_p and n_p^2 are given by

$$n_\mathrm{p} = U^\dagger a^\dagger a U = a^\dagger a - \xi \left(a + a^\dagger \right) + \xi^2 \, , \tag{5.24a}$$

$$n_\mathrm{p}^2 = a^\dagger a a^\dagger a - \xi \left(a^\dagger a \left(a + a^\dagger \right) + \left(a^\dagger + a \right) a^\dagger a \right)$$

$$+ \, \xi^2 \left(a^2 + \left(a^\dagger \right)^2 + 4 a^\dagger a + 1 \right) - 2 \xi^3 \left(a + a^\dagger \right) + \xi^4 \, , \tag{5.24b}$$

$$\xi = p_0 \sigma_z \, . \tag{5.24c}$$

For the stationary density matrix the relations $\rho_{\sigma,n;\sigma,n\pm1} = 0$ and $\rho_{\sigma,n;\sigma,n\pm2} = 0$ hold [41]. Hence, all terms containing an odd power of field operators and all terms proportional to a^2 and $(a^\dagger)^2$ vanish, yielding

$$F = \frac{\sum_{n=0}^{\infty} \left(n^2 + 2 p_0^2 n \right) \rho_{n,n} - \left(\sum_{n=0}^{\infty} n \rho_{n,n} \right)^2 + p_0^2}{\sum_{n=0}^{\infty} n \rho_{n,n} + p_0^2} \, .$$

For typical lasing parameters we have $p_0^2 \ll 1 \ll \langle n \rangle$, which allows to rewrite the Fano factor in the following form:

$$F = F_\mathrm{p} + 2 p_0^2 \, ,$$

$$F_\mathrm{p} = \frac{\langle n^2 \rangle - \langle n \rangle^2}{\langle n \rangle} \, ,$$

where F_p is the Fano factor calculated in the polaron frame out of the polaron-frame photon statistics $\rho(n)$. For the single-atom case the correction $2 p_0^2 \ll 1$ does not change the value of F_p significantly. For instance, for the photon statistics shown in Fig. 5.4 we obtain $F_\mathrm{p} = 0.0621$ in the polaron frame and $F = 0.0622$ in the cavity frame. However, for the multi-atom case discussed in Sec. 5.10 larger corrections may arise, depending on the lasing parameters.

5.5.2. An estimate of the Fano factor

The results of the previous section are sufficient to calculate F and F_p numerically. However, in order to gain insight into the physics of photon-number squeezing we derive an estimate of the Fano factor F_p in the polaron frame. This estimate connects the value of F_p to the slope of the recursion coefficient f_n at the photon number n_max corresponding to the maximum of the photon statistics.

As discussed in Sec. 5.4 the position n_max of the maximum of the photon statistics is defined by $f_{n_\mathrm{max}} = 1$ and $f'_{n_\mathrm{max}} < 0$. We linearize f_n around the photon number n_max,

$$f_n \approx f_n^\mathrm{lin} = 1 - c(n - n_\mathrm{max}) \, , \tag{5.25}$$

where $c = -f'_{n_\mathrm{max}} > 0$ is the absolute value of the slope of the recursion coefficient f_n at n_max. If c is large compared to the slope of f_n for pure σ_x coupling, the photon statistics

$\rho(n)$ drops to zero in the vicinity of $n_{\max}$ faster than a Poissonian distribution. Then, the photon statistics $\rho(n)$ can be calculated using the linearized recursion relation $f_n^{\lin}$ because it is already close to zero in regions where the deviation between f_n and $f_n^{\lin}$ becomes significant. Using Eq. (5.25) we obtain the following photon statistics:

$$\rho_{\lin}(n) = \begin{cases} \rho_0(-c)^n \left(1 - \frac{1}{c} - n_{\max}\right)_n & 0 \leq n < n_{\max} + \frac{1}{c} \,, \\ 0 & \text{otherwise} \,. \end{cases}$$

The two cases arise from the fact that the linearized recursion coefficient is negative for photon numbers larger than $n_{\max} + 1/c$, yielding an unphysical probability distribution. We introduced the Pochhammer symbol

$$(x)_n = x(x+1) \ldots (x+n-1) = \frac{\Gamma(x+n)}{\Gamma(x)} \,.$$

The constant ρ_0 is determined by the normalization condition $\sum_{n=0}^{\infty} \rho(n) = 1$ and is bound from above by the corresponding value of a Poissonian distribution, $\rho_0 \lesssim e^{-n_{\max}}$.

For typical lasing setups $c \gg e^{-n_{\max}}$ is fulfilled. Then, the following expressions are obtained for the Fano factor and the photon number expectation value by using $\rho_{\lin}(n)$:

$$\langle n \rangle_{\lin} = n_{\max} - 1 \,, \tag{5.26a}$$

$$F_{\lin} = \frac{1}{c} \frac{1}{\langle n \rangle_{\lin}} = \frac{1}{c} \frac{1}{n_{\max} - 1} \,. \tag{5.26b}$$

In order to obtain a small Fano factor $F < 1$ a large photon-number expectation value $\langle n \rangle \approx n_{\max}$ and a steep slope c of the recursion coefficient at $n_{\max}$ are needed. The numerical value of c is smaller than unity because the recursion coefficient f_n decreases very slowly as a function of n. Therefore, c and $n_{\max}$ compete in order to get a small Fano factor. For example, for the lasing parameters used in Fig. 5.2 we have $n_{\max} \approx 2 \times 10^5$ and $c \approx 7 \times 10^{-4}$. The value of c is, however, still larger than the one obtained for a conventional laser, which would be $c \approx 5 \times 10^{-6}$.

5.5.3. Connection of squeezing and roots of the coupling matrix elements

The estimate (5.26b) allows for a physical interpretation how squeezing is connected to the presence of roots of the coupling.

For a single-peaked photon statistics the photon-number expectation value $\langle n \rangle$ is approximately given by the position $n_{\max}$ of the maximum of the photon statistics. The photon number $n_{\max}$ is determined by the conditions $f_{n_{\max}} = 1$ and $f'_{n_{\max}} < 0$. Equations (5.17) and (5.18) reveal that this conditions can be fulfilled in two different ways:

1. For photon numbers n far away from the roots n_0^i of the coupling matrix element the recursion coefficient f_n coincides with the recursion coefficient of a conventional laser. For a conventional laser there is a photon number $n_{\max}^{\cl}$ where the bare pumping and loss rates $\Gamma_\uparrow$, $\Gamma_\downarrow$, and κ are in balance. This photon number $n_{\max}^{\cl}$ depends linearly on $\Gamma_\uparrow$.

2. At the roots n_0^i of the coupling matrix elements the interaction between atom and resonator breaks down and f_n drops to a value smaller than unity. Therefore, there are additional photon numbers $n_{\max}^{\add}$ close to the roots n_0^i which also fulfill the criteria of a local maximum of the photon statistics. Their positions $n_{\max}^{\add}$ are defined by the roots n_0^i of the coupling matrix elements and, therefore, they depend on the quantity $p_0 = g \cos(\theta)/\omega$, but they are independent of the bare pumping rate $\Gamma_\uparrow$.

(a)

(b)

(c)

(d)
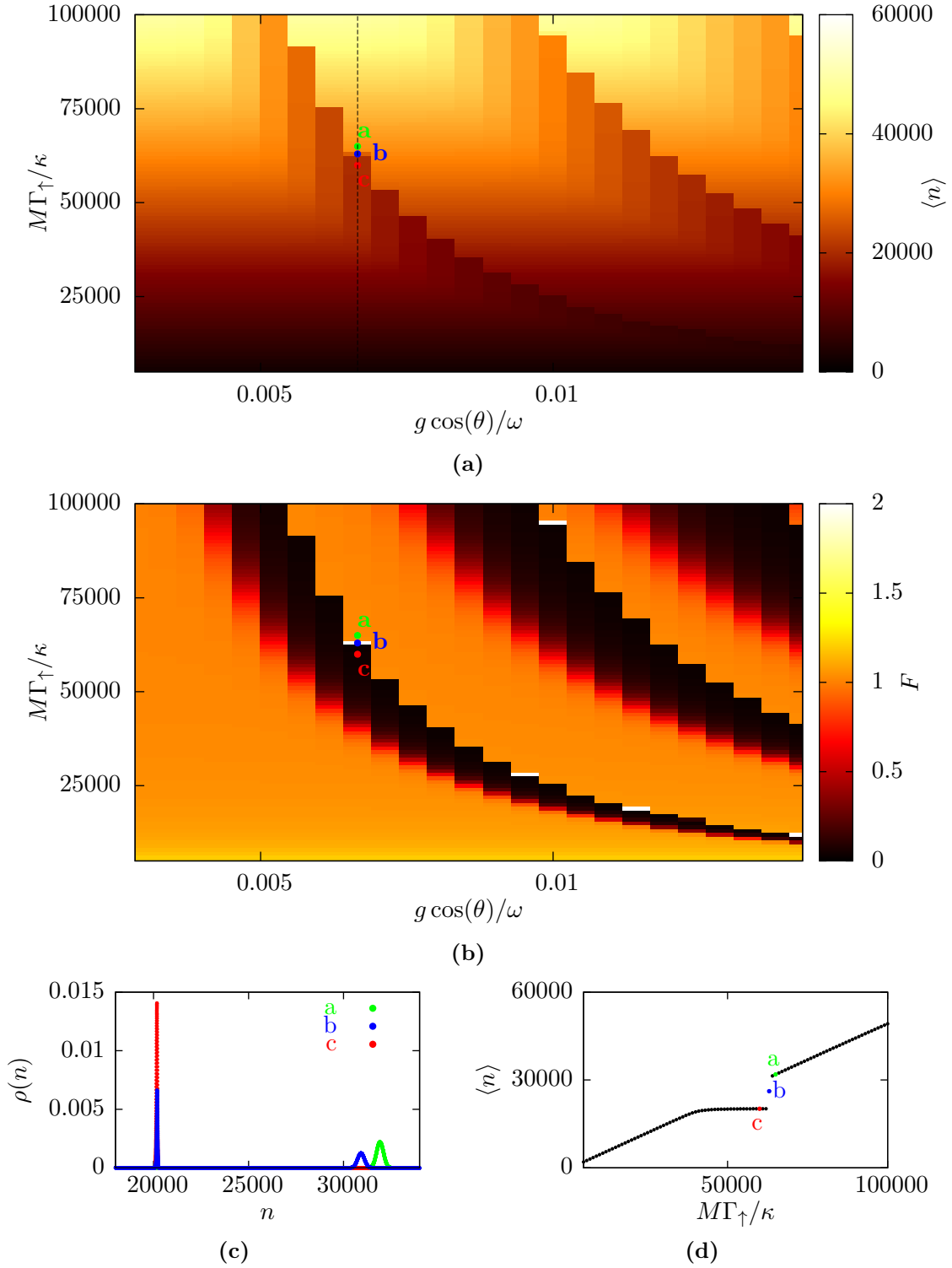
Figure 5.5.: Dependence of **(a)** the photon-number expectation value $\langle n \rangle$ and **(b)** the Fano factor F on the lasing parameters. Strongly photon-number squeezed light is obtained near each root n_0^i of the coupling. The positions n_0^i of the roots decrease for increasing $p_0 = g \cos(\theta)/\omega$. **(c)**: Polaron-frame photon statistics $\rho(n)$ for the three points a, b, and c marked in the density plots. They represent a transition from a "trapped" state to a conventional state. The Fano factor at the point b is much larger than unity because the photon statistics is double-peaked. **(d)**: Photon-number expectation value $\langle n \rangle$ as a function of $M\Gamma_\uparrow/\kappa$ for a fixed value of p_0. This figure is a cut through the density plot (a) along the dashed line indicated there. $\langle n \rangle$ increases linearly with the effective pumping rate, but it is trapped at roots of the coupling matrix elements and takes a constant value for a certain range of pumping rates. Plot parameters are $M = 1$, $N_{\text{th}} = 0$, $\Delta = 0\,\omega$, $\Gamma_\downarrow = \Gamma_\varphi^* = 0.0001\,\omega$, $\kappa = 1 \times 10^{-7}\,\omega$, and $\theta = \pi/10$. $g \in [0.003\,\omega, 0.015\,\omega]$ and $\Gamma_\uparrow \in [0.0005\,\omega, 0.01\,\omega]$. Other values of κ, $M \ll 100$, and $0 < \theta < \pi/4$ yield qualitatively the same plot.

In Fig. 5.5a the photon-number expectation value $\langle n \rangle$ is plotted as a function of the pumping rate $\Gamma_\uparrow$ and the coupling strength g. For a fixed coupling strength g the photon-number expectation value $\langle n \rangle$ increases linearly with the pumping rate as long as it is far away from roots n_0^i of the coupling matrix elements. This is the usual scaling behavior of a conventional laser, $\langle n \rangle \approx n_{\max}^{\mathrm{cl}} \propto \Gamma_\uparrow$, corresponding to the first scenario mentioned above. However, in the vicinity of a root n_0^i the photon number $\langle n \rangle$ gets "trapped" by this root, $\langle n \rangle \approx n_{\max}^{\mathrm{add}} \approx n_0^i$, and keeps constant for a certain range of pumping rates $\Gamma_\uparrow$. This trapping of the photon number is due to the breakdown of the coupling between the atom and the resonator and corresponds to the second scenario. It is clearly visible in Fig. 5.5d, where a cut through the density plot 5.5a at a constant coupling strength g is shown.

The photon statistics $\rho(n)$ describes the fluctuations of the photon number around its expectation value $\langle n \rangle$. The fluctuations arise as follows: For photon numbers $n < \langle n \rangle$ we have $f_n > 1$, i.e., the pumping process dominates and drives the system back to the photon-number expectation value. Likewise, for $n > \langle n \rangle$ losses dominate and, again, the system is driven back to the photon-number expectation value. Figure 5.5b shows that for the first scenario, $\langle n \rangle \approx n_{\max}^{\mathrm{cl}}$, the fluctuations have a Poissonian statistics characterized by a Fano factor $F = 1$ (cf., for instance, point "a" in Fig. 5.5b), which is the expected outcome for a conventional laser. However, if the photon-number expectation value $\langle n \rangle$ is trapped by a root, $\langle n \rangle \approx n_{\max}^{\mathrm{add}}$, fluctuations are strongly suppressed, which corresponds to a small Fano factor $F \ll 1$ (cf. point "c").

This can be understood as follows: If the photon-number expectation value $\langle n \rangle \approx n_{\max}^{\mathrm{add}}$ is trapped by a root, the bare pumping rate $\Gamma_\uparrow$ is larger than the bare loss rates $\Gamma_\downarrow$ and κ. This means that if there were not any roots of the coupling matrix elements, the laser would have a much larger photon-number expectation value $\langle n \rangle$, but it is trapped at $\langle n \rangle \approx n_{\max}^{\mathrm{add}}$ because of the breakdown of the effective pumping rates. If some loss process decreases the photon-number slightly, $n < n_{\max}^{\mathrm{add}}$, the coupling to the radiation field becomes nonzero again and the strongly pumped atom compensates the photon loss in the resonator immediately, driving the system back to the photon-number expectation value $\langle n \rangle \approx n_{\max}^{\mathrm{add}}$. Mathematically, the sudden increase in the photon creation rate for $n < n_{\max}^{\mathrm{add}}$ is represented by the inverse slope $1/c$ in the estimate (5.26b) of the Fano factor.

For some values of the pumping strength in Fig. 5.5b a Fano factor $F \gg 1$ is found. This occurs at the transition from a trapped state with a constant photon-number expectation value $\langle n \rangle$ to a conventional state with a linear scaling of $\langle n \rangle$ with the bare pumping rate $\Gamma_\uparrow$. An example of such a state is marked by the point "b" in Fig. 5.5b. At this transition the photon statistics is double-peaked and, therefore, the Fano factor is much larger than unity. The change of the photon statistics at such a transition is shown in Fig. 5.5c.

The axes in Fig. 5.5 are scaled by the quantities $M\Gamma_\uparrow/\kappa$ and $p_0 = g\cos(\theta)/\omega$. The latter determines the position of the roots n_0^i of the coupling. As shown by Eq. (5.19) the factor $M\Gamma_\uparrow/\kappa$ represents the dominant dependence of the recursion coefficient f_n on the lasing parameters. The factor M arising for a multi-atom setup is derived in Sec. 5.10.2. Because of this scaling of the axes the shown behavior of $\langle n \rangle$ and F is qualitatively the same for setups with a different number of atoms, $1 \leq M \ll 100$, a different resonator decay rate κ, or a different mixing angle $0 < \theta \ll \pi/4$.

In conclusion, the roots of the coupling matrix elements act like a valve that inhibits an increase of the photon number at n_0^i by suppressing the coupling of the atom to the resonator. Fluctuations around $\langle n \rangle$ are the more suppressed the more suddenly the coupling between atom and resonator breaks down in the vicinity of n_0^i, i.e., the more quickly the valve opens and closes. Mathematically, this is expressed by the inverse slope $1/c$ of the recursion coefficient in the estimate (5.26b) of the Fano factor. In order to obtain a strongly photon-number squeezed state the lasing parameters have to be chosen such that the

photon-number expectation value $\langle n \rangle$ is situated close to a root n_0^i of the coupling matrix elements.

5.6. Field strength in the resonator cavity

In this section we derive the field strength of the electric field in a coplanar waveguide resonator as a function of the photon-number expectation value $\langle n \rangle$. A coplanar waveguide resonator consists of a central box-shaped metallic conductor that is flanked by two grounded metal planes which are separated from the conductor by narrow gaps. The central conductor is assumed to be oriented along the z-axis from $z = 0$ to $z = L$. Its width and height are denoted by W and H, respectively. The canonically quantized electromagnetic field (cf. Sec. 3.1 and Ref. [35]) of a single resonator mode is

$$E(z,t) = \sqrt{\frac{\hbar\omega}{\epsilon_0 \epsilon_\mathrm{r} V}} \sin(kz) \left(a e^{-i\omega t} + a^\dagger e^{i\omega t} \right) .$$

The wave vector k must satisfy the boundary conditions, e.g., $E(0,t) = E(L,t) = 0$ if both sides of the conductor are connected to ground. The quantization volume is denoted by $V = LHW$ and ϵ_r is the effective electric permittivity. The electric field strength in the resonator is

$$\sqrt{\left\langle |E(z,t)|^2 \right\rangle} = 2\sqrt{\frac{\hbar\omega}{2\epsilon_0 \epsilon_\mathrm{r} V}} \sin(kz) \sqrt{\langle n \rangle + \frac{1}{2}} \approx E_0 \sin(kz) \sqrt{\langle n \rangle} .$$

Typical values of the resonator parameters are [42]

$$
\begin{aligned}
L &\approx 20\,\mathrm{mm}\,, & \epsilon_\mathrm{r} &\approx 5\,, \\
W &\approx 10\,\mathrm{\mu m}\,, & f &\approx 5\,\mathrm{GHz}\,, \\
H &\approx 200\,\mathrm{nm}\,.
\end{aligned}
$$

Hence, the prefactor E_0 is of the order of unity when measured in SI units and the dependence of the electric field strength on the photon-number expectation value is

$$\sqrt{\left\langle |E(z,t)|^2 \right\rangle} \approx 1.9 \frac{\mathrm{V}}{\mathrm{m}} \sin(kz) \sqrt{\langle n \rangle} .$$

5.7. Suppression of higher-order transition rates

For the solution of the quantum master equation (5.7) in Sec. 5.4 we simplified the Hamiltonian by assuming that only the energy-conserving matrix elements $\langle n | A | n+1 \rangle$ and $\langle n+1 | A^\dagger | n \rangle$ are nonzero. However, the matrix elements $\langle n | A | n+m \rangle$ are in fact nonzero for $m \neq 1$, too. In this subsection we show that there is a range of lasing parameters where the energy-nonconserving processes corresponding to these matrix elements are suppressed.

The suppression of energy-nonconserving transitions is crucial for the existence of a photon-number squeezed state. As shown in Fig. 5.6a, the roots of the matrix elements $\langle n | A | n+m \rangle$ do not coincide for different values of m. If energy-nonconserving transitions are not suppressed, the lasing process is driven across the squeezing points near the roots n_0^i of the energy-conserving coupling matrix element $\langle n | A | n+1 \rangle$: If the single-photon emission breaks down at n_0^i, the two-photon emission takes over and increases the number of photons in the resonator further. Similarly, single- and three-photon creation processes take over at the roots of the two-photon matrix element $\langle n | A | n+2 \rangle$ and the laser finally evolves into a stationary state where the photon-number expectation value is defined by the balance of the bare pumping and loss rates $\Gamma_\uparrow$, $\Gamma_\downarrow$, and κ. In general, this results in the Poissonian photon statistics of a conventional laser.
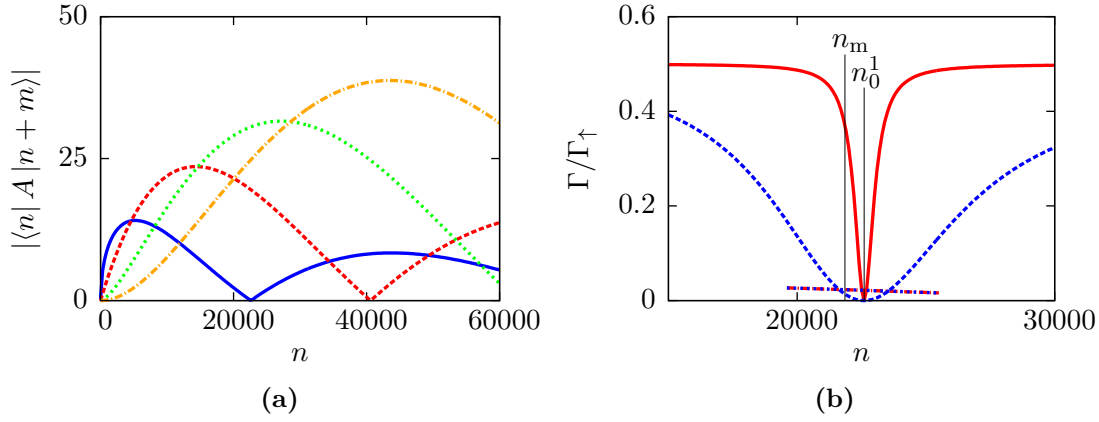
Figure 5.6.: Influence and suppression of energy-nonconserving transitions. **(a)**: Matrix elements $|\langle n| A |n + m\rangle|$ for $m = 1$ (solid blue), $m = 2$ (dashed red), $m = 3$ (dotted green), and $m = 4$ (dash-dotted orange curve). Plot parameters are $g = 0.0067\,\omega$ and $\theta = \pi/10$. **(b)**: Suppression of the two-photon transition rate $\Gamma_{n\to n+2}$ (coinciding dash-dotted red and dotted blue curves) compared to the single-photon transition rate $\Gamma_{n\to n+1}$ (solid red and dashed blue curves) at the maximum of the photon statistics, n_m, for a small bare pumping rate $\Gamma_\uparrow$ and $\theta \ll \pi/4$. Because of approximations the two-photon rates are only plotted close to the first root n_0^1 of the coupling matrix elements. The red curves correspond to the plot parameters of Fig. 5.2, i.e., $g = 0.0067\,\omega$, $\theta = \pi/10$, $\Gamma_\uparrow = 0.006\,\omega$, $\Gamma_\downarrow = 0.0001\,\omega$, $\Gamma_\varphi^* = 0.001\,\omega$, $\Delta = 0\,\omega$, $N_\mathrm{th} = 0$, and $\kappa = 1 \times 10^{-7}\,\omega$. The blue curves are calculated for ten times larger pumping rates $\Gamma_\uparrow = 0.06\,\omega$, $\Gamma_\downarrow = 0.001\,\omega$, and $\Gamma_\varphi^* = 0.01\,\omega$.

In Sec. 5.4.2 we already introduced the single-photon transition rates (5.17),

$$\Gamma_{n\to n+1} = \frac{\mathcal{A}}{1 + 2\mathcal{A}N_n} |\langle n| A |n + 1\rangle|^2 \Gamma_\uparrow \quad \text{and}$$

$$\Gamma_{n+1\to n} = \frac{\mathcal{A}}{1 + 2\mathcal{A}N_n} |\langle n| A |n + 1\rangle|^2 \Gamma_\downarrow .$$

These single-photon transition rates vanish at the roots n_0^i of the coupling matrix element $\langle n| A |n + 1\rangle$. In order to prevent the take-over of energy-nonconserving transitions, higher-order transition rates should be suppressed for all photon numbers n near n_0^i where the photon statistics $\rho(n)$ is nonzero. A complete analysis of higher-order effects for arbitrary photon numbers is only possible within a numerical solution of the master equation (5.7). However, near n_0^i the single-photon matrix elements vanish and the calculations presented in Sec. 5.4 can be performed including the two-photon transition rates. We obtain a modified version of Eq. (5.15) that is valid near n_0^i and in which the single-photon transition rates have been replaced by two-photon transition rates,

$$\frac{\mathrm{d}}{\mathrm{d}t}\rho_{n,n} = \kappa(N_\mathrm{th} + 1)(n + 1)\rho_{n+1,n+1} - \kappa N_\mathrm{th}(n + 1)\rho_{n,n}$$

$$- \kappa(N_\mathrm{th} + 1)n\rho_{n,n} + \kappa N_\mathrm{th}n\rho_{n-1,n-1}$$

$$+ \Gamma_{n+2\to n}\rho_{n+2,n+2} - \Gamma_{n\to n+2}\rho_{n,n} - \Gamma_{n\to n-2}\rho_{n,n} + \Gamma_{n-2\to n}\rho_{n-2,n-2} .$$

The structure of the two-photon transition rates is

$$\Gamma_{n\to n+2} = \frac{\mathcal{A}}{1 + 2\mathcal{A}\overline{N}_n} |\langle n| A |n + 2\rangle|^2 \Gamma_\uparrow ,$$

$$\Gamma_{n+2\to n} = \frac{\mathcal{A}}{1 + 2\mathcal{A}\overline{N}_n} |\langle n| A |n + 2\rangle|^2 \Gamma_\downarrow ,$$

where the term N_n in the denominator of the single-photon rates has been replaced by

$$\overline{N}_n = \frac{(\Delta - \omega)^2}{4g^2} \frac{\Gamma_1}{\Gamma_\varphi} + |\langle n| A |n + 2\rangle|^2 .$$

We now derive suitable values of the lasing parameters in order to suppress the two-photon transition rates. The positions n_0^i of the roots should be fixed, hence $p_0 = \frac{g}{\omega}\cos\theta$ is assumed to be constant. This allows to eliminate g, yielding

$$\Gamma_{n\to n+1} = \frac{p_0^2\omega^2\tan^2(\theta)X(n,1)}{1 + \Delta^2\Gamma_\varphi^{-2} + 2p_0^2\omega^2\tan^2(\theta)X(n,1)}\Gamma_\uparrow,$$

$$\Gamma_{n\to n+2} = \frac{p_0^4\omega^2\tan^2(\theta)X(n,2)}{1 + (\Delta - \omega)^2\Gamma_\varphi^{-2} + 2p_0^4\omega^2\tan^2(\theta)X(n,2)}\Gamma_\uparrow.$$

The term $X(n,m)$ contains all parts of the matrix elements that depend neither on θ nor on ω (note that p_0^2 is a constant),

$$X(n,m) = \frac{2}{\Gamma_1\Gamma_\varphi}m^2 4^{m-1}e^{-4p_0^2}\frac{n!}{(n+m)!}\left(L_n^m(4p_0^2)\right)^2.$$

For typical lasing parameters it holds $\Delta = 0$ and $\omega \gg \Gamma_\varphi$. This allows to simplify the rates,

$$\Gamma_{n\to n+1} = \frac{p_0^2\omega^2\tan^2(\theta)X(n,1)}{1 + 2p_0^2\omega^2\tan^2(\theta)X(n,1)}\Gamma_\uparrow,$$

$$\Gamma_{n\to n+2} = \frac{p_0^4\omega^2\tan^2(\theta)X(n,2)}{\omega^2\Gamma_\varphi^{-2} + 2p_0^4\omega^2\tan^2(\theta)X(n,2)}\Gamma_\uparrow.$$

In the limit $\theta \to \pi/2$ both rates yield

$$\lim_{\theta\to\pi/2}\Gamma_{n\to n+1} = \lim_{\theta\to\pi/2}\Gamma_{n\to n+2} = \frac{\Gamma_\uparrow}{2},$$

so there is no suppression. On the other hand, for each ω there is an angle $\theta \to 0$ such that $2p_0^2\omega^2\tan^2(\theta)X(n,1) \ll 1$ and $2p_0^4\tan^2(\theta)X(n,2) \ll \Gamma_\varphi^{-2}$ hold near n_0^i. In this limit we obtain

$$\Gamma_{n\to n+1} = p_0^2\omega^2 X(p,1)\theta^2\Gamma_\uparrow,$$

$$\Gamma_{n\to n+2} = p_0^4 X(p,1)\Gamma_\varphi\theta^2\Gamma_\uparrow = R(n)\Gamma_{n\to n+1},$$

where the prefactor $R(n)$ is given by

$$R(n) = p_0^2\left(\frac{\Gamma_\varphi}{\omega}\right)^2\frac{X(n,2)}{X(n,1)}.$$

We want p_0^2 to be constant and

$$\frac{X(n,2)}{X(n,1)} = \frac{16}{n+2}\left(\frac{L_n^2(4p_0^2)}{L_n^1(4p_0^2)}\right)^2$$

is a function of n that diverges at n_0^i and fulfills $X(n,2)/X(n,1) \lesssim 1$ for all photon numbers where $\rho(n)$ takes finite values. Therefore, the only way to suppress the prefactor $R(n)$ is to choose Γ_φ small compared to ω. The condition $\Gamma_\varphi \ll \omega$ implies small pumping rates.

Once the two-photon rates are suppressed, similar arguments are applicable to suppress three- and multi-photon rates.

In conclusion, if a secular approximation or, equivalently [43], a rotating wave approximation applies, i.e., if the rates $\Gamma_\uparrow$, $\Gamma_\downarrow$, and Γ_φ^* are much smaller than ω, higher-order transitions are suppressed and it is possible to obtain a photon-number squeezed state near a root n_0^i of the coupling matrix element $\langle n|A|n+1\rangle$.

As the suppression relies on the case $\theta \ll \pi/2$ a large σ_z coupling of the atom to the resonator is needed. Figure 5.6b illustrates the suppression of the two-photon rates for a mixing angle $\theta = \pi/10$ and two sets of lasing parameters whose pumping rates differ by one order of magnitude.

5.8. Pumping process and Lindblad superoperators in the polaron frame

In section 5.2 Lindblad superoperators in the polaron frame of the form of Eqs. (2.8) and (2.9) had been postulated. Now, a detailed derivation of these Lindblad terms is given.

5.8.1. Pumping and relaxation

An experimental realization of a pumping process needs at least a three level system. Two levels are connected by the lasing transition and the third one, $|1\rangle$, is an intermediate level for the pumping process. We discuss the following three-level pumping process:

$$\ldots \longrightarrow |{\downarrow}, n\rangle \longrightarrow |1, n\rangle \longrightarrow |{\uparrow}, n\rangle \overset{\text{lasing transition}}{\longrightarrow} |{\downarrow}, n+1\rangle \longrightarrow \ldots .$$

It increases the number of photons in the resonator in each pumping step by one.

In order to derive effective pumping rates between the two levels of the lasing transition, the third level has to be accounted for explicitly. Therefore, the initial Hamiltonian (5.2) is extended to

$$H_1' = \hbar\omega a^\dagger a + \frac{1}{2}\epsilon\sigma_z + \hbar g\Big(\cos(\theta)\sigma_z + \sin(\theta)\sigma_x \Big)\Big(a + a^\dagger \Big) + \epsilon_1 |1\rangle\langle 1| \,.$$

The energy of the intermediate pumping state $|1\rangle$ is denoted by ϵ_1. The atom couples linearly to two external bosonic baths that provide the energy for the pumping process,

$$H = H_1' + H_{1,\downarrow}^{\text{bath}} + H_{1,\uparrow}^{\text{bath}} + \hbar Q_{1,\downarrow}X_{1,\downarrow} + \hbar Q_{1,\uparrow}X_{1,\uparrow}\,,$$
$$Q_{1,\downarrow} = |1\rangle\langle{\downarrow}| + |{\downarrow}\rangle\langle 1| \,,$$
$$Q_{1,\uparrow} = |1\rangle\langle{\uparrow}| + |{\uparrow}\rangle\langle 1| \,.$$

The bath Hamiltonians $H_{1,\uparrow/\downarrow}^{\text{bath}}$ and the bath coupling operators $X_{1,\uparrow/\downarrow}$ need not be specified explicitly because they are integrated out. Only the spectral functions of the baths enter the results. Now, σ_x and σ_z are generalized Pauli matrices defined by

$$\begin{aligned} \sigma_z |{\uparrow}\rangle &= +|{\uparrow}\rangle \,, & \sigma_x |{\uparrow}\rangle &= |{\downarrow}\rangle \,, \\ \sigma_z |{\downarrow}\rangle &= -|{\downarrow}\rangle \,, & \sigma_x |{\downarrow}\rangle &= |{\uparrow}\rangle \,, \\ \sigma_z |1\rangle &= 0 \,, & \sigma_x |1\rangle &= 0 \,. \end{aligned}$$

The polaron transformation (5.4) maps H_1' to a Jaynes-Cummings-like Hamiltonian and modifies the coupling operators,

$$H_{\text{p}} = H_{1,\text{p}}' + H_{1,\downarrow}^{\text{bath}} + H_{1,\uparrow}^{\text{bath}} + \hbar O_{1,\downarrow}X_{1,\downarrow} + \hbar O_{1,\uparrow}X_{1,\uparrow}\,,$$
$$H_{1,\text{p}}' = \hbar\omega a^\dagger a + \frac{1}{2}\epsilon\sigma_z + \epsilon_1 |1\rangle\langle 1| + \hbar g\left(\sigma_+ \frac{e^{-ip}xe^{-ip}}{\hbar g} + \sigma_- \frac{e^{ip}xe^{ip}}{\hbar g} \right) + \text{const}\,,$$
$$O_{1,\downarrow} = U^\dagger Q_{1,\downarrow}U = |1\rangle\langle{\downarrow}| e^{-ip} + e^{ip} |{\downarrow}\rangle\langle 1| \,,$$
$$O_{1,\uparrow} = U^\dagger Q_{1,\uparrow}U = |1\rangle\langle{\uparrow}| e^{ip} + e^{-ip} |{\uparrow}\rangle\langle 1| \,.$$

If we replace $H_{\text{S}} = H_{1,\text{p}}'$, $H_{\text{R}} = H_{1,\downarrow}^{\text{bath}} + H_{1,\uparrow}^{\text{bath}}$, and $H_{\text{C}} = O_{1,\downarrow}X_{1,\downarrow} + O_{1,\uparrow}X_{1,\uparrow}$, the derivation of the quantum master equation outlined in Sec. 2.2 applies. By tracing out the bath degrees of freedom iteratively we obtain

$$\frac{\mathrm{d}}{\mathrm{d}t}\rho(t) = -\frac{i}{\hbar}\left[H_{1,\text{p}}', \rho(t) \right] + \sum_{O \in \{O_{1,\downarrow}, O_{1,\uparrow}\}} \left[\tilde{O}_+\rho(t)O + O\rho(t)\tilde{O}_- - O\tilde{O}_+\rho(t) - \rho(t)\tilde{O}_-O \right]\,,$$

where the operators $\tilde{O}_\pm$ are defined in Eq. (2.6).

We evaluate the operators $\tilde{O}_\pm$ in the lasing basis $|\uparrow / \downarrow /1, n\rangle$. As discussed in Sec. 5.7 a rotating wave approximation must hold in order to suppress higher-order transitions. Hence, we can exploit the relation $g \ll \omega$ and neglect the interaction term in $H'_{1,\mathrm{p}}$ for the following calculation. Then, the states of the lasing basis are eigenstates of the system and the matrix elements of the coupling operators $\tilde{O}_\pm$ are given by

$$\langle \sigma, n| \tilde{O}_\pm |\sigma', m\rangle = \int_{-\infty}^{0} \mathrm{d}\tau \; e^{i(E_{\sigma,n} - E_{\sigma',m})\tau/\hbar} \langle \sigma, n| O |\sigma', m\rangle \langle X_\mathrm{I}(0) X_\mathrm{I}(\pm\tau)\rangle_\mathrm{R}$$
$$= \frac{1}{2} S_\pm \left(\mp \frac{E_{\sigma,n} - E_{\sigma',m}}{\hbar} \right) \langle \sigma, n| O |\sigma', m\rangle \; .$$

An expansion of the coupling operators in the lasing basis yields

$$\tilde{O}_{1,\downarrow,+} = \sum_{n,m} \left[\; \frac{1}{2} S_+^{1,\downarrow} \left(-\frac{E_{1,n} - E_{\downarrow,m}}{\hbar} \right) \langle n| e^{-ip} |m\rangle |1, n\rangle \langle \downarrow, m| \right.$$
$$\left. + \frac{1}{2} S_+^{1,\downarrow} \left(\frac{E_{1,n} - E_{\downarrow,m}}{\hbar} \right) \langle m| e^{ip} |n\rangle |\downarrow, m\rangle \langle 1, n| \right] ,$$

$$\tilde{O}_{1,\downarrow,-} = \sum_{n,m} \left[\; \frac{1}{2} S_-^{1,\downarrow} \left(\frac{E_{1,n} - E_{\downarrow,m}}{\hbar} \right) \langle n| e^{-ip} |m\rangle |1, n\rangle \langle \downarrow, m| \right.$$
$$\left. + \frac{1}{2} S_-^{1,\downarrow} \left(-\frac{E_{1,n} - E_{\downarrow,m}}{\hbar} \right) \langle m| e^{ip} |n\rangle |\downarrow, m\rangle \langle 1, n| \right] ,$$

$$\tilde{O}_{1,\uparrow,+} = \sum_{n,m} \left[\; \frac{1}{2} S_+^{1,\uparrow} \left(-\frac{E_{1,n} - E_{\uparrow,m}}{\hbar} \right) \langle n| e^{ip} |m\rangle |1, n\rangle \langle \uparrow, m| \right.$$
$$\left. + \frac{1}{2} S_+^{1,\uparrow} \left(\frac{E_{1,n} - E_{\uparrow,m}}{\hbar} \right) \langle m| e^{-ip} |n\rangle |\uparrow, m\rangle \langle 1, n| \right] ,$$

$$\tilde{O}_{1,\uparrow,-} = \sum_{n,m} \left[\; \frac{1}{2} S_-^{1,\uparrow} \left(\frac{E_{1,n} - E_{\uparrow,m}}{\hbar} \right) \langle n| e^{ip} |m\rangle |1, n\rangle \langle \uparrow, m| \right.$$
$$\left. + \frac{1}{2} S_-^{1,\uparrow} \left(-\frac{E_{1,n} - E_{\uparrow,m}}{\hbar} \right) \langle m| e^{-ip} |n\rangle |\uparrow, m\rangle \langle 1, n| \right] .$$

The matrix elements $\langle n| e^{\pm ip} |m\rangle$ are nonzero for $m \neq n$ and, therefore, allow for pumping steps that create or annihilate more than one photon per step. Contrary to the lasing transition these pumping processes create or annihilate photons incoherently and they have to be suppressed by suitably chosen spectral functions of the baths.

In order to define the properties of the spectral functions, the pumping process has to be specified in more detail. We choose $\epsilon_1 > \hbar\omega/2 > 0$, i.e., the pumping process is now given by

$$\ldots \longrightarrow |\downarrow, n\rangle \stackrel{\mathrm{pumping}}{\longrightarrow} |1, n\rangle \stackrel{\mathrm{relaxation}}{\longrightarrow} |\uparrow, n\rangle \stackrel{\mathrm{lasing\ transition}}{\longrightarrow} |\downarrow, n+1\rangle \longrightarrow \ldots \; .$$

Figure 5.7a shows a sketch of the level diagram in the lasing basis. In the pumping step the energy $\epsilon_1 + \hbar\omega/2 = |-\epsilon_1 - \hbar\omega/2|$ is absorbed out of the bath $H^{1,\downarrow}$. In the relaxation step the energy $\epsilon_1 - \hbar\omega/2 > 0$ is released into the bath $H^{1,\uparrow}$. Transition energies that create or annihilate additional photons differ by an integer multiple of $\hbar\omega$. Therefore, the spectral functions of the baths have to be peaked sharply at $\pm\epsilon_1 - \hbar\omega/2$ and they have to be small at all energies differing by an integer multiple of $\hbar\omega$.
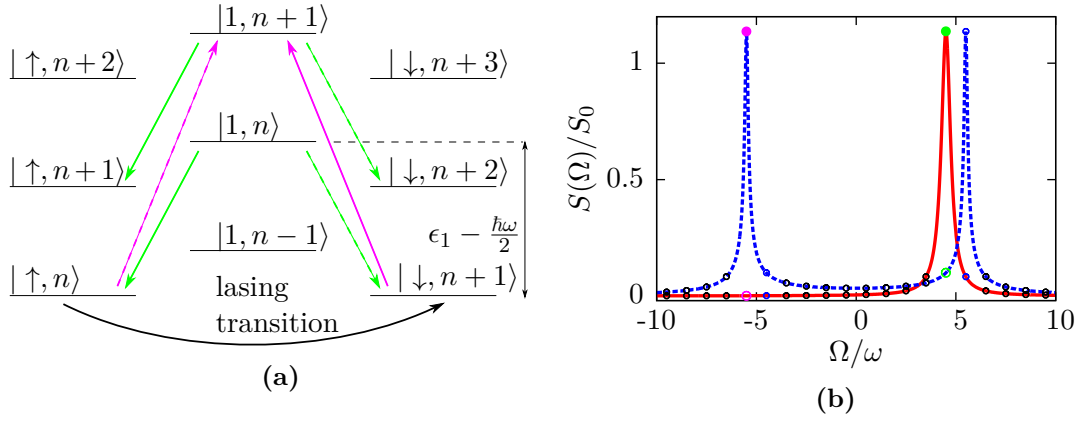
Figure 5.7.: Pumping process. **(a)**: Level diagram in the lasing basis. Green arrows indicate a release of energy into the bath $H^{1,\uparrow}$, magenta arrows indicate an absorption of energy out of the bath $H^{1,\downarrow}$. Dashed transitions have to be suppressed by the spectral functions of the baths. **(b)**: Spectral functions $S^{1,\uparrow}$ (solid red) and $S^{1,\downarrow}$ (dashed blue) of the baths. A positive frequency $\Omega > 0$ corresponds to a release of energy into the bath, $\Omega < 0$ corresponds to an absorption out of the bath. Solid and open circles indicate desired and suppressed transitions, respectively. The transitions of the pumping process are marked in green and magenta. Black circles correspond to undesired higher-order processes and blue circles indicate transitions of the inverse pumping process. The plot parameters are $\epsilon_1 = 5\,\omega$, $\gamma' = 0.28\,\omega$, and $\gamma = 0.08\,\omega$.

Figure 5.7b demonstrates that these conditions can be fulfilled by a spectral function of a harmonic oscillator at infinite temperature for the pumping bath and by a Lorentzian spectral function for the absorption bath,

$$
S^{1,\downarrow}(\Omega) = S_{\text{pump}}(\Omega) = \frac{S_0}{\sqrt{(\Omega^2 - \omega_{\text{r}}^2)^2 + 4\gamma^2\Omega^2}} \,,
$$

$$
S^{1,\uparrow}(\Omega) = S_{\text{relax}}(\Omega) = \frac{S_0'}{\pi} \frac{\gamma'}{(\Omega - \omega_{\text{r}})^2 + \gamma'^2} \,.
$$

Alternatively, a harmonic oscillator at zero temperature could be used for the relaxation bath. The spectral functions $S^{1,\uparrow}$ and $S^{1,\downarrow}$ have their resonance peaks at $\omega_{\text{r}} = \epsilon_1 - \hbar\omega/2$ and $\omega_{\text{r}} = -\epsilon_1 - \hbar\omega/2$, respectively. If the width parameters fulfill $\gamma, \gamma' \approx 0.1\,\omega_{\text{r}}$, the spectral functions drop fast enough to suppress all undesired transitions. An experimental setup providing a Lorentzian spectral function has been demonstrated recently [9].

Based on these assumptions, the spectral functions are rewritten as follows:

$$
S_\pm^{1,\downarrow}\left(\mp\frac{E_{1,n} - E_{\downarrow,m}}{\hbar}\right) = S_\pm^{1,\downarrow}(\mp\omega_{1,\downarrow})\delta_{n,m} \,,
$$

$$
S_\pm^{1,\uparrow}\left(\mp\frac{E_{1,n} - E_{\uparrow,m}}{\hbar}\right) = S_\pm^{1,\uparrow}(\mp\omega_{1,\uparrow})\delta_{n,m} \,,
$$

where $\hbar\omega_{1,\downarrow/\uparrow} = E_{1,n} - E_{\downarrow/\uparrow,n}$. Now, we separate the terms of the Bloch-Redfield master equation into those which connect diagonal elements of ρ to either diagonal or resonant

off-diagonal matrix elements of ρ, and all other terms,

$$
\begin{aligned}
\frac{\mathrm{d}}{\mathrm{d}t}\rho =& -\frac{i}{\hbar}\left[H'_{1,\mathrm{p}},\rho\right] \\
&+\sum_n \Bigg[\quad S^{1,\downarrow}(-\omega_{1,\downarrow})\left|\langle n|e^{-ip}|n\rangle\right|^2 \cdot |1,n\rangle\langle\downarrow,n|\rho|\downarrow,n\rangle\langle 1,n| \\
&\qquad +S^{1,\downarrow}(\omega_{1,\downarrow})\left|\langle n|e^{ip}|n\rangle\right|^2 \cdot |\downarrow,n\rangle\langle 1,n|\rho|1,n\rangle\langle\downarrow,n| \\
&\qquad -\left|\langle n|e^{-ip}|n\rangle\right|^2 \cdot \left(\frac{1}{2}S^{1,\downarrow}_+(-\omega_{1,\downarrow})|\downarrow,n\rangle\langle\downarrow,n|\rho+\frac{1}{2}S^{1,\downarrow}_-(-\omega_{1,\downarrow})\rho|\downarrow,n\rangle\langle\downarrow,n|\right) \\
&\qquad -\left|\langle n|e^{ip}|n\rangle\right|^2 \cdot \left(\frac{1}{2}S^{1,\downarrow}_+(\omega_{1,\downarrow})|1,n\rangle\langle 1,n|\rho+\frac{1}{2}S^{1,\downarrow}_-(\omega_{1,\downarrow})\rho|1,n\rangle\langle 1,n|\right)\Bigg] \\
&+\sum_n \Bigg[\quad S^{1,\uparrow}(-\omega_{1,\uparrow})\left|\langle n|e^{ip}|n\rangle\right|^2 \cdot |1,n\rangle\langle\uparrow,n|\rho|\uparrow,n\rangle\langle 1,n| \\
&\qquad +S^{1,\uparrow}(\omega_{1,\uparrow})\left|\langle n|e^{-ip}|n\rangle\right|^2 \cdot |\uparrow,n\rangle\langle 1,n|\rho|1,n\rangle\langle\uparrow,n| \\
&\qquad -\left|\langle n|e^{ip}|n\rangle\right|^2 \cdot \left(\frac{1}{2}S^{1,\uparrow}_+(-\omega_{1,\uparrow})|\uparrow,n\rangle\langle\uparrow,n|\rho+\frac{1}{2}S^{1,\uparrow}_-(-\omega_{1,\uparrow})\rho|\uparrow,n\rangle\langle\uparrow,n|\right) \\
&\qquad -\left|\langle n|e^{-ip}|n\rangle\right|^2 \cdot \left(\frac{1}{2}S^{1,\uparrow}_+(\omega_{1,\uparrow})|1,n\rangle\langle 1,n|\rho+\frac{1}{2}S^{1,\uparrow}_-(\omega_{1,\uparrow})\rho|1,n\rangle\langle 1,n|\right)\Bigg] \\
&+ \text{terms connecting to non-resonant off-diagonal matrix elements}\,.
\end{aligned}
$$

All terms connecting diagonal matrix elements to non-resonant off-diagonal matrix elements are neglected within a secular approximation. To justify this, we note that all rates in this master equation are of the same order of magnitude, given by the product of a spectral function and two matrix elements,

$$
\frac{1}{2}S^{1,\uparrow/\downarrow}_\pm(\pm\omega_{1,\uparrow/\downarrow})\langle n|e^{ip}|n\rangle\langle n'|e^{-ip}|m'\rangle\,.
$$

As it turns out below, the rates connecting diagonal elements to themselves are proportional to the bare pumping and relaxation rates $\Gamma_\uparrow$ and $\Gamma_\downarrow$. In Sec. 5.7 we demanded the condition $\Gamma_\uparrow,\Gamma_\downarrow,\Gamma^*_\varphi \ll \omega$ for the suppression of higher-order lasing transitions. Hence, all rates in the above master equation are much smaller than ω and all rates to non-resonant off-diagonal matrix elements can be neglected using a secular approximation.

The terms in big round brackets are simplified using the relations (2.7a) and (2.7b), yielding

$$
\begin{aligned}
&\frac{1}{2}S^{1,\downarrow}_+(-\omega_{1,\downarrow})|\downarrow,n\rangle\langle\downarrow,n|\rho+\frac{1}{2}S^{1,\downarrow}_-(-\omega_{1,\downarrow})\rho|\downarrow,n\rangle\langle\downarrow,n| \\
&\quad=\frac{S^{1,\downarrow}(-\omega_{1,\downarrow})}{2}\left(|\downarrow,n\rangle\langle\downarrow,n|\rho+\rho|\downarrow,n\rangle\langle\downarrow,n|\right)+i\mathcal{P}\int\frac{\mathrm{d}\Omega}{2\pi}\,\frac{S^{1,\downarrow}(\Omega)}{-\omega_{1,\downarrow}-\Omega}\left[|\downarrow,n\rangle\langle\downarrow,n|,\rho\right]\,, \\
&\frac{1}{2}S^{1,\downarrow}_+(\omega_{1,\downarrow})|1,n\rangle\langle 1,n|\rho+\frac{1}{2}S^{1,\downarrow}_-(\omega_{1,\downarrow})\rho|1,n\rangle\langle 1,n| \\
&\quad=\frac{S^{1,\downarrow}(\omega_{1,\downarrow})}{2}\left(|1,n\rangle\langle 1,n|\rho+\rho|1,n\rangle\langle 1,n|\right)+i\mathcal{P}\int\frac{\mathrm{d}\Omega}{2\pi}\,\frac{S^{1,\downarrow}(\Omega)}{\omega_{1,\downarrow}-\Omega}\left[|1,n\rangle\langle 1,n|,\rho\right]\,,
\end{aligned}
$$

and similar for the terms emerging from $O_{1,\uparrow}$. The terms involving the Cauchy principle value integral $\mathcal{P}\int\mathrm{d}\Omega$ are an energy renormalization and the remaining terms have the

usual form of a Lindblad superoperator,

$$
\begin{aligned}
\dot{\rho} = &-\frac{i}{\hbar}\left[H'_{1,\mathrm{p}}, \rho\right] \\
&+ \sum_n \Bigg[\; \frac{\Gamma_{\downarrow,n\to 1,n}}{2}\left(2\left|1,n\right\rangle\left\langle\downarrow,n\right|\rho\left|\downarrow,n\right\rangle\left\langle 1,n\right| - \left|\downarrow,n\right\rangle\left\langle\downarrow,n\right|\rho - \rho\left|\downarrow,n\right\rangle\left\langle\downarrow,n\right|\right) \\
&+ \frac{\Gamma_{1,n\to\downarrow,n}}{2}\left(2\left|\downarrow,n\right\rangle\left\langle 1,n\right|\rho\left|1,n\right\rangle\left\langle\downarrow,n\right| - \left|1,n\right\rangle\left\langle 1,n\right|\rho - \rho\left|1,n\right\rangle\left\langle 1,n\right|\right) \\
&+ \frac{\Gamma_{\uparrow,n\to 1,n}}{2}\left(2\left|1,n\right\rangle\left\langle\uparrow,n\right|\rho\left|\uparrow,n\right\rangle\left\langle 1,n\right| - \left|\uparrow,n\right\rangle\left\langle\uparrow,n\right|\rho - \rho\left|\uparrow,n\right\rangle\left\langle\uparrow,n\right|\right) \\
&+ \frac{\Gamma_{1,n\to\uparrow,n}}{2}\left(2\left|\uparrow,n\right\rangle\left\langle 1,n\right|\rho\left|1,n\right\rangle\left\langle\uparrow,n\right| - \left|1,n\right\rangle\left\langle 1,n\right|\rho - \rho\left|1,n\right\rangle\left\langle 1,n\right|\right) \Bigg] ,
\end{aligned}
$$

where the rates are defined as follows:

$$
\Gamma_{\downarrow,n\to 1,n} = S^{1,\downarrow}(-\omega_{1,\downarrow})\left|\left\langle n\right|e^{-ip}\left|n\right\rangle\right|^2 , \qquad \Gamma_{\uparrow,n\to 1,n} = S^{1,\uparrow}(-\omega_{1,\uparrow})\left|\left\langle n\right|e^{ip}\left|n\right\rangle\right|^2 ,
$$

$$
\Gamma_{1,n\to\downarrow,n} = S^{1,\downarrow}(\omega_{1,\downarrow})\left|\left\langle n\right|e^{-ip}\left|n\right\rangle\right|^2 , \qquad \Gamma_{1,n\to\uparrow,n} = S^{1,\uparrow}(\omega_{1,\uparrow})\left|\left\langle n\right|e^{ip}\left|n\right\rangle\right|^2 .
$$

Finally, the intermediate pumping state is eliminated and effective rates between the upper and the lower lasing state are calculated. If the population of the intermediate pumping state does not change, $\dot{\rho}_{1,n;1,n} = 0$, effective rates are given by

$$
\Gamma_\uparrow = \Gamma_{\downarrow,n\to\uparrow,n} = \frac{\Gamma_{\downarrow,n\to 1,n}\Gamma_{1,n\to\uparrow,n}}{\Gamma_{\downarrow,n\to 1,n} + \Gamma_{1,n\to\uparrow,n}} = \frac{S^{1,\downarrow}(-\omega_{1,\downarrow})S^{1,\uparrow}(\omega_{1,\uparrow})}{S^{1,\downarrow}(-\omega_{1,\downarrow}) + S^{1,\uparrow}(\omega_{1,\uparrow})}\left|\left\langle n\right|e^{ip}\left|n\right\rangle\right|^2 , \quad (5.27a)
$$

$$
\Gamma_\downarrow = \Gamma_{\uparrow,n\to\downarrow,n} = \frac{\Gamma_{\uparrow,n\to 1,n}\Gamma_{1,n\to\downarrow,n}}{\Gamma_{\uparrow,n\to 1,n} + \Gamma_{1,n\to\downarrow,n}} \approx 0 . \qquad (5.27b)
$$

The rate $\Gamma_\downarrow$ vanishes because the single-peaked spectral function $S^{1,\uparrow}$ suppresses the transition rate $\Gamma_{\uparrow,n\to 1,n} \approx 0$. The matrix elements $\left\langle n\right|e^{ip}\left|n\right\rangle$ have roots at certain photon numbers $n_0^{i\,\prime}$, but the first root of $\left\langle n\right|e^{ip}\left|n\right\rangle$ is situated at a larger photon number than the first root of $\left\langle n\right|A\left|n+1\right\rangle$. Therefore, the pumping process allows to reach at least the first root of the coupling matrix element $\left\langle n\right|A\left|n+1\right\rangle$ and a photon-number squeezed state can be established, there.

In conclusion, pumping and relaxation processes can be modeled in the polaron frame by a Lindblad superoperator as given by the first line of Eq. (2.9). Pure dephasing is covered in the next subsection.

5.8.2. Pure dephasing

Pure dephasing is modeled with a σ_z coupling to the external bath,

$$
H = H_1 + H_{\mathrm{pd}}^{\mathrm{bath}} + \hbar Q_{\mathrm{pd}}X_{\mathrm{pd}} ,
$$

$$
Q_{\mathrm{pd}} = \sigma_z .
$$

The coupling operator Q_{pd} is invariant under a polaron transformation so that the transformed system is given by

$$
H_{\mathrm{p}} = H_{1,\mathrm{p}} + H_{\mathrm{pd}}^{\mathrm{bath}} + \hbar O_{\mathrm{pd}}X_{\mathrm{pd}} ,
$$

$$
O_{\mathrm{pd}} = \sigma_z .
$$

Again, the derivation of the master equation outlined in Sec. 2.2 is used by replacing $H_\mathrm{S} = H'_{1,\mathrm{p}}$, $H_\mathrm{R} = H^\mathrm{bath}_\mathrm{pd}$, and $H_\mathrm{C} = O_\mathrm{pd}X_\mathrm{pd}$. The Bloch-Redfield form of the master equation is now

$$\frac{\mathrm{d}}{\mathrm{d}t}\rho(t) = -\frac{i}{\hbar}\left[H'_{1,\mathrm{p}}, \rho(t)\right]$$
$$+ \left[\tilde{O}_{\mathrm{pd},+}\rho(t)O_\mathrm{pd} + O_\mathrm{pd}\rho(t)\tilde{O}_{\mathrm{pd},-} - O_\mathrm{pd}\tilde{O}_{\mathrm{pd},+}\rho(t) - \rho(t)\tilde{O}_{\mathrm{pd},-}O_\mathrm{pd}\right],$$
$$\tilde{O}_{\mathrm{pd},\pm} = \frac{1}{2}S^\mathrm{pd}_\pm(0)O_\mathrm{pd}.$$

We find that the Bloch-Redfield master equation is given by

$$\frac{\mathrm{d}}{\mathrm{d}t}\rho(t) = -\frac{i}{\hbar}\left[H'_{1,\mathrm{p}}, \rho(t)\right] + S^\mathrm{pd}(0)\left(\sigma_z\rho\sigma_z - \rho\right),$$

which corresponds to the standard form of a Lindblad superoperator for pure dephasing with a pure-dephasing rate $\Gamma^*_\varphi = 2S^\mathrm{pd}(0)$. Combining this with the result of the previous subsection we find that the atomic Lindblad superoperator describing pumping, relaxation, and dephasing in the polaron frame is given by Eq. (2.9).

5.8.3. Resonator decay

Resonator decay is modeled using the following coupling to an external bath:

$$H = H_1 + H^\mathrm{bath}_\mathrm{res} + \hbar Q_\mathrm{res}X_\mathrm{res},$$
$$Q_\mathrm{res} = a + a^\dagger.$$

The polaron transformed Hamiltonian is given by

$$H_\mathrm{p} = H_{1,\mathrm{p}} + H^\mathrm{bath}_\mathrm{res} + \hbar O_\mathrm{res}X_\mathrm{res},$$
$$O_\mathrm{res} = a + a^\dagger - 2p_0\sigma_z.$$

The Bloch-Redfield form of the master equation is

$$\frac{\mathrm{d}}{\mathrm{d}t}\rho(t) = -\frac{i}{\hbar}\left[H'_{1,\mathrm{p}}, \rho(t)\right]$$
$$+ \left[\tilde{O}_{\mathrm{res},+}\rho(t)O_\mathrm{res} + O_\mathrm{res}\rho(t)\tilde{O}_{\mathrm{res},-} - O_\mathrm{res}\tilde{O}_{\mathrm{res},+}\rho(t) - \rho(t)\tilde{O}_{\mathrm{res},-}O_\mathrm{res}\right],$$
$$\tilde{O}_{\mathrm{res},\pm} = \frac{1}{2}S^\mathrm{res}_\pm(\pm\omega)a + \frac{1}{2}S^\mathrm{res}_\pm(\mp\omega)a^\dagger - S^\mathrm{res}_\pm(0)p_0\sigma_z.$$

Similar to the derivation of the Lindblad superoperator for pumping and relaxation, the terms in the Bloch-Redfield master equation are separated into those which connect diagonal matrix elements or resonant off-diagonal matrix elements to other diagonal or resonant off-diagonal matrix elements, and all other terms. Again, all rates in the master equation are of the same order of magnitude and a secular approximation holds because of the condition $\kappa \ll \omega$. Therefore, all terms that do not connect diagonal matrix elements or resonant off-diagonal matrix elements to similar terms are neglected in the Bloch-Redfield master equation. The remaining terms can be rewritten as follows:

$$\tilde{O}_{\mathrm{res},+}\rho O_\mathrm{res} + O_\mathrm{res}\rho\tilde{O}_{\mathrm{res},-} - O_\mathrm{res}\tilde{O}_{\mathrm{res},+}\rho - \rho\tilde{O}_{\mathrm{res},-}O_\mathrm{res}$$
$$= S^\mathrm{res}(-\omega)\left(a^\dagger\rho a - \frac{1}{2}\left(aa^\dagger\rho + \rho aa^\dagger\right)\right) + S^\mathrm{res}(\omega)\left(a\rho a^\dagger - \frac{1}{2}\left(a^\dagger a\rho + \rho a^\dagger a\right)\right)$$
$$+ 4p_0^2 S^\mathrm{res}(0)\left(\sigma_z\rho\sigma_z - \rho\right) + i\mathcal{P}\int_0^\infty \frac{\mathrm{d}\Omega}{2\pi}\left(\frac{S^\mathrm{res}(\Omega)}{\omega + \Omega} - \frac{S^\mathrm{res}(\Omega)}{\omega - \Omega}\right)\left[a^\dagger a, \rho\right].$$
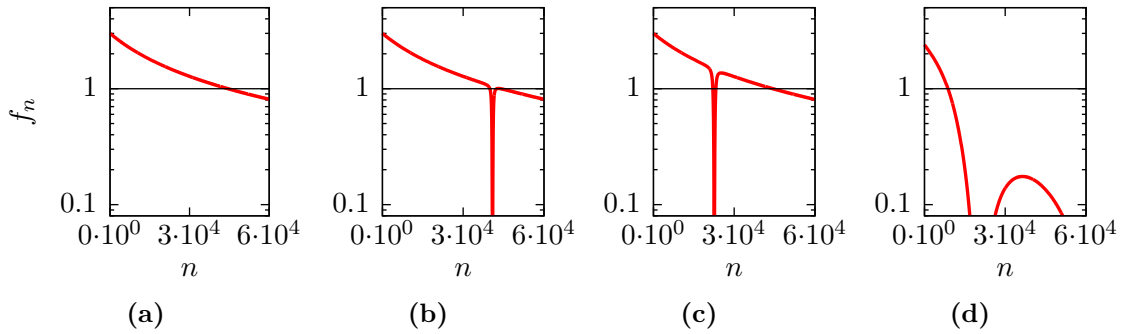
Figure 5.8.: Influence of the mixing angle θ on squeezing. The plots correspond to the four cases discussed in Sec. 5.9. **(a):** $\theta = \pi/2$, $n_0^1 \gg n_{\mathrm{max}}^{\mathrm{cl}}$, $F = 1$. **(b):** $\theta = \pi/4$, $n_{\mathrm{m}} < n_0^1 < n_{\mathrm{max}}^{\mathrm{cl}}$, $F = 0.16$ but higher-order rates are not suppressed and drive the system across the squeezed state. **(c):** $\theta = \pi/10$, $n_{\mathrm{m}} < n_0^1 < n_{\mathrm{max}}^{\mathrm{cl}}$, $F = 0.04$, squeezed light is produced. **(d):** $\theta = \pi/500$, $F = 0.75$, the recursion coefficient decreases because of $f_n \propto \theta$ and the steepness of the slope at n_{m} decreases. Therefore, the Fano factor increases again. Plot parameters are $g = 0.0067\,\omega$, $\Delta = 0\,\omega$, $\kappa = 4.5 \times 10^{-8}\,\omega$, $M = 1$, and $N_{\mathrm{th}} = 0$.

The last term is a renormalization of the resonator frequency that can be absorbed into the system Hamiltonian. The first line on the right-hand side is the standard form of a Lindblad superoperator for resonator relaxation. The spectral functions are given by $S^{\mathrm{res}}(-\omega) = \kappa N_{\mathrm{th}}$ and $S^{\mathrm{res}}(\omega) = \kappa(N_{\mathrm{th}} + 1)$. Because of the additional σ_z coupling arising form the polaron transformation, the bath $H_{\mathrm{res}}^{\mathrm{bath}}$ has an influence on atomic pure dephasing, which is the first term on the second line. This effect can be absorbed into the pure dephasing rate Γ_φ^* in the atomic Lindblad superoperator.

In conclusion, pumping, dephasing, and relaxation processes for the atom and the resonator are modeled by standard Lindblad superoperators even after a polaron transformation. The rates $\Gamma_\uparrow$, $\Gamma_\downarrow$ and Γ_φ^* are effective rates, given by Eqs. (5.27a), (5.27b), and

$$\Gamma_\varphi^* = 2\left(S^{\mathrm{pd}}(0) + 4p_0^2 S^{\mathrm{res}}(0)\right) .$$

5.9. Influence of the mixing angle on squeezing

In Secs. 5.4 and 5.5 we showed that the creation of a photon-number squeezed state relies on the roots of the coupling matrix element $\langle n | A | n+1 \rangle$ and, therefore, on the presence of a σ_z coupling to the radiation field. In this section we discuss the influence of the mixing angle θ on squeezing and find that only mixing angles $0 < \theta \ll \pi/4$ actually allow for squeezing.

The polaron transformation is a nontrivial unitary transformation for $0 \leq \theta < \pi/2$. For any mixing angle θ in this range the coupling matrix element $\langle n | A | n+1 \rangle$ has roots at certain photon numbers n_0^i. However, in order to get photon-number squeezed light the position of one of these roots, e.g., the first one, n_0^1, must be smaller than the photon number $n_{\mathrm{max}}^{\mathrm{cl}}$ of the maximum of the photon statistics of a conventional laser with pure σ_x couplings. The conventional photon number $n_{\mathrm{max}}^{\mathrm{cl}}$ is defined by the balance of the bare pumping and loss rates in the system.

For $\theta \approx \pi/2$, i.e, pure σ_x coupling, p_0 tends to zero and, therefore, the position of the first root of the coupling matrix element tends to infinity. Hence, the first root is situated beyond the photon number $n_{\mathrm{max}}^{\mathrm{cl}}$ of a conventional laser, $n_0^1 \gg n_{\mathrm{max}}^{\mathrm{cl}}$, and squeezing is not possible for any set of realistic lasing parameters (Fig 5.8a). Instead, a Poissonian photon statistics is observed with a photon-number expectation value $\langle n \rangle \approx n_{\mathrm{max}}^{\mathrm{cl}}$.

For $\pi/4 \lesssim \theta < \pi/2$, we may find a root of the coupling matrix element at a photon number smaller than $n_{\mathrm{max}}^{\mathrm{cl}}$, $n_0^1 < n_{\mathrm{max}}^{\mathrm{cl}}$, by a suitable choice of lasing parameters. Then, a local maximum of the photon distribution $n_{\mathrm{m}} \approx n_0^1 < n_{\mathrm{max}}^{\mathrm{cl}}$ exists that allows in principle for a photon-number squeezed state. However, in this range of the mixing angle higher-order transition rates are not suppressed and they will drive the system across the root of the coupling at n_0^1. The squeezed state cannot establish and the laser produces light with a Poissonian statistics at the photon-number expectation value of a conventional laser, $\langle n \rangle \approx n_{\mathrm{m}}^{\mathrm{cl}}$ (Fig. 5.8b).

For $0 < \theta \ll \pi/4$ we still can satisfy the condition $n_{\mathrm{m}} \approx n_0^1 < n_{\mathrm{max}}^{\mathrm{cl}}$ and, now, higher order rates are suppressed. Therefore, a photon-number squeezed state can be realized with an average photon number $\langle n \rangle \approx n_0^1$ (Fig. 5.8c).

For very small mixing angles $\theta \to 0$, i.e., almost pure σ_z coupling, the coupling matrix elements are proportional to θ as shown by Eq. (5.10). Hence, for sufficiently small θ the recursion coefficient is given by the approximation (5.20) for all photon numbers n. By combining this with Eq. (5.10) we obtain a linear scaling of the recursion coefficient f_n with the mixing angle,

$$f_n \propto \frac{\theta}{\kappa n} \ .$$

If the recursion coefficient f_n tends to zero, the position of the maximum of the photon distribution, n_{m}, decreases. On the other hand, the position of the first root, n_0^1, is bounded from below by $n_0^{\mathrm{min}} = \lim_{\theta \to 0} p_0^2 = \frac{g}{\omega}$. Therefore, for sufficiently small mixing angles θ we have $n_{\mathrm{m}} < n_0^{\mathrm{min}}$. As shown in Fig. 5.8d the slope of the recursion coefficient f_n at the photon number n_{m} decreases. Therefore, the Fano factor increases and the laser intensity decreases for a very small mixing angle $\theta \to 0$.

In conclusion, squeezed light is created for a mixing angle in the range $0 < \theta \ll \pi/4$ and there is a trade-off between a good suppression of higher-order transitions, which demands a small mixing angle θ, and a sufficient coupling between atom and resonator, which relies on a not too small mixing angle θ.

5.10. Multi-atom lasing setups

5.10.1. Polaron transformation and mean-field Hamiltonian

In this section we generalize the results obtained so far to a multi-atom lasing Hamiltonian. We consider M identical atoms, i.e., the generalized lasing Hamiltonian (5.1) takes now the following form,

$$H_M = \hbar\omega a^\dagger a + \sum_{j=1}^{M} \frac{1}{2}\epsilon\sigma_z^j + \sum_{j=1}^{M} \hbar g \left(\cos(\theta)\sigma_z^j + \sin(\theta)\sigma_x^j \right) \left(a^\dagger + a \right) \ .$$

The polaron transformation (5.4) is generalized to M atoms as well,

$$U = \exp\left[ip \sum_{j=1}^{M} \sigma_z^j \right] \ ,$$

where the quantity p is still given by Eq. (5.3b). A polaron transformation of the Hamiltonian H_M yields (cf. Appendix B.1)

$$H = \hbar\omega a^\dagger a + \sum_{j=1}^{M} \frac{1}{2}\epsilon\sigma_z^j + \sum_{j=1}^{M} \left(\sigma_+^j e^{-ip} x e^{-ip} + \sigma_-^j e^{ip} x e^{ip}\right)$$
$$- 2\hbar\frac{g^2}{\omega}\sin(\theta)\cos(\theta)\sum_{j\neq l=1}^{M}\left(\sigma_+^j\sigma_z^l e^{-2ip} + \sigma_-^j\sigma_z^l e^{2ip}\right) \tag{5.28}$$
$$- \hbar\frac{g^2}{\omega}\cos^2(\theta)M - \hbar\frac{g^2}{\omega}\cos^2(\theta)\sum_{j\neq l=1}^{M}\sigma_z^l\sigma_z^j\,.$$

Two new terms arise because of the polaron transformation: First, there are couplings between the atoms that depend on the lasing activity, $\sigma_\pm^j\sigma_z^l e^{\mp 2ip}$. Second, there are correlations between the atoms, $\sigma_z^j\sigma_z^l$. In order to obtain an effective Hamiltonian of M independent atoms coupled to a common resonator a mean-field approximation is performed by rewriting

$$\sigma_z^l\sigma_z^j \approx \sigma_z^l\left\langle\sigma_z^j\right\rangle + \left\langle\sigma_z^l\right\rangle\sigma_z^j - \left\langle\sigma_z^l\right\rangle\left\langle\sigma_z^j\right\rangle\,, \tag{5.29a}$$
$$\sigma_\pm^i\sigma_z^j \approx \sigma_\pm^i\left\langle\sigma_z^j\right\rangle + \left\langle\sigma_\pm^i\right\rangle\sigma_z^j - \left\langle\sigma_\pm^i\right\rangle\left\langle\sigma_z^j\right\rangle = \sigma_\pm^i\left\langle\sigma_z^j\right\rangle\,. \tag{5.29b}$$

In the last step we used that only energy-conserving matrix elements of ρ are nonzero.

Introducing the sum of all atomic polarizations except of the one of atom j itself,

$$S_z^j = \sum_{\substack{i\neq j \\ i=1}}^{M}\left\langle\sigma_z^i\right\rangle\,, \tag{5.30}$$

the Hamiltonian (5.28) can be rewritten as follows,

$$H_{\text{MF}} = \hbar\omega a^\dagger a + \sum_{j=1}^{M}\frac{1}{2}E(S_z^j)\sigma_z^j + \sum_{j=1}^{M}\hbar g\left(\sigma_+^j A(S_z^j) + \sigma_-^j A^\dagger(S_z^j)\right) + c\,, \tag{5.31}$$

with a modified level splitting energy $E(S_z^j)$, modified field operators $A^{(\dagger)}(S_z^j)$, and an irrelevant constant energy shift given by

$$E(S_z^j) = \epsilon - 4\hbar\omega p_0^2 S_z^j\,, \tag{5.32a}$$
$$A(S_z^j) = \frac{e^{-ip} x e^{-ip}}{\hbar g} - \frac{2}{\hbar g}x_0 p_0 S_z^j e^{-2ip}\,, \tag{5.32b}$$
$$c = -\hbar\omega p_0^2 M + \hbar\omega p_0^2 \sum_{j\neq l=1}^{M}\left\langle\sigma_z^l\right\rangle\left\langle\sigma_z^j\right\rangle\,. \tag{5.32c}$$

The quantity S_z^j needs to be determined self-consistently.

Both terms in the matrix elements $\langle n| A^{(\dagger)}(S_z^j) |n+m\rangle$ are proportional to the operator e^{-2ip} and, therefore, using Eqs. (5.8) and (5.9) the coupling matrix elements can be rewritten as follows:

$$\langle n| A(S_z^j) |n+m\rangle = -\left(\frac{1}{\hbar g}\frac{m}{2}\frac{x_0}{p_0} + \frac{2}{\hbar g}x_0 p_0 S_z^j\right)T_{n,m}^-\,, \tag{5.33a}$$
$$\langle n| A^\dagger(S_z^j) |n+m\rangle = +\left(\frac{1}{\hbar g}\frac{m}{2}\frac{x_0}{p_0} - \frac{2}{\hbar g}x_0 p_0 S_z^j\right)T_{n,m}^+\,. \tag{5.33b}$$

The position of the roots is determined only by $T_{n,m}^{\pm}$ and does not depend on S_z^j. Hence, the single-atom laser and the multi-atom laser have roots of the coupling matrix elements at the same photon numbers n_0^i. However, the amplitude of the matrix elements contains a term that scales linearly with S_z^j, i.e., in the multi-atom lasing setup the effective coupling strength of each atom to the radiation field is increased. This increase of the effective coupling strength is different from the collective renormalization by a factor of $\sqrt{M}$ found in Sec. 4.3 because S_z^j scales linearly with M. The scaling behavior follows from the definition (5.30) and is explicitly derived in Sec. 5.10.3.

5.10.2. Quantum master equation and photon statistics

The single-atom quantum master equation in the polaron frame, Eq. (5.7), is now generalized to M atoms:

$$\frac{\mathrm{d}}{\mathrm{d}t}\rho = -\frac{i}{\hbar}\left[H_{\mathrm{MF}},\rho\right] + L_{\mathrm{R}}\rho + \sum_{j=1}^{M} L_{\mathrm{Q,j}}\rho\,. \tag{5.34}$$

Here ρ is the density matrix describing M two-level atoms and the resonator. The derivation of the Lindblad superoperators in the polaron frame shown in Sec. 5.8 holds for multi-atom lasing setups as well. By L_{R} we denote the usual Lindblad superoperator for the resonator introduced in Eq. (2.8), and $L_{\mathrm{Q},j}$ is an atomic Lindblad superoperator as given in Eq. (2.9), which describes the pumping, relaxation and dephasing of atom j. Hence, all Pauli matrices in $L_{\mathrm{Q},j}$ act only on atom j. As all atoms are assumed to be identical, the pumping, relaxation and dephasing rates $\Gamma_\uparrow$, $\Gamma_\downarrow$ and Γ_φ^* are the same for all M atoms.

Similar to the single-atom case the atomic states are traced out in order to obtain the reduced density matrix of the resonator,

$$\frac{\mathrm{d}}{\mathrm{d}t}\rho^{\mathrm{res}} = -i\omega\left[a^\dagger a, \rho^{\mathrm{res}}\right] - ig\sum_{j=1}^{M} \mathrm{Tr}_{\mathrm{atom}\ j}\left(\left[\sigma_+^j A(S_z^j) + \sigma_-^j A^\dagger(S_z^j), \rho^{j,\mathrm{res}}\right]\right) + L_{\mathrm{R}}\rho^{\mathrm{res}}\,.$$

Here $\rho^{j,\mathrm{res}}$ represents a reduced density matrix describing the dynamics of atom j and the resonator. Analogous to the single-atom case the interaction term still couples the reduced density matrix of the resonator, ρ^{res}, to the density matrix $\rho^{j,\mathrm{res}}$ that also accounts for the dynamics of the atom j. As we assume all atoms to be identical it is sufficient to calculate the reduced density matrix $\rho^{k,\mathrm{res}}$ for one arbitrarily chosen atom k. Similar to the single-atom laser we are left with

$$\frac{\mathrm{d}}{\mathrm{d}t}\rho^{\mathrm{res}} = -i\omega\left[a^\dagger a, \rho^{\mathrm{res}}\right] - igM\,\mathrm{Tr}_{\mathrm{atom}\ k}\left(\left[\sigma_+^k A(S_z^k) + \sigma_-^k A^\dagger(S_z^k), \rho^{k,\mathrm{res}}\right]\right) + L_{\mathrm{R}}\rho^{\mathrm{res}}\,, \tag{5.35a}$$

$$\frac{\mathrm{d}}{\mathrm{d}t}\rho^{k,\mathrm{res}} = -\frac{i}{\hbar}\left[\hbar\omega a^\dagger a + \frac{1}{2}E(S_z^k)\sigma_z^k + \hbar g\left(\sigma_+^k A(S_z^k) + \sigma_- A^\dagger(S_z^k)\right), \rho^{k,\mathrm{res}}\right] + L_{\mathrm{Q},k}\rho^{k,\mathrm{res}}\,. \tag{5.35b}$$

Details on the derivation are given in the Appendix C. Like for the single-atom case the resonator Lindblad term $L_{\mathrm{R}}\rho$ has been eliminated from equation (5.35b) using an adiabatic approximation. This system of coupled differential equations has the same structure as the corresponding system in the single-atom case, Eq. (5.12), but the effective coupling strength in equation (5.35a) has been increased by a factor of M originating from the sum over all atoms.

The matrix elements $\rho_{\uparrow,n;\downarrow,n+1}^{k,\mathrm{res}}$ and $\rho_{\downarrow,n+1;\uparrow,n}^{k,\mathrm{res}}$ are calculated out of Eq. (5.35b) analogously to the single-atom case, i.e., Eq. (5.35b) is reformulated as a matrix differential equation of

the form of Eq. (5.13), but with the following replacements in the matrix $M_{n,m}$:

$$A \to A(S_z^k),$$
$$A^\dagger \to A^\dagger(S_z^k),$$
$$\Delta \to \Delta(S_z^k) = E(S_z^k)/\hbar - \omega = \Delta - 4\omega p_0^2 S_z^k.$$

The solution of this matrix differential equation generalizes Eq (5.14) as follows,

$$\rho_{\uparrow,n;\downarrow,n+1}^{k,\mathrm{res}} = g\Gamma_1 \frac{\langle n| A(S_z^k) |n+1\rangle}{\det M_{n,n}(S_z^k)} \left[\rho_{n,n}\Gamma_\uparrow \left(\Delta(S_z^k) + i\Gamma_\varphi\right) - \rho_{n+1,n+1}\Gamma_\downarrow \left(\Delta(S_z^k) + i\Gamma_\varphi\right) \right],$$

$$\rho_{\downarrow,n+1;\uparrow,n}^{k,\mathrm{res}} = g\Gamma_1 \frac{\langle n+1| A^\dagger(S_z^k) |n\rangle}{\det M_{n,n}(S_z^k)} \left[\rho_{n,n}\Gamma_\uparrow \left(\Delta(S_z^k) - i\Gamma_\varphi\right) - \rho_{n+1,n+1}\Gamma_\downarrow \left(\Delta(S_z^k) - i\Gamma_\varphi\right) \right],$$

$$\det M_{n,n}(S_z^k) = \Gamma_1^2 \Gamma_\varphi^2 \left(1 + \frac{4g^2}{\Gamma_1\Gamma_\varphi} N_n(S_z^k)\right),$$

$$N_n(S_z^k) = \frac{\Delta^2(S_z^k)}{4g^2} \frac{\Gamma_1}{\Gamma_\varphi} + \langle n+1| A^\dagger(S_z^k) |n\rangle \langle n| A(S_z^k) |n+1\rangle.$$

For later we also give the results for the diagonal matrix elements of $\rho^{k,\mathrm{res}}$,

$$\rho_{\uparrow n,\uparrow n}^{k,\mathrm{res}} = \frac{\Gamma_\uparrow}{\Gamma_1} \rho_{n,n} - \frac{\kappa}{\Gamma_1 M}(n+1)\Big((N_\mathrm{th}+1)\rho_{n+1,n+1} - N_\mathrm{th}\rho_{n,n}\Big) \text{ and} \qquad (5.36a)$$

$$\rho_{\downarrow n,\downarrow n}^{k,\mathrm{res}} = \frac{\Gamma_\downarrow}{\Gamma_1} \rho_{n,n} + \frac{\kappa}{\Gamma_1 M}n\Big((N_\mathrm{th}+1)\rho_{n,n} - N_\mathrm{th}\rho_{n-1,n-1}\Big). \qquad (5.36b)$$

The equation of motion of the diagonal elements of the reduced resonator density matrix, Eq. (5.15), now takes the following form:

$$\frac{\mathrm{d}}{\mathrm{d}t}\rho_{n,n} = \kappa(N_\mathrm{th}+1)(n+1)\rho_{n+1,n+1} - \kappa N_\mathrm{th}(n+1)\rho_{n,n}$$
$$- \kappa(N_\mathrm{th}+1)n\rho_{n,n} + \kappa N_\mathrm{th}n\rho_{n-1,n-1}$$
$$+ \frac{M\mathcal{A}}{1+2\mathcal{A}N_n(S_z^k)} \left|\langle n| A(S_z^k) |n+1\rangle\right|^2 (\Gamma_\downarrow\rho_{n+1,n+1} - \Gamma_\uparrow\rho_{n,n})$$
$$- \frac{M\mathcal{A}}{1+2\mathcal{A}N_{n-1}(S_z^k)} \left|\langle n-1| A(S_z^k) |n\rangle\right|^2 (\Gamma_\downarrow\rho_{n,n} - \Gamma_\uparrow\rho_{n-1,n-1}).$$

The quantity $\mathcal{A} = \frac{2g^2}{\Gamma_1\Gamma_\varphi}$ is the same as in the single-atom case. The recursion relation (5.16) obtained out of a detailed balance condition is modified as well,

$$\rho_{n,n} = f_n \rho_{n-1,n-1}, \qquad (5.37a)$$

$$f_n = \frac{\kappa N_\mathrm{th}n + \Gamma_\uparrow \frac{M\mathcal{A}}{1+2\mathcal{A}N_{n-1}(S_z^k)} \left|\langle n-1| A(S_z^k) |n\rangle\right|^2}{\kappa(N_\mathrm{th}+1)n + \Gamma_\downarrow \frac{M\mathcal{A}}{1+2\mathcal{A}N_{n-1}(S_z^k)} |\langle n-1| A(S_z^k) |n\rangle|^2}. \qquad (5.37b)$$

This result shows that for the multi-atom laser the bare pumping and relaxation rates are rescaled by the number of atoms M, $\Gamma_{\uparrow/\downarrow} \to M\Gamma_{\uparrow/\downarrow}$. Therefore, the maximum photon number of a conventional laser with pure σ_x coupling scales linearly with M,

$$n_\mathrm{m}^\mathrm{cl} = \frac{1}{2}\left(M\frac{\Gamma_\uparrow - \Gamma_\downarrow}{\kappa} - \frac{1}{\mathcal{A}}\right) - \frac{\Delta^2}{4g^2}\frac{\Gamma_1}{\Gamma_\varphi}.$$

The suppression of higher-order transitions and the derivation of the Lindblad superoperators describing pumping, relaxation, and dephasing hold for the multi-atom case as well.

(a)

(b)
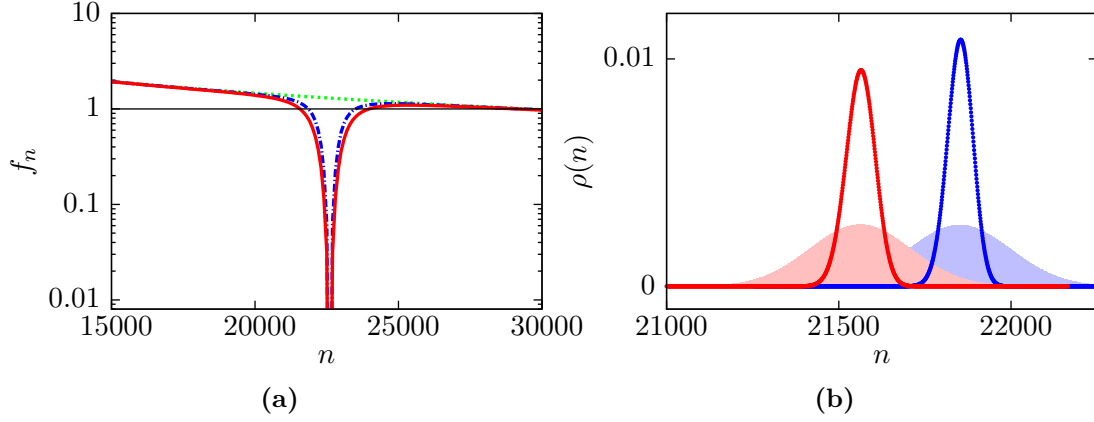
Figure 5.9.: Recursion coefficient and photon statistics in a multi-atom lasing setup. **(a)**: Comparison of the recursion coefficient f_n in the single-atom case (dash-dotted blue line, $\kappa = 1 \times 10^{-7} \, \omega$) with the recursion coefficient for $M = 100$ atoms (solid red line, $\kappa = 1 \times 10^{-5} \, \omega$). The dotted green curve represents the results obtained for a conventional laser with pure σ_x coupling. **(b)**: Corresponding photon statistics $\rho(n)$ for $M = 1$ atom (blue curve) and $M = 100$ atoms (red curve). Both setups produce photon-number squeezed light with a Fano factor of $F_p = 0.062$ and $F_p = 0.082$ in the polaron frame, which corresponds to a Fano factor of $F = 0.062$ and $F = 0.144$ in the cavity frame, respectively. The photon-number expectation values are $\langle n \rangle = 21562$ and $\langle n \rangle = 21851$, respectively. The filled faint red and blue curves represent a Poissonian statistics with the same mean photon number, which is the result for a conventional laser. The plot parameters are $g = 0.0067 \, \omega$, $\theta = \pi/10$, $\Gamma_\uparrow = 0.006 \, \omega$, $\Gamma_\downarrow = 0.0001 \, \omega$, $\Gamma_\varphi^* = 0.001 \, \omega$, $\Delta = 0 \, \omega$, and $N_{\mathrm{th}} = 0$. For the multi-atom lasing setup we have $S_z^k = 25.76$.

In Fig. 5.9a the recursion coefficient in the single-atom case (dash-dotted blue line) is compared to the corresponding quantity in the multi-atom case (solid red line). The resonator decay rate κ is rescaled by a factor of M in the multi-atom lasing setup to compensate the increase of the pumping rate by the same factor. Therefore, the recursion coefficients are of the same order of magnitude and coincide for photon numbers away from the roots of the coupling matrix element. As expected from Eq. (5.33) the roots of the coupling matrix elements are identical for the single-atom and the multi-atom case. However, the range of photon numbers in which f_n drops to zero near a root of the coupling matrix elements depends on the value of S_z^j and is increased for a multi-atom lasing setup. In Fig. (5.9b) the corresponding photon statistics in the polaron frame are shown. The increase of the drop region of the recursion coefficient due to a nonzero value $S_z^k > 0$ decreases the photon-number expectation value $\langle n \rangle$ of the multi-atom lasing setup and increases the Fano factor F_p in the polaron frame.

5.10.3. Self-consistency equation

The photon statistics $\rho(n)$ is calculated numerically by evaluating Eq. (5.37) with the methods described in Sec. 5.4.3. Out of $\rho(n)$ the atomic polarization S_z^k is determined. Using the matrix elements (5.36) we obtain the following expression for S_z^k:

$$S_z^k = \sum_{\substack{i \neq k \\ i=1}}^{M} \left\langle \sigma_z^i \right\rangle = \sum_{\substack{i \neq k \\ i=1}}^{M} \sum_n \left(\rho_{\uparrow,n;\uparrow,n}^{i,\mathrm{res}} - \rho_{\downarrow,n;\downarrow,n}^{i,\mathrm{res}} \right) = (M-1)D_0 - \frac{M-1}{M} \frac{2\kappa}{\Gamma_1} \left(\langle n \rangle - N_{\mathrm{th}} \right) .$$

$$(5.38)$$

The value of S_z^k depends on the photon statistics $\rho(n)$ via the photon-number expectation value $\langle n \rangle$. In turn, $\rho(n)$ is determined by the recursion relation (5.37) that depends

on S_z^k. A self-consistent solution for these coupled quantities $\rho(n)$ and S_z^k is calculated iteratively, starting with an initial guess for S_z^k. The number of necessary iterations depends significantly on this initial guess and should be as small as possible because the numerical evaluation of the recursion relation (5.37) is slow.

A good estimate on S_z^k can be obtained as follows: The recursion coefficient f_n is plotted for $S_z^k = 0$ and the maximum $n_{\max}$ of the photon statistics, defined by $f_{n_{\max}} = 1$ and $f'_{n_{\max}} < 0$, is calculated numerically. This calculation is performed much faster than the evaluation of the recursion relation (5.37). Then, an estimate on S_z^k is obtained using Eq. (5.38) with the photon-number expectation value $\langle n \rangle$ set to $n_{\max}$. If necessary, these two steps are repeated several times until the estimate for S_z^k converges to a constant value. Finally, this value is used as an initial guess in the numerical evaluation of the recursion relation (5.37).

For a conventional laser the photon-number expectation value $\langle n \rangle$ is determined by the balance of pumping and loss rates. Therefore, the atomic polarization $\langle \sigma_z^i \rangle$ is close to zero for all atoms and we have $S_z^k \approx 0$. However, for a laser producing squeezed light the photon-number expectation value $\langle n \rangle$ is determined by the position of the roots of the coupling matrix elements and, in general, we have $\langle \sigma_z^i \rangle \neq 0$ and $S_z^k \neq 0$. The value of S_z^k is a measure how deep the laser is operated in the trapping regime, where the photon-number expectation value is fixed by a root n_0^i of the coupling matrix elements. When the pumping rate $\Gamma_\uparrow$ is increased, the quantity S_z^k increases starting from the value $S_z^k \approx 0$ of a conventional laser to $S_z^k > 0$. Right before the trapping breaks down, S_z^k reaches a maximum value (point "c" in Fig. 5.5) and then jumps back to $S_z^k \approx 0$ (point "a" in Fig. 5.5).

5.10.4. Fano factor

The Fano factor F_{p} in the polaron frame is obtained out of the self-consistently calculated photon statistics $\rho(n)$. As discussed for the single-atom case it differs from the Fano factor F defined in the cavity frame by corrections due to the polaron transformation. In this subsection the corrections for the multi-atom lasing setup are calculated. Out of Eqs. (5.24a) and (5.24b) the following corrections are obtained for the nominator of the Fano factor:

$$
\begin{aligned}
\left\langle n_{\mathrm{c}}^2 \right\rangle - \left\langle n_{\mathrm{c}} \right\rangle^2 = {} & \left\langle n^2 \right\rangle - \langle n \rangle^2 \\
& - \left\langle \xi \left(a^\dagger a (a + a^\dagger) + (a + a^\dagger) a^\dagger a \right) \right\rangle + 2 \left\langle a^\dagger a \right\rangle \left\langle \xi (a + a^\dagger) \right\rangle \\
& + \left\langle \xi^2 \left(a^2 + (a^\dagger)^2 + 4 a^\dagger a + 1 \right) \right\rangle - \left\langle \xi (a + a^\dagger) \right\rangle^2 - 2 \left\langle a^\dagger a \right\rangle \left\langle \xi^2 \right\rangle \\
& - 2 \left\langle \xi^3 (a + a^\dagger) \right\rangle + 2 \langle \xi \rangle^2 \left\langle \xi (a + a^\dagger) \right\rangle \\
& + \left\langle \xi^4 \right\rangle - \left\langle \xi^2 \right\rangle^2 \, ,
\end{aligned}
$$

with $\xi = p_0 \sum_{i=1}^M \sigma_z^i$. Most of the terms cancel because of the following reasons:

1. Within the mean-field approach the expectation values of products of σ_z operators factorize, i.e., $\langle \xi^r \rangle = \langle \xi \rangle^r$ and $\left\langle \xi^r \xi a^{(\dagger)} \right\rangle = \langle \xi \rangle^r \left\langle \xi a^{(\dagger)} \right\rangle$ for $r \in \mathbb{N}_0$, and

2. energy-nonconserving matrix elements are zero, i.e., $\left\langle \xi a^{(\dagger)} \right\rangle \propto \rho_{\sigma,n;\sigma,n\pm 1} = 0$.

Hence, only three of the correction terms remain,

$$
\left\langle n_{\mathrm{c}}^2 \right\rangle - \left\langle n_{\mathrm{c}} \right\rangle^2 = \left\langle n^2 \right\rangle - \langle n \rangle^2 + 4 \left\langle \xi^2 a^\dagger a \right\rangle + \left\langle \xi^2 \right\rangle - 2 \left\langle a^\dagger a \right\rangle \left\langle \xi^2 \right\rangle .
$$

The expectation values $\langle \xi^2 \rangle$ and $\langle \xi^2 a^\dagger a \rangle$ are obtained using Eq. (5.36),

$$\left\langle \xi^2 \right\rangle = p_0^2 M + p_0^2 \frac{M}{M-1} \left(S_z^k \right)^2 ,$$

$$\left\langle \xi^2 a^\dagger a \right\rangle = \langle n \rangle \left\langle \xi^2 \right\rangle - p_0^2 \frac{2\kappa}{\Gamma_1} S_z^k \left[\left\langle n^2 \right\rangle - (\langle n \rangle + N_{\text{th}}) \left(\langle n \rangle + \frac{1}{2} \right) \right] .$$

Therefore, the Fano factor in the cavity frame is given by

$$F = \frac{F_{\text{p}} \langle n \rangle + (2 \langle n \rangle + 1) \langle \xi^2 \rangle - p_0^2 \frac{8\kappa}{\Gamma_1} S_z^k \left[\langle n^2 \rangle - (\langle n \rangle + N_{\text{th}}) \left(\langle n \rangle + \frac{1}{2} \right) \right]}{\langle n \rangle + \langle \xi^2 \rangle} .$$

In order to clarify the structure of this equation we use the approximations $1, N_{\text{th}}, F_{\text{p}}, \langle \xi^2 \rangle \ll \langle n \rangle$. Then, F can be rewritten as

$$F = F_{\text{p}} \left(1 - p_0^2 \frac{8\kappa}{\Gamma_1} S_z^k \right) + 2 \left(p_0^2 M + p_0^2 \frac{M}{M-1} \left(S_z^k \right)^2 \right) . \tag{5.39}$$

All corrections proportional to p_0^2 are negligible for typical lasing parameters, except of the last term: As discussed in the previous subsection, in general the atomic polarization $\langle \sigma_z^j \rangle$ is nonzero for a laser that produces squeezed light. Therefore, we have $0 \leq |S_z^k| \leq M$. For typical lasing parameters and M of the order of 100 it holds $p_0^2 M \ll 1$, but $p_0^2 M^2$ may be of the order of unity. Hence, the last term in Eq. (5.39) can be a relevant correction to F_{p} depending on the actual numerical value of S_z^k,

$$F \approx F_{\text{p}} + 2 p_0^2 \left(S_z^k \right)^2 \leq F_{\text{p}} + 2 p_0^2 M^2 . \tag{5.40}$$

In conclusion, for a multi-atom setup large corrections to F_{p} may arise, depending on the value of S_z^k. Even a Fano factor $F > 1$ may be reached, i.e., larger fluctuations appear than for a conventional laser. In order to avoid this the lasing parameters have to be chosen such that S_z^k is close to zero. This is the case if the photon-number expectation value $\langle n \rangle$ is close to the photon number $n_{\text{max}}^{\text{cl}}$ corresponding to the maximum of the photon statistics of a conventional laser. This means that a multi-atom lasing setup should be operated at the smallest possible pumping rate $\Gamma_\uparrow$ that allows for a trapping of the photon-number expectation value $\langle n \rangle$ by a root n_0^i. If $\Gamma_\uparrow$ is increased, the laser is further driven into the trapping regime and corrections to F_{p} due to a nonzero value of S_z^k may spoil squeezing. On the other hand, if a nonzero value of S_z^k cannot be avoided and if the Fano factor F should not exceed a certain threshold value, Eq. (5.40) puts an upper bound on the number of atoms M in the setup.

5.10.5. Photon statistics in the cavity frame

The corrections to the Fano factor in the polaron frame and the increase of the Fano factor in the cavity frame for large values of S_z^k are due to the fact that $|\sigma, n\rangle$ is actually a superposition of several cavity-frame states $|\sigma, m_{\text{c}}\rangle$. The cavity-frame photon statistics is a convolution of the polaron-frame photon statistics and the decomposition of a polaron frame into cavity states. This broadens the photon statistics in the cavity frame. In this section we derive an approximation of the photon statistics in the cavity frame in order to qualitatively understand the enhancement of the Fano factor.

The polaron transformation is essentially a displacement operator

$$U = \exp \left[p_0 \sum_{i=1}^{M} \sigma_z^i \left(a - a^\dagger \right) \right] = \exp \left[\alpha a^\dagger - \alpha^* a \right] = D(\alpha) ,$$

where α is the displacement parameter. It holds $U^\dagger = D(-\alpha)$. The displacement parameter α is in this case a real quantity and proportional to the sum of all atomic polarizations,

$$\alpha = \alpha^* = -p_0 \sum_{i=1}^{M} \sigma_z^i \, .$$

In the following we denote the combined atomic and resonator states of a M-atom system by $|\boldsymbol{\sigma}, n\rangle = |\boldsymbol{\sigma}\rangle \otimes |n\rangle$, where the vector $\boldsymbol{\sigma}$ contains the M atomic states, $\boldsymbol{\sigma} = (\sigma_z^1, \ldots, \sigma_z^M)$. In the Appendix B.2 the decomposition of a polaron-frame state $|\boldsymbol{\sigma}, n\rangle$ into cavity-frame states $|\boldsymbol{\sigma}, m_\mathrm{c}\rangle$ is derived, yielding

$$|\boldsymbol{\sigma}, n\rangle = \sum_{m=0}^{\infty} a_{n,m}(\alpha(\boldsymbol{\sigma})) |\boldsymbol{\sigma}, m_\mathrm{c}\rangle \, ,$$

$$a_{n,m}(\alpha) = \frac{1}{\sqrt{n!m!}} e^{-|\alpha|^2/2} \sum_{k=0}^{n} (-1)^{n+k} \binom{n}{k} \frac{m!}{(m-k)!} (-\alpha)^{m+n-2k} \Theta(m-k) \, ,$$

where $\Theta(x)$ is the Heaviside step function, which is equal to unity for a non-negative argument and zero otherwise.

Using this decomposition the full polaron-frame density matrix ρ is expanded in the basis of cavity states,

$$\rho = \sum_{\boldsymbol{\sigma}, \boldsymbol{\sigma}'} \sum_{n,n'} \rho_{\boldsymbol{\sigma}, n; \boldsymbol{\sigma}', n'} |\boldsymbol{\sigma}, n\rangle \langle \boldsymbol{\sigma}', n'|$$

$$= \sum_{\boldsymbol{\sigma}, \boldsymbol{\sigma}'} \sum_{n,n'} \sum_{m,m'} \rho_{\boldsymbol{\sigma}, n; \boldsymbol{\sigma}', n'} a_{n,m}(\alpha) a_{n',m'}^*(\alpha') |\boldsymbol{\sigma}, m_\mathrm{c}\rangle \langle \boldsymbol{\sigma}', m_\mathrm{c}'| \, ,$$

where α depends on the atomic state vector $\boldsymbol{\sigma}$ and α' on $\boldsymbol{\sigma}'$. We read off the following transformation from the polaron-frame density matrix elements $\rho_{\boldsymbol{\sigma}, n; \boldsymbol{\sigma}', n'}$ to the corresponding cavity-frame quantities $\rho_{\boldsymbol{\sigma}, m; \boldsymbol{\sigma}', m'}^\mathrm{cav}$:

$$\rho_{\boldsymbol{\sigma}, m; \boldsymbol{\sigma}', m'}^\mathrm{cav} = \sum_{n,n'} \rho_{\boldsymbol{\sigma}, n; \boldsymbol{\sigma}', n'} a_{n,m}(\alpha) a_{n',m'}^*(\alpha') \, .$$

The photon statistics in the cavity frame is given by

$$\rho_{m,m}^\mathrm{cav} = \sum_{\boldsymbol{\sigma}} \rho_{\boldsymbol{\sigma}, m; \boldsymbol{\sigma}, m}^\mathrm{cav} = \sum_{\boldsymbol{\sigma}} \sum_{n,n'} \rho_{\boldsymbol{\sigma}, n; \boldsymbol{\sigma}, n'} a_{n,m}(\alpha) a_{n',m}^*(\alpha)$$

$$= \sum_{\boldsymbol{\sigma}} \sum_{n=0}^{\infty} \rho_{\boldsymbol{\sigma}, n; \boldsymbol{\sigma}, n} |a_{n,m}(\alpha)|^2 \, . \qquad (5.41)$$

In the last step we used that only diagonal elements of the stationary density matrix in the polaron frame are nonzero [41].

In order to evaluate Eq. (5.41) numerically the sum over the photon numbers n is restricted to all n for that $a_{n,m}(\alpha)$ is nonzero. The matrix element $\rho_{\boldsymbol{\sigma}, n; \boldsymbol{\sigma}, n}$ is approximated by $\rho_{n,n}$ multiplied with the probability $p_{\boldsymbol{\sigma}}$ to find the system in the state $|\boldsymbol{\sigma}\rangle$, which is obtained as follows: For M identical atoms the polarization $\langle \sigma_z \rangle$ of each atom is $\langle \sigma_z \rangle = S_z^k/(M-1)$ and the probability $p_{\uparrow/\downarrow}$ for this atom to be in the state $|\uparrow\rangle$ or $|\downarrow\rangle$, respectively, is

$$p_\uparrow = \frac{1 + \langle \sigma_z \rangle}{2} \quad \text{and} \quad p_\downarrow = \frac{1 - \langle \sigma_z \rangle}{2} \, .$$
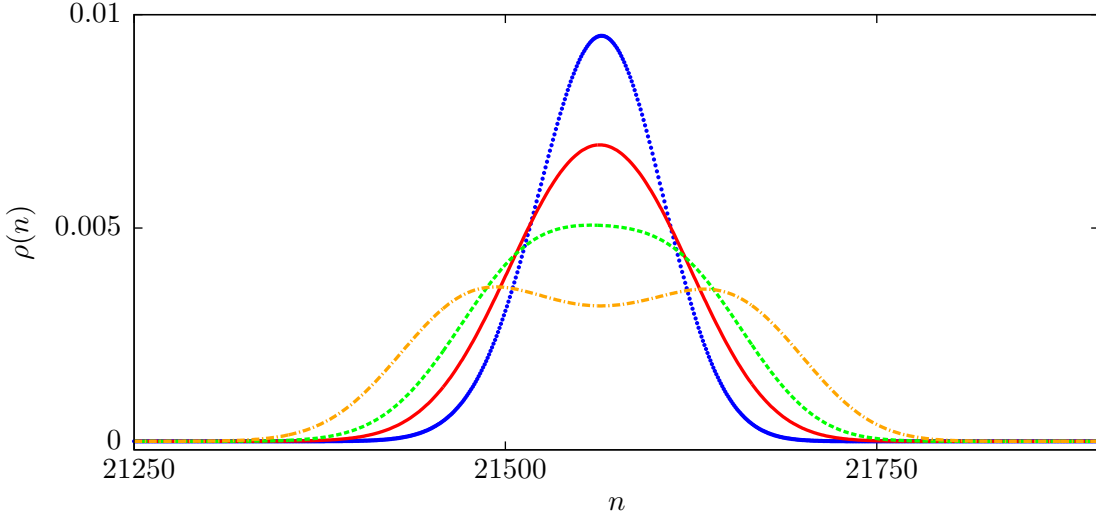
Figure 5.10.: Comparison of the photon statistics in the polaron and the cavity frame. The blue dots represent the photon statistics in the polaron frame shown in Fig. 5.9b. Its plot parameters are $M = 100$, $g = 0.0067\,\omega$, $\theta = \pi/10$, $\Gamma_\uparrow = 0.006\,\omega$, $\Gamma_\downarrow = 0.0001\,\omega$, $\Gamma_\varphi^* = 0.001\,\omega$, $\Delta = 0\,\omega$, $\kappa = 1 \times 10^{-5}\,\omega$, and $N_{\text{th}} = 0$. It has a Fano factor $F_{\text{p}} = 0.082$ in the polaron frame and $S_z^k = 25.76$. The solid red line represents the corresponding photon statistics in the cavity frame with a Fano factor $F = 0.144$. The dashed green and the dash-dotted orange lines represent the photon statistics in the cavity frame which one would obtain for $S_z^j = 40$ and 60 with a Fano factor of $F = 0.22$ and $F = 0.39$, respectively. For large S_z^j the photon statistics in the cavity frame evolves into a double-peaked shape corresponding to a large Fano factor.

As all M atoms are assumed to be identical the total number of atoms in the state $|\downarrow\rangle$, N, defines the state of the multi-atom system completely. Hence, the probability of a state $|\boldsymbol{\sigma}\rangle$ with N atoms being in the state $|\downarrow\rangle$ and $M - N$ atoms being in the state $|\uparrow\rangle$ is given by

$$p_{\boldsymbol{\sigma}} = p(N) = \begin{pmatrix} M \\ M - N, N \end{pmatrix} p_\downarrow^N p_\uparrow^{M-N} \, ,$$

where the multinomial coefficient accounts for the different combinatoric possibilities to distribute the state $|\downarrow\rangle$ on N out of M atoms. The displacement coefficient $\alpha(\boldsymbol{\sigma})$ is also expressed in terms of N, $\alpha(N) = -p_0(M - 2N)$, such that we finally obtain

$$\rho_{m,m}^{\text{cav}} = \sum_{N=0}^{M} \sum_{n=0}^{\infty} \rho_{n,n} p(N) \left| \alpha_{n,m}(\alpha(N)) \right|^2 \, . \tag{5.42}$$

Figure 5.10 shows numerical results obtained for different values of S_z^k. The blue dots represent the photon statistics in the polaron frame. For small values of S_z^k the photon statistics in the cavity frame is broadened, but still has a single peak (solid red and dashed green curves). However, for large values of S_z^k the photon statistics evolves into a symmetric double-peaked shape corresponding to a strongly increased Fano factor $F > 1$ (dash-dotted orange curve).

The arising of a double-peaked photon statistics can be understood as follows: The polaron transformation shifts a state $|\psi\rangle = \sum_n g(n) |\sigma, n\rangle$ in the photon-number space, i.e., if its distribution $g(n)$ was originally peaked at a certain photon number n_{peak}, the polaron-transformed state $U |\psi\rangle$ is peaked at a different photon number n'_{peak}. However, the expansion coefficients $a_{n,m}(\alpha)$ in Eq. (5.41) are squared because both states in the projector

$|\boldsymbol{\sigma}, n\rangle \langle \boldsymbol{\sigma}, n|$ undergo a polaron transformation. Therefore, the dash-dotted orange cavity-frame photon statistics in Fig. 5.10 has two peaks shifted symmetrically to the maximum of the polaron-frame photon statistics.

The distance of the shift is given by the parameter $\alpha(\boldsymbol{\sigma})$ and depends on the atomic expectation values $\langle \sigma_z^j \rangle$. Equation (5.42) shows that the sum of the atomic states $|\boldsymbol{\sigma}\rangle$ represents essentially a superposition of all possible displacement parameters $\alpha(\boldsymbol{\sigma})$ weighted with the probability of the realization of the corresponding atomic state $|\boldsymbol{\sigma}\rangle$. If the sum of atomic polarizations is close to zero, $S_z^k \approx 0$, both atomic states $|\uparrow\rangle$ and $|\downarrow\rangle$ are equally probable, $p_\uparrow \approx p_\downarrow$. Hence, most of the multi-atom states $|\boldsymbol{\sigma}\rangle$ correspond to a displacement parameter $\alpha(\boldsymbol{\sigma}) \approx 0$ and the cavity-frame photon statistics is only weakly shifted compared to the polaron-frame statistics. However, if we have $S_z^k > 0$, the probability $p_\uparrow$ is larger than $p_\downarrow$ and, therefore, most of the atomic states $|\boldsymbol{\sigma}\rangle$ yield a nonzero shift parameter $\alpha(\boldsymbol{\sigma}) > 0$. Then, the polaron-frame photon statistics is shifted to lower and higher photon numbers, which causes the broadening and the double-peaked shape.

5.11. Disorder in the mixing angle and the detuning

As discussed in the introduction different superconducting circuits, e.g., charge and flux qubits, as well as quantum dots are described by the same effective Hamiltonian (1.2),

$$H = \frac{\delta}{2}\sigma_z - \frac{t}{2}\sigma_x \, .$$

For a charge qubit the level-splitting energy δ is proportional to the control charge on the superconducting island and t is the Josephson energy of the junction. For a flux qubit δ describes the asymmetry of the double-well potential and t is the tunneling amplitude through the potential barrier.

The dominant source of noise in charge qubits are fluctuations of the control charge. This so-called charge noise introduces fluctuations in the level-splitting energy δ which translate into a fluctuating mixing angle $\theta = \tan^{-1}(-t/\delta)$. Flux qubits are designed to be independent of charge fluctuations as the qubit control is based on the magnetic flux. However, experiments revealed that flux qubits are sensitive to so-called flux noise. It is caused, for instance, by flux trapping or fluctuations of the critical current of the Josephson junctions [15]. Inhomogeneities in the applied magnetic flux in metamaterials built out of a large number of flux qubits may also lead to different flux biases for the individual qubits. In conclusion, also in a flux qubit system the parameters δ and t are affected by noise, which translates into fluctuations of the mixing angle θ. Simultaneously, also the detuning $\Delta = \sqrt{\delta^2 + t^2}/\hbar - \omega$ is subject to variations as it depends on δ and t as well.

In order to obtain understand the influence of these effects on squeezing we examine numerically disorder in the mixing angle θ and the detuning Δ in a multi-atom lasing setup. We consider the following Hamiltonian,

$$H_M = \hbar\omega a^\dagger a + \sum_{j=1}^{M} \frac{1}{2}\epsilon_j \sigma_z^j + \sum_{j=1}^{M} \hbar g \left(\cos(\theta_j)\sigma_z^j + \sin(\theta_j)\sigma_x^j \right) \left(a^\dagger + a \right) , \qquad (5.43)$$

with an individual mixing angle θ_i and an individual level-splitting energy ϵ_i of each atom i. The generalization of our calculations to this Hamiltonian is given in the following subsection. Numerical results are presented in subsection 5.11.2.

5.11.1. Photon statistics and Fano factor in disordered lasing setups

The polaron transformation that maps the Hamiltonian (5.43) on a Jaynes-Cummings-like Hamiltonian depends in a disordered setup on the individual mixing angles θ_j,

$$U = \exp\left[i\sum_{j=1}^{M} p_j \sigma_z^j\right],$$

$$p_j = i p_{0,j}\left(a^\dagger - a\right) = i\frac{g}{\omega}\cos(\theta_j)\left(a^\dagger - a\right),$$

$$x_j = x_{0,j}\left(a^\dagger + a\right) = \hbar g \sin(\theta_j)\left(a^\dagger + a\right).$$

The polaron-transformed Hamiltonian reads

$$H_{\mathrm{p}} = \sum_{j=1}^{M}\frac{1}{2}\epsilon_j\sigma_z^j + \hbar\omega a^\dagger a + \hbar g\sum_{j=1}^{M}\left(\sigma_+^j\frac{e^{-ip_j}x_j e^{-ip_j}}{\hbar g} + \sigma_-^j\frac{e^{ip_j}x_j e^{ip_j}}{\hbar g}\right)$$
$$- \hbar\omega\sum_{j=1}^{M}p_{0,j}^2 - \hbar\omega\sum_{j\neq l=1}^{M}p_{0,j}p_{0,l}\sigma_z^j\sigma_z^l - 2\sum_{j\neq l=1}^{M}x_{0,j}p_{0,l}\left(\sigma_+^j\sigma_z^l e^{-2ip_j} + \sigma_-^j\sigma_z^l e^{2ip_j}\right).$$

Again, a mean-field approximation is performed, i.e., products of Pauli matrices are rewritten using the approximation (5.29), and a self-consistency equation is introduced,

$$\tilde{S}_z^j = \sum_{\substack{i\neq j \\ i=1}}^{M} p_{0,i}\left\langle\sigma_z^i\right\rangle.$$

Note that, compared to Eq. (5.30), $\tilde{S}_z^j$ includes an additional factor $p_{0,j}$. The effective Hamiltonian within this mean-field approach is given by

$$H_{\mathrm{MF}} = \hbar\omega a^\dagger a + \sum_{j=1}^{M}\frac{1}{2}\tilde{E}_j(\tilde{S}_z^j)\sigma_z^j + \hbar g\sum_{j=1}^{M}\left[\sigma_+^j\tilde{A}(\tilde{S}_z^j) + \sigma_-^j\tilde{A}^\dagger(\tilde{S}_z^j)\right] + \mathrm{const},$$

$$\tilde{E}_j(\tilde{S}_z^j) = \epsilon_j - 4\hbar\omega p_{0,j}\tilde{S}_z^j,$$

$$\tilde{A}_j(\tilde{S}_z^j) = \frac{e^{-ip_j}x_j e^{-ip_j}}{\hbar g} - \frac{2}{\hbar g}x_{0,j}\tilde{S}_z^j e^{-2ip_j}.$$

The master equation for the diagonal elements of the reduced density matrix of the resonator reads

$$\frac{\mathrm{d}}{\mathrm{d}t}\rho_{n,n} = \kappa(N_{\mathrm{th}}+1)(n+1)\rho_{n+1,n+1} - \kappa N_{\mathrm{th}}(n+1)\rho_{n,n}$$
$$- \kappa(N_{\mathrm{th}}+1)n\rho_{n,n} + \kappa N_{\mathrm{th}}n\rho_{n-1,n-1}$$
$$+ \sum_{j=1}^{M}\left[\frac{\mathcal{A}}{1+2\mathcal{A}N_n^j(\tilde{S}_z^j)}\left|\langle n|\tilde{A}_j(\tilde{S}_z^j)|n+1\rangle\right|^2(\Gamma_\downarrow\rho_{n+1,n+1} - \Gamma_\uparrow\rho_{n,n})\right.$$
$$\left. - \frac{\mathcal{A}}{1+2\mathcal{A}N_{n-1}^j(\tilde{S}_z^k)}\left|\langle n-1|\tilde{A}_j(\tilde{S}_z^j)|n\rangle\right|^2(\Gamma_\downarrow\rho_{n,n} - \Gamma_\uparrow\rho_{n-1,n-1})\right],$$

$$N_n^j(\tilde{S}_z^j) = \frac{\left(\Delta_j - 4\omega p_{0,j}\tilde{S}_z^j\right)^2}{4g^2}\frac{\Gamma_1}{\Gamma_\varphi} + \left|\langle n|\tilde{A}_j(\tilde{S}_z^j)|n+1\rangle\right|^2,$$

with $\mathcal{A} = 2g^2/(\Gamma_1 \Gamma_\varphi)$. The stationary solution for the diagonal elements $\rho_{n,n}$ of the reduced density matrix of the resonator is defined by the following recursion relation,

$$\rho_{n,n} = \tilde{f}_n \rho_{n-1,n-1}\,, \tag{5.44a}$$

$$\tilde{f}_n = \frac{\kappa N_{\text{th}} n + \Gamma_\uparrow \sum_{j=1}^M \frac{\mathcal{A}}{1+2\mathcal{A}N_{n-1}^j(\tilde{S}_z^j)} \left| \langle n-1 | \, \tilde{A}_j(\tilde{S}_z^j) \, | n \rangle \right|^2}{\kappa(N_{\text{th}}+1)n + \Gamma_\downarrow \sum_{j=1}^M \frac{\mathcal{A}}{1+2\mathcal{A}N_{n-1}^j(\tilde{S}_z^j)} \left| \langle n-1 | \, \tilde{A}_j(\tilde{S}_z^j) \, | n \rangle \right|^2}\,. \tag{5.44b}$$

The self-consistency condition is now

$$\tilde{S}_z^i = D_0 \sum_{\substack{j \neq i \\ j=1}}^M p_{0,j} + \frac{2\kappa}{\Gamma_1} \sum_{n=0}^\infty f_i(n)(n+1)\Big(N_{\text{th}}\rho_{n,n} - (N_{\text{th}}+1)\rho_{n+1,n+1}\Big)\,, \tag{5.45a}$$

$$f_i(n) = \left(\sum_{\substack{j \neq i \\ j=1}}^M p_{0,j} \frac{\left| \langle n | \, \tilde{A}_j(\tilde{S}_z^j) \, | n+1 \rangle \right|^2}{1 + 2\mathcal{A}N_n^j(\tilde{S}_z^j)} \right) \left(\sum_{l=1}^M \frac{\left| \langle n | \, \tilde{A}_l(\tilde{S}_z^l) \, | n+1 \rangle \right|^2}{1 + 2\mathcal{A}N_n^l(\tilde{S}_z^l)} \right)^{-1}\,. \tag{5.45b}$$

For a given set of lasing parameters $\{\Delta_j\}$, $\{\theta_j\}$, and $\{S_z^j\}$, Eqs. (5.44) and (5.45) can be solved numerically.

The Fano factor F in the cavity frame is given by

$$F = \frac{\langle n^2 \rangle - \langle n \rangle^2 + (2\langle n \rangle + 1)\langle \xi^2 \rangle + 4(X+Y)}{\langle n \rangle + \langle \xi^2 \rangle}\,,$$

$$\langle \xi^2 \rangle = \sum_{i=1}^M p_{0,i}^2 + D_0 \sum_{i=1}^M p_{0,i}\tilde{S}_z^i$$

$$+ \frac{2}{\Gamma_1} \sum_{i=1}^M p_{0,i}\tilde{S}_z^i \sum_{n=0}^\infty \frac{\mathcal{A}}{1+2\mathcal{A}N_n^i(\tilde{S}_z^i)} \left| \langle n | \, \tilde{A}_i(\tilde{S}_z^i) \, | n+1 \rangle \right|^2 (\Gamma_\downarrow \rho_{n+1} - \Gamma_\uparrow \rho_n)\,,$$

$$X = \frac{2\kappa}{\Gamma_1} D_0 \sum_{i=1}^M p_{0,i} \sum_{n=0}^\infty \left(n + \frac{1}{2} - \langle n \rangle \right)(n+1)f_i(n)\left[N_{\text{th}}\rho_n - (N_{\text{th}}+1)\rho_{n+1}\right]\,,$$

$$Y = \frac{4\kappa}{\Gamma_1^2} \sum_{i=1}^M p_{0,i} \sum_{n=0}^\infty \left[\frac{\mathcal{A}}{1+2\mathcal{A}N_n^i(\tilde{S}_z^i)} \left| \langle n | \, \tilde{A}_i(\tilde{S}_z^i) \, | n+1 \rangle \right|^2 (\Gamma_\downarrow \rho_{n+1} - \Gamma_\uparrow \rho_n) \right]$$

$$\times \sum_{m=0}^\infty \left[f_i(m)\left(m + \frac{1}{2} - \langle n \rangle \right)(m+1)\left[N_{\text{th}}\rho_m - (N_{\text{th}}+1)\rho_{m+1}\right] \right]\,.$$

Numerical results for the photon statistics and the Fano factor are given in the next subsection.

5.11.2. Numerical results

In Fig. 5.11 numerical results for the Fano factor F, the photon-number expectation value $\langle n \rangle$, and the recursion coefficient f_n in case of disorder in the mixing angle θ_j and the atomic detuning Δ_j are shown.

The photon-number expectation value $\langle n \rangle$ and the Fano factor F are calculated for $N_{\text{ens}} = 150$ systems consisting of $M = 25$ atoms. The lasing parameters of these systems are randomly generated as follows: As a preliminary step a mixing angle $\bar{\theta}$ in the range $0 < \bar{\theta} \ll \pi/4$ is chosen. The mean detuning be $\overline{\Delta} = 0$, which implies the condition

$$\sqrt{\bar{\delta}^2 + t^2} \overset{!}{=} \omega\,,$$

(a)

(b)

(c)
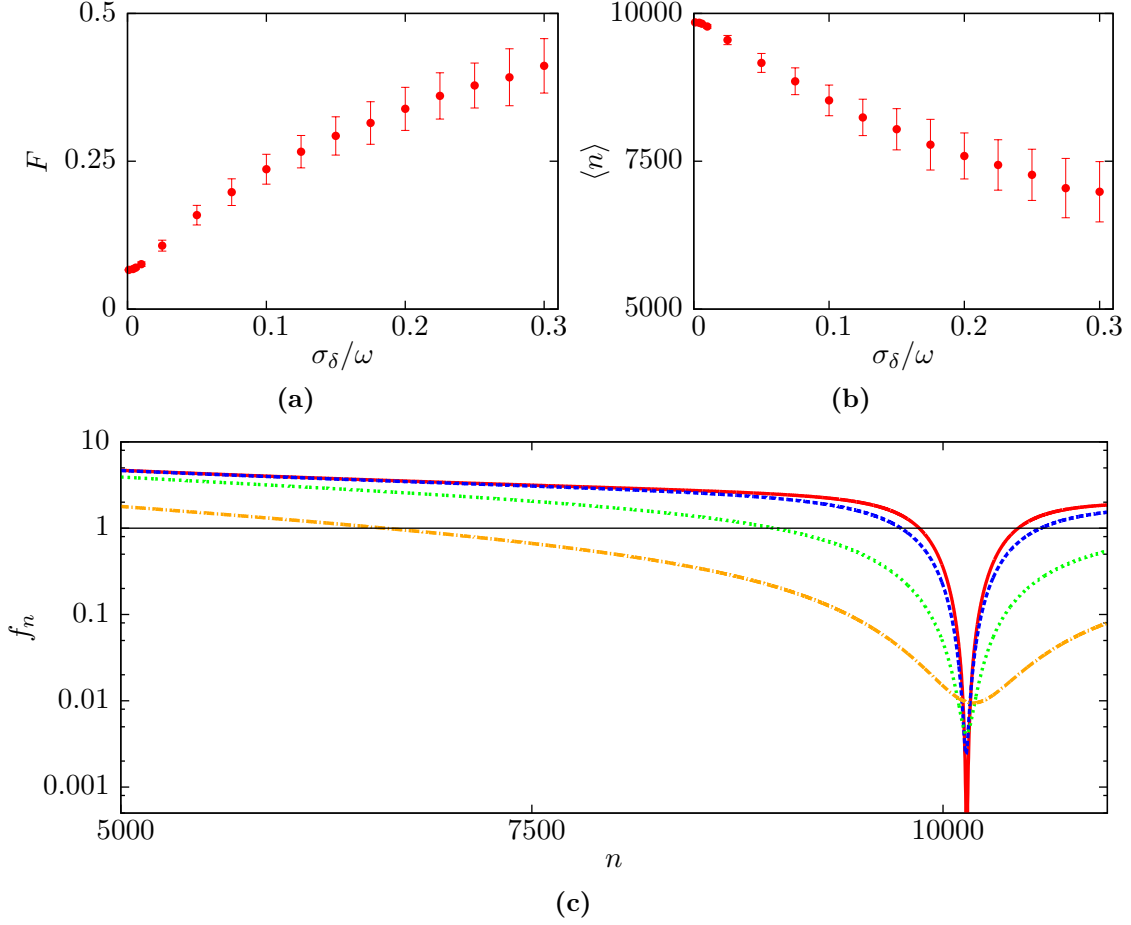
Figure 5.11.: Influence of disorder in the mixing angle θ and the detuning Δ on squeezing. Disorder in the level-splitting energy δ of the bare qubit Hamiltonian (1.2) is modeled by a Gaussian distribution with mean $\overline{\delta} = 0.95\,\omega$ and standard deviation σ_δ. **(a)**: Fano factor F as a function of σ_δ. **(b)**: Photon number expectation value $\langle n \rangle$ as a function of σ_δ. Data was obtained by averaging for each value of σ_δ over $N_{\mathrm{ens}} = 150$ systems. The error bars indicate the standard deviation of the fluctuations. **(c)**: Recursion coefficient f_n for a randomly chosen system (out of N_{ens}) for $\sigma_\delta = 0.001\,\omega$ (solid red), $\sigma_\delta = 0.01\,\omega$ (dashed blue), $\sigma_\delta = 0.1\,\omega$ (dotted green), and $\sigma_\delta = 0.3\,\omega$ (dash-dotted orange curve). Plot parameters are $g = 0.01\,\omega$, $N_{\mathrm{th}} = 0$, $\kappa = 4 \times 10^{-7}\,\omega$, $\Gamma_\uparrow = 0.008\,\omega$, $\Gamma_\downarrow = 0.0001\,\omega$, $\Gamma_\varphi^* = 0.001\,\omega$, $t = 0.31\,\omega$, and $M = 25$.

where δ and t are the parameters of the qubit Hamiltonian (1.2). This condition is solved by $\overline{\delta} = \cos(\overline{\theta})\omega$ and $t = \sin(\overline{\theta})\omega$, which determines the values of $\overline{\delta}$ and t. As discussed in Chap. 4 the range of values of the standard deviation σ_δ of the disorder distribution is restricted by physical constraints. First, the condition $\Delta \geq -\omega$ puts the constraint $\sqrt{\delta^2 + t^2} > 0$ which is, however, always fulfilled. Second, the level splitting energy δ of the qubit Hamiltonian (1.2) should be positive, $\delta \geq 0$. Therefore, Eq. (4.9) restricts the standard deviation to

$$\sigma_g \leq \frac{\overline{\delta}}{\sqrt{2}\,\mathrm{erfc}^{-1}(2\epsilon)} = 0.3\,\omega$$

for $\epsilon = 0.001$ and $\overline{\delta} = 0.95\,\omega$. Now, the level-splitting energy δ_i of each atom i is chosen randomly according to a Gaussian distribution with mean $\overline{\delta}$ and standard deviation σ_δ.

Out of this the individual mixing angle θ_i and the atomic detuning Δ_i are calculated:

$$\theta_i = \arctan\left(-\frac{t}{\delta_i}\right) \quad \text{and} \quad \Delta_i = \frac{\sqrt{\delta_i^2 + t^2}}{\hbar} - \omega\,.$$

In Fig. 5.11a, the Fano factor F as a function of the standard deviation σ_g of the disorder distribution is shown. It increases with the disorder, i.e., disorder in the lasing parameters perturbs photon-number squeezing. However, for the given parameters the photon distribution is still photon-number squeezed even at the maximum allowed value of σ_δ.

Similar to the observations in Sec. 4.2 the photon number expectation value shown in Fig. 5.11b decreases slowly as a function of the standard deviation σ_δ of the disorder distribution. Even at the maximum standard deviation the setup is still operating at approximately 70% of the intensity obtained in an ordered system, whose results are obtained in the limit $\sigma_g \to 0$.

In order to explain these features it is instructive to examine the recursion coefficient f_n for disordered systems. Figure 5.11c shows the recursion coefficient of one randomly chosen system out of the N_{ens} systems calculated for each value of the standard deviation σ_δ of the disorder distribution. The different colors correspond to four different values of σ_g. The plot reveals the following properties of the recursion coefficient f_n in disordered setups:

1. The position of the root of the coupling matrix element of atom i is determined by $p_{0,i} = \frac{g}{\omega}\cos(\theta_i)$. Disorder in the mixing angle θ_i yields different positions of the root for the individual atoms. Therefore, in disordered setups, $\sigma_\delta > 0$, the recursion coefficient f_n does not drop exactly to zero any more. However, the position of its minimum coincides still quite well with the position n_0^i of the root in an ordered system. The reason for this is that the quantity $p_{0,i} \propto \cos(\theta_i) \approx 1 - \theta_i^2$ is robust against small fluctuations in the mixing angle θ_i. Therefore, the roots are only weakly shifted and the recursion coefficient f_n still takes a minimal value at n_0^i that is much smaller than unity. Only for the maximum standard deviation $\sigma_\delta = 0.3\,\omega$ the minimum of f_n in the disordered system differs significantly from the position n_0^i of the root in an ordered system.

2. The range of photon numbers in which f_n drops from the asymptotic value $f_n(\theta/2)$ to its minimal value is significantly broadened by disorder. In Sec. 5.4.2 we showed that the width of the drop region is defined by the condition

$$\left|\langle n-1|\,\tilde{A}_j(\tilde{S}_z^j)\,|n\rangle\right|^2 \ll \frac{\Gamma_1\Gamma_\varphi}{4g^2}\,. \tag{5.46}$$

It implies that the drop region increases if the matrix elements are suppressed: For small mixing angles θ the matrix elements scale proportional to the mixing angle, as described by Eq. (5.10),

$$\langle n-1|\,\tilde{A}_j(\tilde{S}_z^j)\,|n\rangle \propto \theta_j\,.$$

With increasing disorder the amount of atoms with a small mixing angle $\theta_j \ll \bar{\theta}$ increases. The contributions of these atoms to the recursion coefficient f_n broaden the drop region according to Eq. (5.46).

This broadening shifts the maximum of the photon statistics, defined by $f_n = 1$ and $f_n' < 0$, to smaller photon numbers. Therefore, the photon-number expectation value $\langle n\rangle$ decreases. However, the absolute value of the slope of f_n is still larger than the corresponding value for an ordered system with a mixing angle $\theta = \pi/2$, i.e., the photon statistics is still photon-number squeezed.

In conclusion, in the regime of large σ_z couplings, i.e., $\bar{\theta} \ll \pi/4$, the position of the minimum of the recursion coefficient f_n is almost independent of disorder. We observe a decrease of the photon number expectation value $\langle n \rangle$ and an increase of the Fano factor F in disordered systems. These effects are caused by the scaling of the matrix elements proportional to the mixing angle θ and, therefore, a broadening of the drop region of the recursion coefficient f_n around its minimum due to the influence of atoms with a small mixing angle $\theta_i \ll \bar{\theta}$. Although disorder in the mixing angle θ and the detuning Δ increases the Fano factor F, it is still possible to obtain a photon-number squeezed statistics.

6. Conclusion

In this thesis we investigated the influence of disorder and longitudinal couplings on lasing setups that use quantum metamaterials as optically active medium. An advantage of metamaterials built out of artificial atoms is the possibility to tailor the atomic properties. This gives rise to novel interactions with the electromagnetic field and allows for new functionality. In particular we have shown that longitudinal couplings between atoms and the radiation field of a resonator allow for the creation of photon-number squeezed laser light.

Whereas conventional atoms are identical by nature, artificially created atoms, e.g., superconducting circuits or quantum dots, exhibit fluctuations of their individual parameters, for instance, the level splitting energy ϵ, the coupling strength g to a resonator, or the pumping strength D_0. These fluctuations are caused by the fabrication process, noise, and interactions with the environment. If the magnitude of these fluctuations is too large, some artificial atoms are expected not to participate in the lasing process, for instance, because they are too far detuned or too weakly coupled. This may obstruct lasing processes and, therefore, we have investigated the influence of disorder on multi-atom lasing setups. However, we have found that multi-atom lasing setups become robust against disorder when the number of atoms is increased, which opens a way to compensate for inevitable fluctuations of the atomic parameters in quantum metamaterials.

In order to investigate the influence of disorder on a M-atom lasing setup we calculated its photon-number expectation value $\langle n \rangle_M$ using the semiquantum theory of lasing. Disorder in the lasing setup has been modeled by a probability distribution p that describes the spread of the atomic parameters around their intended mean values. We have developed a method to relate the mean photon-number expectation value $\overline{\langle n \rangle}_M$ of a M-atom lasing setup to the mean and the standard deviation of this probability distribution p, and we have applied this method to disorder in the atomic detuning Δ, the coupling strength g, and the pumping strength D_0. Multi-atom lasing setups have been found to be quite robust against these types of disorder. The dependence of the mean photon-number expectation value $\overline{\langle n \rangle}_M$ on the disorder standard deviation for disorder in the detuning and the coupling strength is remarkably weak: Based on the photon-number expectation value $\langle n \rangle_1$ of a single-atom lasing setup one would expect the mean photon-number expectation value $\overline{\langle n \rangle}_M$ of the multi-atom lasing setup to decrease strongly if the standard deviation σ of the disorder distribution increases. For disorder in the pumping strength D_0 the photon-number expectation value $\overline{\langle n \rangle}_M$ is even found to be independent of the standard deviation of the disorder distribution, i.e., it depends only on the mean pumping strength $\overline{D}_0$.

The origin of this robustness against disorder is a widening of the range of parameters that allow for lasing in the multi-atom lasing setup: At a threshold detuning $\Delta_{\max}(1)$ a single-atom laser exhibits a crossover from a lasing state with a large photon-number expectation value to a non-lasing state with a very small photon-number expectation value. In a multi-atom system this threshold detuning $\Delta_{\max}$ is increased, $\Delta_{\max}(M) \geq \Delta_{\max}(1)$,

i.e., the multi-atom lasing system tolerates a larger detuning of each atom than a single-atom laser, while still being in a lasing state. In particular, lasing is observed in a multi-atom setup even if the individual detuning of all atoms is larger than $\Delta_{\max}(1)$. Likewise, there is a minimal coupling strength $g_{\min}(1)$ where the single-atom laser shows a crossover from a non-lasing state to a lasing state. In a multi-atom lasing setup the minimally required coupling strength to the resonator is lowered, $g_{\min}(M) \leq g_{\min}(1)$. Similarly, the lasing-crossover pumping strength $D_{0,\min}$ in a multi-atom lasing setup is lowered compared to the corresponding value of a single-atom laser. For an ordered system explicit expressions for the scaling behavior have been derived, $\Delta_{\max}(M) \propto \sqrt{M}$, $g_{\min}(M) \propto 1/\sqrt{M}$, and $D_{0,\min}(M) \propto 1/M$.

In order to explain the physical origin of this effect we have reformulated the implicit equation defining the photon-number expectation value $\langle n \rangle_M$ of a M-atom setup as a set of coupled equations for the single-atomic contributions $\langle n_i \rangle$, $i \in \{1, \ldots, M\}$, to the overall photon-number expectation value $\langle n \rangle = \sum_{i=1}^{M} \langle n_i \rangle$. The set of coupled equations has to be solved self-consistently. This approach reveals that a collective widening of the range of lasing parameters also takes place in disordered systems. It is caused by an increase of the stimulated emission of each atom i due to the presence of photons in the resonator that are emitted by other atoms $j \neq i$. Therefore, strongly coupled resonant atoms create a nonzero photon number in the resonator that "drags" detuned, weakly coupled, or weakly pumped atoms into resonance such that they participate in the lasing process at a reduced effective detuning and an increased effective coupling and pumping strength. The multi-atom lasing setup evolves into a self-organized stationary state that is quite independent of the initial disordered atomic parameters.

The derivation of the mean photon-number expectation value $\overline{\langle n \rangle}_M$ is exact in the limit of large system sizes $M \to \infty$. However, for realistic system sizes $M \lesssim 100$ deviations of the actual photon-number expectation value $\langle n \rangle_M$ from its mean value $\overline{\langle n \rangle}_M$ are expected, which are caused by sample-to-sample fluctuations of the atomic lasing parameters. Noise and quasistatic fluctuations of the atomic parameters have a similar influence on $\langle n \rangle_M$. We have investigated these fluctuations numerically. Disorder in the detuning at a realistic standard deviation $\sigma_\Delta = 0.2\,\omega$ of the disorder distribution causes relative fluctuations of $\langle n \rangle_M$ around $\overline{\langle n \rangle}_M$ of the order of 10% for small system sizes $M \lesssim 100$. These fluctuations are reduced if the number M of atoms in the metamaterial is increased, and for $M \gtrsim 800$ the relative fluctuations are found to be less than a percent. Hence, a laser built out of a large metamaterial reaches a good long-term power stability even for realistic assumptions on the disorder. This opens a way to build on-chip sources of coherent microwave radiation that have applications in low-temperature experiments. However, it remains still an effort to reach the stability of standard microwave sources even though they also show power fluctuations due to thermal effects, fluctuations of the power-amplifier bias point, or amplification of parasitic signals.

Superconducting circuits or quantum dots have not only a transversal but also a longitudinal coupling to the radiation field. We showed that a strong longitudinal coupling allows for the creation of photon-number squeezed light. Using a polaron transformation we mapped the effective lasing Hamiltonian with both a longitudinal and a transversal coupling between the atoms and the radiation field onto a Tavis-Cummings-like Hamiltonian. In this transformed Hamiltonian the usual coupling operators to the resonator, a and $a^\dagger$, are replaced by more complicated operators that have roots at certain photon numbers and allow for multi-photon transitions. At these roots the coherent emission of photons into the resonator breaks down. The position of the roots can be adjusted via the coupling strength g and the mixing angle θ that defines the relative strength of longitudinal and transversal couplings.

We have shown that if the laser is operated at a photon-number expectation value $\langle n \rangle$

close to a root of the coupling matrix elements, photon-number squeezed light is created. Realistic parameters, e.g., a coupling strength of the order of $1 \times 10^{-3}\,\omega$, allow for strong squeezing, characterized by a Fano factor $F \ll 1$, at large photon numbers, e.g., of the order of 1×10^4.

Numerical methods to examine a squeezed photon statistics of a laser are restricted to rather small photon numbers of the order of 1×10^2. Our analytic approach allows to discuss photon-number squeezing at photon numbers beyond the range of numerical methods.

The coupling operators allow for multi-photon transitions, but in order to obtain a squeezed photon distribution these multi-photon transitions in the pumping process and in the lasing transition have to be suppressed. This is the case if

1. the system has a strong σ_z interaction, i.e., the mixing angle θ is in the range $0 < \theta \lesssim \pi/4$,

2. a rotating wave approximation holds, i.e., all atomic rates $\Gamma_\downarrow$, $\Gamma_\uparrow$, and Γ_φ^* as well as the resonator decay rate κ are much smaller than the resonator frequency ω, and

3. the spectral functions of the pumping and relaxation baths are sufficiently narrowly peaked to suppress multi-photon transitions.

If the first requirement of a strong σ_z interaction is not fulfilled, the laser has a Poissonian photon statistics like a conventional laser as observed in recent experiments [7]. The second requirement holds for typical relaxation and decay rates in superconducting circuits. An experimental setup that allows to fulfill the third requirement has been presented recently [9].

Finally, the influence of disorder in the mixing angle θ and the detuning Δ has been investigated. Such fluctuations arise in quantum metamaterials built out of superconducting qubits because of charge or flux noise. A numerical analysis revealed that the Fano factor increases with increasing disorder, but the photon statistics still remains photon-number squeezed even for large disorder.

A drawback of the studied effective lasing Hamiltonian is the need for a polaron transformation to obtain the Tavis-Cummings-like Hamiltonian with roots of the coupling to the electromagnetic field. The density matrix and the photon statistics are calculated in the polaron frame. However, the photon state $|n\rangle$ in the polaron frame is actually a superposition of different Fock states $|m_\mathrm{c}\rangle$, which represent states with exactly m photons in the resonator cavity. Therefore, the photon statistics in the cavity frame is broadened compared to the one calculated in the polaron frame. This implies that the experimentally relevant Fano factor F in the cavity frame is larger than the Fano factor F_p in the polaron frame. We have found that some corrections to the polaron-frame Fano factor F_p originating from the polaron transformation scale proportional to M^2. For small numbers of atoms, $M \ll 100$, these corrections are negligible. However, for $M \gtrsim 100$ significant corrections arise that can be of the order of unity and spoil photon-number squeezing. In this regime, the photon statistics in the cavity frame has been found to be double-peaked. The photon-number expectation value $\langle n \rangle$ in the cavity frame is also modified by corrections due to the polaron transformation, however, these corrections are negligible for any realistic system size M.

Hence, the polaron transformation imposes for large system sizes M a restriction on the range of lasing parameters that yield a photon-number squeezed statistics. In the near future, experimentally realized quantum metamaterials are expected to have rather small system sizes, $M \ll 100$, and, therefore, are not affected by this restriction. For larger system sizes an improvement can be achieved by using artificial atoms that have roots in the coupling to the electromagnetic field already in the effective lasing Hamiltonian. Such couplings have been discussed, for instance, for a superconducting single-electron transistor

that couples to a resonator via the phase difference across its junction [44] and they are also known for voltage-biased Josephson junctions in series with a resonator [13]. Our calculations apply to these systems as well, but there is no need for a polaron transformation of the initial Hamiltonian any more. Therefore, corrections to the Fano factor due to the polaron transformation do not arise which opens a way to obtain photon-number squeezed light also for quantum metamaterials with a very large number of atoms.

In conclusion, we found that disorder due to imperfections in the control of material parameters does not prohibit the construction of multi-atom lasing setups using quantum metamaterials as active lasing medium. Metamaterials built out of superconducting circuits and quantum dots have longitudinal couplings to the radiation field which allow for the creation of photon-number squeezed light. Our results will help to construct miniaturized on-chip sources for coherent microwave radiation, which have applications in low-temperature experiments, e.g., qubit control or interferometric measurements.

Danksagung

Appendix

A. Influence of the shape of a disorder distribution on the mean photon-number expectation value

Figures 4.2 and 4.3 show that, for disorder in the detuning or the coupling strength, the mean photon-number expectation values $\overline{\langle n \rangle}_M$ obtained for a Gaussian and a box distribution coincide for small values of the standard deviation of the disorder distribution. For a sufficiently narrow disorder distribution the actual shape of the distribution, defined by its higher moments, does not matter and the mean value and the variance are sufficient for characterization. Here we substantiate this observation in the case of disorder in the atomic detuning.

For disorder in the detuning the fixed point equation (4.8) reads

$$\langle n \rangle = N_{\text{th}} + M\beta \int_{-\infty}^{\infty} \mathrm{d}\Delta\, p(\Delta) \frac{D_0 \left(\langle n \rangle + \frac{1}{2} \right) + \frac{1}{2}}{\Gamma_\kappa^2 + \Delta^2 + \alpha \left(\langle n \rangle + \frac{1}{2} \right)} \ .$$

In the case of a large photon-number expectation value $\langle n \rangle$ the right-hand side is expanded into a Taylor polynomial of order N in terms of $\epsilon = 1/\langle n \rangle \ll 1$:

$$\langle n \rangle = N_{\text{th}} + M\beta \int_{-\infty}^{\infty} \mathrm{d}\Delta\, p(\Delta) \left[\frac{D_0}{\alpha} + \sum_{m=1}^{N} c_m \frac{1}{\langle n \rangle^m} + R_N(n) \right] \ ,$$

$$c_m = (-1)^m \frac{\left(\Gamma_\kappa^2 + \Delta^2 + \frac{\alpha}{2} \right)^{m-1}}{\alpha^{m+1}} \left(D_0 \left(\Gamma_\kappa^2 + \Delta^2 \right) - \frac{\alpha}{2} \right) \ ,$$

where the rest term $R_N(n)$ is bounded by the upper limit

$$|R_N(n)| \leq D_0 \frac{\left(\Gamma_\kappa^2 + \frac{\alpha}{2} + \Delta^2 \right)^m}{(\alpha n)^{m+1}} \left| \Gamma_\kappa^2 + \Delta^2 - \frac{\alpha}{2D_0} \right| \ .$$

We now perform the integration term by term and obtain

$$\langle n \rangle = M\beta \left[\frac{D_0}{\alpha} \right.$$
$$+ \sum_{m=1}^{\infty} \frac{(-1)^m}{\alpha^m} \frac{1}{\langle n \rangle^m} \left(\frac{D_0}{\alpha} \sum_{k=0}^{m} \binom{m}{k} \left(\Gamma_\kappa^2 + \frac{\alpha}{2} \right)^{m-k} \overline{\Delta^{2k}} \right.$$
$$\left. \left. - \frac{D_0 + 1}{2} \sum_{k=0}^{m-1} \binom{m-1}{k} \left(\Gamma_\kappa^2 + \frac{\alpha}{2} \right)^{m-1-k} \overline{\Delta^{2k}} \right) \right]$$
$$+ N_{\text{th}} + \overline{R}_N(n) \ , \tag{A.1}$$

where the moments of the probability distribution p are denoted by $\overline{\Delta^{2k}} = \int_{-\infty}^{\infty} \mathrm{d}\Delta\, p(\Delta)\Delta^{2k}$ and the averaged rest term is given by $\overline{R}_N(n) = M\beta \int_{-\infty}^{\infty} \mathrm{d}\Delta\, p(\Delta) R_N(n)$. The Taylor

expansion converges for photon-number expectation values fulfilling $\langle n \rangle > \frac{1}{2} + (\Gamma_\kappa^2 + \Delta^2)/\alpha$. Hence, if $p(\Delta)$ has a compact support $[-a, a]$, $a > 0$, the rest term $R_N(n)$ vanishes in the limit $N \to \infty$ for all photon numbers that satisfy the condition $\langle n \rangle > \frac{1}{2} + (\Gamma_\kappa^2 + a^2)/\alpha$. This applies for a box distribution, whereas a Gaussian distribution has support $(-\infty, \infty)$ and, therefore, the expansion never converges. However, if the order N of the Taylor expansion is chosen suitably, the rest term $\overline{R}_N(n)$ takes a minimal value much smaller than unity so that the expansion is still a good approximation.

The properties of the probability distribution $p(\Delta)$ enter into Eq. (A.1) through its even moments $\overline{\Delta^{2k}}$. For a given probability distribution these moments can be expressed by polynomials of the mean value μ, the standard deviation σ, and other parameters of the distribution. As all lasing parameters are much smaller than the frequency ω, higher order terms of these polynomials can be neglected because it holds $\mu/\omega \ll 1$ and $\sigma/\omega \ll 1$. Therefore, two probability distributions yield the same results for the mean photon-number expectation value $\overline{\langle n \rangle}_M$ if their moments are identical to low orders of μ and σ.

B. Properties of the polaron transformation

B.1. Transformation rules

In this section we give the transformation properties of the Pauli matrices and the photon creation and annihilation operators under a polaron transformation of the form

$$U = \exp \left[i \sum_{j=1}^{M} p_j \sigma_z^j \right] ,$$

$$p_j = i p_{0,j} \left(a^\dagger - a \right) = i \frac{g}{\omega} \cos(\theta_j) \left(a^\dagger - a \right) .$$

The field operators transform as follows:

$$a_{\mathrm{p}} = U^\dagger a U = a - \sum_{i=1}^{M} p_{0,i} \sigma_z^i ,$$

$$a_{\mathrm{p}}^\dagger = U^\dagger a^\dagger U = a^\dagger - \sum_{i=1}^{M} p_{0,i} \sigma_z^i ,$$

$$a_{\mathrm{p}}^\dagger a_{\mathrm{p}} = U^\dagger a^\dagger a U = a^\dagger a - \sum_{i=1}^{M} p_{0,i} \sigma_z^i \left(a + a^\dagger \right) + \sum_{i=1}^{M} p_{0,i}^2 + \sum_{i \neq j=1}^{M} p_{0,i} p_{0,j} \sigma_z^i \sigma_z^j .$$

For the third Pauli matrix and the atomic ladder operators we have

$$\sigma_{z,\mathrm{p}}^j = U^\dagger \sigma_z^j U = \sigma_z^j ,$$

$$\sigma_{+,\mathrm{p}}^j = U^\dagger \sigma_+^j U = \sigma_+^j e^{-2ip_j} ,$$

$$\sigma_{-,\mathrm{p}}^j = U^\dagger \sigma_-^j U = \sigma_-^j e^{2ip_j} .$$

B.2. Expansion of a polaron state into cavity states

In this section we calculate the expansion of a polaron-frame state $|\boldsymbol{\sigma}, n\rangle \equiv |\boldsymbol{\sigma}\rangle \otimes |n\rangle$ into states in the cavity frame, $|\boldsymbol{\sigma}, m_{\mathrm{c}}\rangle \equiv |\boldsymbol{\sigma}\rangle \otimes |m_{\mathrm{c}}\rangle$. The states of the M atoms are denoted by the vector $\boldsymbol{\sigma} = (\sigma_z^1, \ldots, \sigma_z^M)$. Polaron and cavity states are connected via a polaron transformation,

$$|\boldsymbol{\sigma}, n\rangle = U^\dagger |\boldsymbol{\sigma}, n_{\mathrm{c}}\rangle ,$$

$$U = \exp \left[\sum_{j=1}^{M} p_{0,j} \sigma_z^j \left(a - a^\dagger \right) \right] ,$$

which is essentially a displacement operator

$$U = D(\alpha) = \exp\left[\alpha a^\dagger - \alpha^* a\right],$$

with the displacement parameter $\alpha(\boldsymbol{\sigma}) = \alpha^*(\boldsymbol{\sigma}) = -\sum_{j=1}^M p_{0,j}\sigma_z^j$. It holds $U^\dagger = D(-\alpha)$. The expansion of the polaron-frame state $|\boldsymbol{\sigma}, n\rangle$ into cavity states $|\boldsymbol{\sigma}, m_c\rangle$ is formally given by

$$|\boldsymbol{\sigma}, n\rangle = \sum_{m=0}^\infty a_{n,m}(\boldsymbol{\sigma}) |\boldsymbol{\sigma}, m_c\rangle,$$

$$a_{n,m}(\boldsymbol{\sigma}) = \langle\boldsymbol{\sigma}, m| D(-\alpha(\boldsymbol{\sigma})) |\boldsymbol{\sigma}, n\rangle.$$

In order to calculate the expansion coefficient $a_{n,m}(\boldsymbol{\sigma})$ we use the following representation of the state $|n\rangle$ in the polaron frame:

$$|n\rangle = \frac{(a^\dagger)^n}{\sqrt{n!}} |0\rangle = \frac{1}{\sqrt{n!}} \frac{\mathrm{d}^n}{\mathrm{d}\lambda^n} e^{\lambda a^\dagger}\bigg|_{\lambda=0} |0\rangle.$$

As a preliminary step we calculate the action of the displacement operator $D(\beta)$ on a state $e^{\lambda a^\dagger} |0\rangle$,

$$D(\beta)e^{\lambda a^\dagger} |0\rangle = e^{-|\beta|^2/2 - \beta^*\lambda + |\beta+\lambda|^2/2} |\beta + \lambda\rangle,$$

which yields the following matrix element:

$$\langle m| D(\beta)e^{\lambda a^\dagger} |0\rangle = e^{-|\beta|^2/2 - \beta^*\lambda} \frac{(\beta + \lambda)^m}{\sqrt{m!}}.$$

The matrix element $\langle m| D(\beta) |n\rangle$ of the displacement operator is connected to this via

$$\langle m| D(\beta) |n\rangle = \frac{1}{\sqrt{n!m!}} e^{-|\beta|^2/2} \frac{\mathrm{d}^n}{\mathrm{d}\lambda^n} e^{-\beta^*\lambda}(\beta + \lambda)^m\bigg|_{\lambda=0}.$$

By complete induction one can proof the identity

$$\frac{\mathrm{d}^n}{\mathrm{d}\lambda^n} e^{-\beta^*\lambda}(\beta + \lambda)^m = \sum_{k=0}^\infty (-1)^{n+k}\binom{n}{k}\frac{m!}{(m-k)!}(\beta + \lambda)^{m-k}(\beta^*)^{n-k}e^{-\beta^*\lambda}\Theta(m - k),$$

where $\binom{n}{k}$ is a binomial coefficient and $\Theta(x)$ is the Heaviside step function, which is equal to unity for $x \geq 0$ and zero otherwise. With this result we obtain

$$\langle m| D(\beta) |n\rangle = \frac{1}{\sqrt{n!m!}} e^{-|\beta|^2/2} \sum_{k=0}^n (-1)^{n+k}\binom{n}{k}\frac{m!}{(m-k)!}\beta^{m-k}(\beta^*)^{n-k}\Theta(m - k)$$

$$= \frac{1}{\sqrt{n!m!}} e^{-|\beta|^2/2}(-1)^n(\beta^*)^{n-m}\, \mathrm{U}(-m, 1 - m + n, |\beta|^2),$$

where $U(a, b, x)$ is the hypergeometric function of the second kind.

For $\beta = -\alpha(\boldsymbol{\sigma}) = -\alpha^*(\boldsymbol{\sigma})$ we finally obtain the expansion coefficient $a_{n,m}(\boldsymbol{\sigma})$:

$$a_{n,m}(\boldsymbol{\sigma}) = \frac{1}{\sqrt{n!m!}} e^{-|\alpha|^2/2} \sum_{k=0}^n (-1)^{n+k}\binom{n}{k}\frac{m!}{(m-k)!}(-\alpha)^{m+n-2k}\Theta(m - k).$$

C. Calculating traces of the quantum master equation

The density matrix ρ is the most general way to describe the state of a quantum-mechanical system. If only information of a certain subsystem is required, a reduced density matrix for this subsystem is obtained by tracing out all degrees of freedom that do not belong to that subsystem. Analogously, by tracing out certain degrees of freedom in the quantum master equation of the density matrix ρ an equation of motion for the reduced density matrix is obtained. In this section we discuss the behavior of the coherent Liouville term and the Lindblad terms under such tracing operations. The time evolution of the full density matrix ρ is given by the following quantum master equation:

$$\frac{\mathrm{d}}{\mathrm{d}t}\rho = -\frac{i}{\hbar}\left[H,\rho\right] + L_{\mathrm{R}}\rho + \sum_{j=1}^{M} L_{\mathrm{Q},j}\rho \,,$$

where the coherent M-atom Hamiltonian H and the Lindblad superoperators are given by

$$H = H_{\mathrm{res}} + \sum_{j=1}^{M} H_{\mathrm{at}}^{j} + \sum_{j=1}^{M} H_{\mathrm{int}}^{j}\,,$$

$$L_{\mathrm{R}}\rho = \frac{\kappa}{2}(N_{\mathrm{th}}+1)\left(2a\rho a^{\dagger} - a^{\dagger}a\rho - \rho a^{\dagger}a\right) + \frac{\kappa}{2}N_{\mathrm{th}}\left(2a^{\dagger}\rho a - aa^{\dagger}\rho - \rho aa^{\dagger}\right)\,,$$

$$L_{\mathrm{Q},j}\rho = \frac{\Gamma_{\downarrow}}{2}\left(2\sigma_{-}^{j}\rho\sigma_{+}^{j} - \rho\sigma_{+}^{j}\sigma_{-}^{j} - \sigma_{+}^{j}\sigma_{-}^{j}\rho\right) + \frac{\Gamma_{\uparrow}}{2}\left(2\sigma_{+}^{j}\rho\sigma_{-}^{j} - \rho\sigma_{-}^{j}\sigma_{+}^{j} - \sigma_{-}^{j}\sigma_{+}^{j}\rho\right)$$
$$+ \frac{\Gamma_{\varphi}^{*}}{2}\left(\sigma_{z}^{j}\rho\sigma_{z}^{j} - \rho\right)\,.$$

Here H_{res} is the Hamiltonian of the resonator, H_{at}^{j} is the Hamiltonian of atom j, $j = 1,\ldots,M$, and H_{int}^{j} is the interaction of atom j with the resonator.

The state of the M atoms is denoted by the vector $\boldsymbol{\sigma} = (\sigma_{z}^{1},\ldots,\sigma_{z}^{M})$ and the state of $M-1$ atoms except of atom k is denoted by $\boldsymbol{\sigma}_{k}' = (\sigma_{z}^{1},\ldots,\sigma_{z}^{k-1},\sigma_{z}^{k+1},\ldots,\sigma_{z}^{M})$. In the following we are interested in the reduced density matrix of the resonator, ρ^{res}, and the reduced density matrix of the resonator and atom k, $\rho^{k,\mathrm{res}}$, which are defined by

$$\rho^{\mathrm{res}} = \mathrm{Tr}_{\boldsymbol{\sigma}}(\rho) = \sum_{\boldsymbol{\sigma}} \langle\boldsymbol{\sigma}|\,\rho\,|\boldsymbol{\sigma}\rangle\,,$$

$$\rho^{k,\mathrm{res}} = \mathrm{Tr}_{\boldsymbol{\sigma}_{k}'}(\rho) = \sum_{\boldsymbol{\sigma}_{k}'} \langle\boldsymbol{\sigma}_{k}'|\,\rho\,|\boldsymbol{\sigma}_{k}'\rangle\,.$$

C.1. Reduced density matrix of the resonator

If all atomic states are traced out, the different terms of the master equation yield

$$\mathrm{Tr}_{\boldsymbol{\sigma}}\left(\left[H_{\mathrm{at}}^{j},\rho\right]\right) = \sum_{\boldsymbol{\sigma}} \langle\boldsymbol{\sigma}|\left[H_{\mathrm{at}}^{j},\rho\right]|\boldsymbol{\sigma}\rangle = \sum_{\boldsymbol{\sigma}}(E(\sigma_{j}) - E(\sigma_{j}))\,\langle\boldsymbol{\sigma}|\,\rho\,|\boldsymbol{\sigma}\rangle = 0\,,$$

$$\mathrm{Tr}_{\boldsymbol{\sigma}}\left([H_{\mathrm{res}},\rho]\right) = \sum_{\boldsymbol{\sigma}} \langle\boldsymbol{\sigma}|\,[H_{\mathrm{res}},\rho]\,|\boldsymbol{\sigma}\rangle = \sum_{\boldsymbol{\sigma}} [H_{\mathrm{res}},\langle\boldsymbol{\sigma}|\,\rho\,|\boldsymbol{\sigma}\rangle] = [H_{\mathrm{res}},\rho^{\mathrm{res}}]\,,$$

$$\mathrm{Tr}_{\boldsymbol{\sigma}}\left(\left[H_{\mathrm{int}}^{j},\rho\right]\right) = \sum_{\boldsymbol{\sigma}} \langle\boldsymbol{\sigma}|\left[H_{\mathrm{int}}^{j},\rho\right]|\boldsymbol{\sigma}\rangle = \sum_{\sigma_{z}^{j}} \left\langle\sigma_{z}^{j}\right|\left[H_{\mathrm{int}}^{j},\rho^{j,\mathrm{res}}\right]\left|\sigma_{z}^{j}\right\rangle\,,$$

$$\mathrm{Tr}_{\boldsymbol{\sigma}}\left(L_{\mathrm{Q},j}\rho\right) = \sum_{\sigma_{z}^{j}} \left\langle\sigma_{z}^{j}\right| L_{\mathrm{Q},j}\rho^{j,\mathrm{res}} \left|\sigma_{z}^{j}\right\rangle$$
$$= \sum_{\sigma_{z}^{j}} \left(\Gamma_{\downarrow}\langle\uparrow|\,\rho^{j,\mathrm{res}}\,|\uparrow\rangle\left(\delta_{\sigma_{z}^{j},\downarrow} - \delta_{\sigma_{z}^{j},\uparrow}\right) + \Gamma_{\uparrow}\langle\downarrow|\,\rho^{j,\mathrm{res}}\,|\downarrow\rangle\left(\delta_{\sigma_{z}^{j},\uparrow} - \delta_{\sigma_{z}^{j},\downarrow}\right)\right) = 0\,,$$

$$\mathrm{Tr}_{\boldsymbol{\sigma}}\left(L_{\mathrm{R}}\rho\right) = L_{\mathrm{R}}\rho^{\mathrm{res}}\,.$$

Therefore, the reduced density matrix of the resonator has the following equation of motion:

$$\frac{\mathrm{d}}{\mathrm{d}t}\rho^{\mathrm{res}} = -\frac{i}{\hbar}\left[H_{\mathrm{res}}, \rho^{\mathrm{res}}\right] - \frac{i}{\hbar}\sum_{j=1}^{M}\sum_{\sigma_z^j}\left\langle\sigma_z^j\right|\left[H_{\mathrm{int}}^j, \rho^{j,\mathrm{res}}\right]\left|\sigma_z^j\right\rangle + L_{\mathrm{R}}\rho^{\mathrm{res}}\,.$$

C.2. Reduced density matrix of one atom and the resonator

Similarly, if all atomic states but one are traced out, we obtain

$$\mathrm{Tr}_{\boldsymbol{\sigma}_k'}\left(\left[H_{\mathrm{at}}^j, \rho\right]\right) = \sum_{\boldsymbol{\sigma}_k'}\left\langle\boldsymbol{\sigma}_k'\right|\left[H_{\mathrm{at}}^j, \rho\right]\left|\boldsymbol{\sigma}_k'\right\rangle = \sum_{\boldsymbol{\sigma}_k'}\left[H_{\mathrm{at}}^j, \left\langle\boldsymbol{\sigma}_j'\right|\rho\left|\boldsymbol{\sigma}_j'\right\rangle\right]\delta_{j,k} = \left[H_{\mathrm{at}}^j, \rho^{j,\mathrm{res}}\right]\delta_{j,k}\,,$$

$$\mathrm{Tr}_{\boldsymbol{\sigma}_k'}\left(\left[H_{\mathrm{res}}, \rho\right]\right) = \sum_{\boldsymbol{\sigma}_k'}\left\langle\boldsymbol{\sigma}_k'\right|\left[H_{\mathrm{res}}, \rho\right]\left|\boldsymbol{\sigma}_k'\right\rangle = \sum_{\boldsymbol{\sigma}_k'}\left[H_{\mathrm{res}}, \left\langle\boldsymbol{\sigma}_k'\right|\rho\left|\boldsymbol{\sigma}_k'\right\rangle\right] = \left[H_{\mathrm{res}}, \rho^{k,\mathrm{res}}\right]\,,$$

$$\mathrm{Tr}_{\boldsymbol{\sigma}_k'}\left(L_{\mathrm{Q},j}\rho\right) = \sum_{\boldsymbol{\sigma}_k'}\left\langle\boldsymbol{\sigma}_k'\right|L_{\mathrm{Q},j}\rho\left|\boldsymbol{\sigma}_k'\right\rangle = L_{\mathrm{Q},j}\rho^{j,\mathrm{res}}\delta_{j,k}\,,$$

$$\mathrm{Tr}_{\boldsymbol{\sigma}_k'}\left(L_{\mathrm{R}}\rho\right) = L_{\mathrm{R}}\rho^{k,\mathrm{res}}\,.$$

The trace of the interaction term is more complicated. For an interaction of the form $H_{\mathrm{int}}^j = \hbar g(\sigma_+^j A + \sigma_-^j A^\dagger)$ we obtain for $k = j$

$$\mathrm{Tr}_{\boldsymbol{\sigma}_j'}\left(\left[H_{\mathrm{int}}^j, \rho\right]\right) = \sum_{\boldsymbol{\sigma}_j'}\left\langle\boldsymbol{\sigma}_j'\right|\left[H_{\mathrm{int}}^j, \rho\right]\left|\boldsymbol{\sigma}_j'\right\rangle = \left[H_{\mathrm{int}}^j, \rho^{j,\mathrm{res}}\right]\,.$$

However, for $k \neq j$ the interaction Hamiltonian yields

$$\mathrm{Tr}_{\boldsymbol{\sigma}_k'}\left(\left[H_{\mathrm{int}}^j, \rho\right]\right) = \hbar g\sum_{\sigma_j}\left\langle\sigma_j\right|\left[H_{\mathrm{int}}^j, \rho^{j,k,\mathrm{res}}\right]\left|\sigma_j\right\rangle$$

$$= \hbar g\Big(\quad A\left\langle\downarrow_j\right|\rho^{j,k,\mathrm{res}}\left|\uparrow_j\right\rangle + A^\dagger\left\langle\uparrow_j\right|\rho^{j,k,\mathrm{res}}\left|\downarrow_j\right\rangle$$

$$- \left\langle\downarrow_j\right|\rho^{j,k,\mathrm{res}}\left|\uparrow_j\right\rangle A - \left\langle\uparrow_j\right|\rho^{j,k,\mathrm{res}}\left|\downarrow_j\right\rangle A^\dagger\Big)\,,$$

where $\rho^{j,k,\mathrm{res}}$ is the reduced density matrix for the resonator and the atoms j and k. Therefore, we obtain the following equation of motion for the reduced density matrix of atom k and the resonator:

$$\frac{\mathrm{d}}{\mathrm{d}t}\rho^{k,\mathrm{res}} = -\frac{i}{\hbar}\left[H_{\mathrm{at}}^k + H_{\mathrm{res}} + H_{\mathrm{int}}^k, \rho^{k,\mathrm{res}}\right] + L_{\mathrm{Q},k}\rho^{k,\mathrm{res}} + L_{\mathrm{R}}\rho^{k,\mathrm{res}} - \frac{i}{\hbar}\sum_{\substack{j\neq k\\j=1}}^{M}\mathrm{Tr}_{\boldsymbol{\sigma}_k'}\left(\left[H_{\mathrm{int}}^j, \rho\right]\right)\,.$$

$$(\mathrm{C.1})$$

We neglect the term $\mathrm{Tr}_{\boldsymbol{\sigma}_k'}\left(\left[H_{\mathrm{int}}^j, \rho\right]\right)$ for $j \neq k$ and the resonator Lindblad term $L_{\mathrm{R}}\rho^{k,\mathrm{res}}$ by using that

1. all M qubits are independent, i.e., there are no correlations between different qubits, and

2. an adiabatic approximation holds for typical lasing parameters.

To justify this step we consider the contribution of $\mathrm{Tr}_{\boldsymbol{\sigma}_k'}\left(\left[H_{\mathrm{int}}^j, \rho\right]\right)$ to the equations of motion of the matrix elements $\rho_{\sigma,n;\sigma,n}$, $\rho_{\uparrow,n;\downarrow,n+1}$, and $\rho_{\downarrow,n+1;\uparrow,n}$. These matrix elements are subsumed in the vector $\boldsymbol{R}$ during the calculation of photon statistics in Sec. 5.4. If only energy-conserving transitions are considered, we obtain the following contributions:

$$\frac{\mathrm{d}}{\mathrm{d}t}\rho_{\sigma,n;\sigma,n}^{k,\mathrm{res}} \propto \hbar g\Big(\quad\left\langle n\right|A\left|n+1\right\rangle\rho_{\sigma_k,\downarrow_j,n+1;\sigma_k,\uparrow_j,n} + \left\langle n\right|A^\dagger\left|n-1\right\rangle\rho_{\sigma_k,\uparrow_j,n-1;\sigma_k,\downarrow_j,n}$$

$$-\rho_{\sigma_k,\downarrow_j n;\sigma_k,\uparrow_j,n-1}\left\langle n-1\right|A\left|n\right\rangle - \rho_{\sigma_k,\uparrow_j,n;\sigma_k,\downarrow_j,n+1}\left\langle n+1\right|A^\dagger\left|n\right\rangle\Big)\,,$$

$$(\mathrm{C.2a})$$

$$\frac{\mathrm{d}}{\mathrm{d}t}\rho_{\uparrow,n;\downarrow,n+1}^{k,\mathrm{res}} \propto \hbar g\Big(\quad \langle n|\,A\,|n+1\rangle\,\rho_{\uparrow_k,\downarrow_j,n+1;\downarrow_k,\uparrow_j,n+1} + \langle n|\,A^\dagger\,|n-1\rangle\,\rho_{\uparrow_k,\uparrow_j,n-1;\downarrow_k,\downarrow_j,n+1}$$
$$-\rho_{\uparrow_k,\downarrow_j,n;\downarrow_k,\uparrow_j,n}\,\langle n|\,A\,|n+1\rangle - \rho_{\uparrow_k,\uparrow_j,n;\downarrow_k,\downarrow_j,n+2}\,\langle n+2|\,A^\dagger\,|n+1\rangle\Big)$$
$$= 0\,, \tag{C.2b}$$

$$\frac{\mathrm{d}}{\mathrm{d}t}\rho_{\downarrow,n+1;\uparrow,n}^{k,\mathrm{res}} \propto \hbar g\Big(\quad \langle n+1|\,A\,|n+2\rangle\,\rho_{\downarrow_k,\downarrow_j,n+2;\uparrow_k,\uparrow_j,n} + \langle n+1|\,A^\dagger\,|n\rangle\,\rho_{\downarrow_k,\uparrow_j,n;\uparrow_k,\downarrow_j,n}$$
$$-\rho_{\downarrow_k,\downarrow_j,n+1;\uparrow_k,\uparrow_j,n-1}\,\langle n-1|\,A\,|n\rangle - \rho_{\downarrow_k,\uparrow_j,n+1;\uparrow_k,\downarrow_j,n+1}\,\langle n+1|\,A^\dagger\,|n\rangle\Big)$$
$$= 0\,. \tag{C.2c}$$

For the sake of a compact notation the superscript "k,j,res" has been dropped at the density matrix elements on the right-hand side. Equations (C.2b) and (C.2c) are zero because the occurring density matrix elements describe correlations between the atoms k and j. These matrix elements vanish as all M atoms are independent of each other. However, the contributions to the equation of motion given by Eq. (C.2a) are nonzero. The assumption of independent atoms allows to rewrite the occurring matrix elements as follows:

$$\rho_{\sigma_k,\sigma_j,n;\sigma_k,\sigma_j',n'} = \rho_{\sigma_k,\sigma_k} \otimes \rho_{\sigma_j,n;\sigma_j',n'}\,.$$

Now we obtain

$$\frac{\mathrm{d}}{\mathrm{d}t}\rho_{\sigma,n;\sigma,n}^{k,\mathrm{res}} \propto \hbar g\rho_{\sigma_k,\sigma_k} \otimes \Big(\quad \langle n|\,A\,|n+1\rangle\,\rho_{\downarrow_j,n+1;\uparrow_j,n} + \langle n|\,A^\dagger\,|n-1\rangle\,\rho_{\uparrow_j,n-1;\downarrow_j,n}$$
$$-\rho_{\downarrow_j,n;\uparrow_j,n-1}\,\langle n-1|\,A\,|n\rangle - \rho_{\uparrow_j,n;\downarrow_j,n+1}\,\langle n+1|\,A^\dagger\,|n\rangle\Big)\,.$$

The terms in round brackets are evaluated using Eq. (5.14). We find that they only introduce a phase change,

$$\frac{\mathrm{d}}{\mathrm{d}t}\rho_{\sigma,n;\sigma,n}^{k,\mathrm{res}} \propto 2i\hbar g^2\Gamma_1\Gamma_\varphi\rho_{\sigma_k,\sigma_k} \otimes \Bigg[\quad \Gamma_\uparrow\left(\frac{|\langle n-1|\,A\,|n\rangle|^2}{\det M_{n-1,n-1}}\rho_{n-1,n-1}^{\mathrm{res}} - \frac{|\langle n|\,A\,|n+1\rangle|^2}{|M_{n,n}|}\rho_{n,n}\right)$$
$$-\Gamma_\downarrow\left(\frac{|\langle n-1|\,A\,|n\rangle|^2}{\det M_{n-1,n-1}}\rho_{n,n}^{\mathrm{res}} - \frac{|\langle n|\,A\,|n+1\rangle|^2}{|M_{n,n}|}\rho_{n+1,n+1}\right)\Bigg]$$
$$= i\left[\gamma_1\rho_{\sigma,n-1;\sigma,n-1}^{k,\mathrm{res}} + \gamma_2\rho_{\sigma,n;\sigma,n}^{k,\mathrm{res}} + \gamma_3\rho_{\sigma,n+1;\sigma,n+1}^{k,\mathrm{res}}\right]\,.$$

A numerical evaluation reveals that the rates γ_1, γ_2, and γ_3 are of the order of the resonator decay rate κ.

This allows to apply an adiabatic approximation: The atomic Lindblad term $L_{\mathrm{Q},k}\rho^{k,\mathrm{res}}$ in Eq. (C.1) describes atomic decay processes that happen on a timescale of $\Gamma_\uparrow^{-1}$, $\Gamma_\downarrow^{-1}$, and $(\Gamma_\varphi^*)^{-1}$. The resonator Lindblad term $L_{\mathrm{R}}\rho^{k,\mathrm{res}}$ and the interaction term $\mathrm{Tr}_{\sigma_k'}\left(\left[H_{\mathrm{int}}^j,\rho\right]\right)$ for $j \neq k$ describe decay processes and phase changes that happen on a timescale of κ^{-1}. For typical lasing parameters it holds $\kappa \ll \Gamma_\uparrow,\Gamma_\downarrow,\Gamma_\varphi^*$ and, therefore, we neglect these processes in the master equation (C.1) focusing only on atomic decay processes.

In conclusion, the reduced density matrix for the resonator and the atom k has the following equation of motion:

$$\frac{\mathrm{d}}{\mathrm{d}t}\rho^{k,\mathrm{res}} = -\frac{i}{\hbar}\left[H_{\mathrm{at}}^k + H_{\mathrm{res}} + H_{\mathrm{int}}^k, \rho^{k,\mathrm{res}}\right] + L_{\mathrm{Q},k}\rho^{k,\mathrm{res}}\,.$$

Bibliography

[1] C. H. Townes. *Obituary: Theodore H. Maiman (1927-2007)*. Nature **447**(7145), 654 (2007).
URL http://dx.doi.org/10.1038/447654a

[2] W. E. Lamb, W. P. Schleich, M. O. Scully, and C. H. Townes. *Laser physics: Quantum controversy in action*. Rev. Mod. Phys. **71**, S263 (1999).
URL http://dx.doi.org/10.1103/RevModPhys.71.S263

[3] H. Haken. *Licht und Materie*, volume 2: Laser. Bibliograph. Inst., Mannheim, 1st edition (1981). ISBN 3-411-01589-6.

[4] T. H. Maiman. *Stimulated optical radiation in ruby*. Nature **187**, 493 (1960).
URL http://dx.doi.org/10.1038/187493a0

[5] G. H. B. Thompson. *Physics of semiconductor laser devices*. Wiley, Chichester (1980). ISBN 0-471-27685-5.

[6] O. Astafiev, K. Inomata, A. O. Niskanen, T. Yamamoto, Y. A. Pashkin, Y. Nakamura, and J. S. Tsai. *Single artificial-atom lasing*. Nature **449**(7162), 588 (2007).
URL http://dx.doi.org/10.1038/nature06141

[7] Y.-Y. Liu, J. Stehlik, C. Eichler, M. Gullans, J. Taylor, and J. Petta. *Semiconductor double quantum dot micromaser*. Science **347**(6219), 285 (2015).
URL http://dx.doi.org/10.1126/science.aaa2501

[8] F. Chen, J. Li, A. D. Armour, E. Brahimi, J. Stettenheim, A. J. Sirois, R. W. Simmonds, M. P. Blencowe, and A. J. Rimberg. *Realization of a single-Cooper-pair Josephson laser*. Phys. Rev. B **90**, 020506 (2014).
URL http://dx.doi.org/10.1103/PhysRevB.90.020506

[9] Z. H. Peng, Y.-X. Liu, J. T. Peltonen, T. Yamamoto, J. S. Tsai, and O. Astafiev. *Correlated emission lasing in harmonic oscillators coupled via a single three-level artificial atom*. Phys. Rev. Lett. **115**, 223603 (2015).
URL http://dx.doi.org/10.1103/PhysRevLett.115.223603

[10] N. I. Zheludev. *The Road Ahead for Metamaterials*. Science **328**, 582 (2010).

[11] M. Hofheinz, F. Portier, Q. Baudouin, P. Joyez, D. Vion, P. Bertet, P. Roche, and D. Esteve. *Bright side of the Coulomb blockade*. Phys. Rev. Lett. **106**, 217005 (2011).
URL http://dx.doi.org/10.1103/PhysRevLett.106.217005

[12] S. André, L. Guo, V. Peano, M. Marthaler, and G. Schön. *Emission spectrum of the driven nonlinear oscillator*. Phys. Rev. A **85**, 053825 (2012).
URL http://dx.doi.org/10.1103/PhysRevA.85.053825

[13] V. Gramich, B. Kubala, S. Rohrer, and J. Ankerhold. *From Coulomb-blockade to nonlinear quantum dynamics in a superconducting circuit with a resonator*. Phys.

Rev. Lett. **111**, 247002 (2013).
URL http://dx.doi.org/10.1103/PhysRevLett.111.247002

[14] P. Macha, G. Oelsner, J.-M. Reiner, M. Marthaler, S. André, G. Schön, U. Hübner, H.-G. Meyer, E. Il'ichev, and A. V. Ustinov. *Implementation of a quantum metamaterial using superconducting qubits.* Nat. Commun. **5**, 5146 (2014).
URL http://dx.doi.org/10.1038/ncomms6146

[15] M. H. Devoret, A. Wallraff, and J. M. Martinis. *Superconducting qubits: A short review.* arXiv (2004).
URL http://arxiv.org/abs/cond-mat/0411174

[16] T. P. Orlando, J. E. Mooij, L. Tian, C. H. van der Wal, L. S. Levitov, S. Lloyd, and J. J. Mazo. *Superconducting persistent-current qubit.* Phys. Rev. B **60**, 15398 (1999).
URL http://dx.doi.org/10.1103/PhysRevB.60.15398

[17] M. O. Scully and M. S. Zubairy. *Quantum optics.* Cambridge Univ. Press, Cambridge, repr. edition (1999). ISBN 978-0-521-43595-6.

[18] Y. Makhlin, G. Schön, and A. Shnirman. *Quantum-state engineering with Josephson-junction devices.* Rev. Mod. Phys. **73**, 357 (2001).
URL http://dx.doi.org/10.1103/RevModPhys.73.357

[19] A. Fedorov, A. K. Feofanov, P. Macha, P. Forn-Díaz, C. J. P. M. Harmans, and J. E. Mooij. *Strong coupling of a quantum oscillator to a flux qubit at its symmetry point.* Phys. Rev. Lett. **105**, 060503 (2010).
URL http://dx.doi.org/10.1103/PhysRevLett.105.060503

[20] L. Childress, A. S. Sørensen, and M. D. Lukin. *Mesoscopic cavity quantum electrodynamics with quantum dots.* Phys. Rev. A **69**, 042302 (2004).
URL http://dx.doi.org/10.1103/PhysRevA.69.042302

[21] M. C. Teich and B. E. A. Saleh. *Squeezed state of light.* Quant. Opt. Euro. Opt. Soc. P. B **1**(2), 153 (1989).
URL http://stacks.iop.org/0954-8998/1/i=2/a=006

[22] C. M. Caves. *Quantum-mechanical noise in an interferometer.* Phys. Rev. D **23**, 1693 (1981).
URL http://dx.doi.org/10.1103/PhysRevD.23.1693

[23] S. S. Y. Chua, B. J. J. Slagmolen, D. A. Shaddock, and D. E. McClelland. *Quantum squeezed light in gravitational-wave detectors.* Classical and Quantum Gravity **31**(18), 183001 (2014).
URL http://stacks.iop.org/0264-9381/31/i=18/a=183001

[24] J. Miller, L. Barsotti, S. Vitale, P. Fritschel, M. Evans, and D. Sigg. *Prospects for doubling the range of Advanced LIGO.* Phys. Rev. D **91**, 062005 (2015).
URL http://dx.doi.org/10.1103/PhysRevD.91.062005

[25] E. S. Polzik, J. Carri, and H. J. Kimble. *Spectroscopy with squeezed light.* Phys. Rev. Lett. **68**, 3020 (1992).
URL http://dx.doi.org/10.1103/PhysRevLett.68.3020

[26] N. Didier, A. Kamal, W. D. Oliver, A. Blais, and A. A. Clerk. *Heisenberg-limited qubit read-out with two-mode squeezed light.* Phys. Rev. Lett. **115**, 093604 (2015).
URL http://dx.doi.org/10.1103/PhysRevLett.115.093604

[27] G. S. Agarwal and M. O. Scully. *Ramsey spectroscopy with nonclassical light sources.* Phys. Rev. A **53**, 467 (1996).
URL http://dx.doi.org/10.1103/PhysRevA.53.467

[28] H. Carmichael. *Statistical methods in quantum optics*, volume 1: Master equations and Fokker-Planck equations of *Texts and monographs in physics*. Springer, Berlin (1999). ISBN 3-540-54882-3.

[29] L. Genzel, editor. *Handbuch der Physik*, volume 25,2c: Licht und Materie 1c. Springer, Berlin (1970). ISBN 3-540-04856-1.

[30] W. Weidlich and F. Haake. *Coherence-properties of the statistical operator in a laser model.* Zeitschrift für Physik **185**(1), 30 (1965).
URL http://dx.doi.org/10.1007/BF01381300

[31] P. Mandel. *Fluctuations in laser theories.* Phys. Rev. A **21**, 2020 (1980).
URL http://dx.doi.org/10.1103/PhysRevA.21.2020

[32] S. André, V. Brosco, A. Shnirman, and G. Schön. *Phase diffusion and locking in single-qubit lasers.* Phys. Rev. A **79**, 053848 (2009).
URL http://dx.doi.org/10.1103/PhysRevA.79.053848

[33] S. André, V. Brosco, M. Marthaler, A. Shnirman, and G. Schön. *Few-qubit lasing in circuit QED.* Physica Scripta **2009**(T137), 014016 (2009).
URL http://stacks.iop.org/1402-4896/2009/i=T137/a=014016

[34] S. André. *Quantum electrodynamics with superconducting circuits: Effects of dissipation and fluctuations.* Ph.D. thesis, Fakultät für Physik, Karlsruher Institut für Technologie (2012).

[35] R. Loudon and P. L. Knight. *Squeezed Light.* J. Mod. Opt. **34**(6-7), 709 (1987).
URL http://dx.doi.org/10.1080/09500348714550721

[36] G. Reinhardt and W. Greiner. *Field quantization.* Springer (1996). ISBN 3-540-59179-6.

[37] M. Sargent, M. O. Scully, and W. E. Lamb. *Laser physics.* Addison-Wesley, Reading, Mass., 5th repr. edition (1987). ISBN 0-201-06903-2.

[38] K. Qu and G. S. Agarwal. *Ramsey spectroscopy with squeezed light.* Opt. Lett. **38**(14), 2563 (2013).
URL http://dx.doi.org/10.1364/OL.38.002563

[39] J. Braumüller and H. Rotzinger. *Private communications* (2016).

[40] H. J. Carmichael and D. F. Walls. *Modifications to the Scully-Lamb laser master equation.* Phys. Rev. A **9**, 2686 (1974).
URL http://dx.doi.org/10.1103/PhysRevA.9.2686

[41] M. O. Scully and W. E. Lamb. *Quantum theory of an optical maser. I. General theory.* Phys. Rev. **159**, 208 (1967).
URL http://dx.doi.org/10.1103/PhysRev.159.208

[42] M. Göppl, A. Fragner, M. Baur, R. Bianchetti, S. Filipp, J. M. Fink, P. J. Leek, G. Puebla, L. Steffen, and A. Wallraff. *Coplanar waveguide resonators for circuit quantum electrodynamics.* J. Appl. Phys. **104**(11) (2008).
URL http://dx.doi.org/10.1063/1.3010859

[43] D. Kohen, C. C. Marston, and D. J. Tannor. *Phase space approach to theories of quantum dissipation.* J. Chem. Phys. **107**(13), 5236 (1997).
URL http://dx.doi.org/10.1063/1.474887

[44] M. Marthaler, J. Leppäkangas, and J. H. Cole. *Lasing, trapping states, and multistability in a circuit quantum electrodynamical analog of a single-atom injection maser.* Phys. Rev. B **83**, 180505 (2011).
URL http://dx.doi.org/10.1103/PhysRevB.83.180505